Spring 2012

Investigation of the fracture phenomena during the milling process of inorganic particulates and brittle fracture of polymer composites using fractal theory

Zheng Qian
New Jersey Institute of Technology

ABSTRACT

INVESTIGATION OF THE FRACTURE PHENOMENA DURING THE MILLING PROCESS OF INORGANIC PARTICULATES AND BRITTLE FRACTURE OF POLYMER COMPOSITES USING FRACTAL THEORY

by

Zheng Qian

This dissertation investigates the applicability and usefulness of applying Fractal mathematics and to the fracture of brittle particulates in Fluid Energy Mill devices, and in particular quantifying the resulting power law particle size distributions, examining the Surface Fractal Dimension of milled particulates, and relating the Izod Impact Strength values of composites of polypropylene and Calcium carbonate particulates which are large un-milled, small milled, as well as small and produced by the simultaneous milling and coating with nano-silica to the Surface Fractal Dimension of the impact fracture surfaces.

First, the dissertation examines the behavior of un-coated and micron-sized wax pre-coated particulates in a specially designed Single-event Fluid Mill (SEFM), which is utilized to represent (for each pass) the Elementary Breakage Events in the Fluid Energy Milling process, and analyze the results in terms of the Fractal Theory.

The results establish that brittle milled particulates have self-similar shape to the original particulates, which points to the self-similarity property of fractals. Particle size distribution (PSD) of milled particulates obeys Power Law expression. This allows the

analysis of size reduction efficiency and specific kinetic energy of particulates during SEFM milling using fractal methods. For modeling the surface structure of particles by a fractal surface at various scales, Atomic Force Microscopy and the Gwyddion 2.25 software are used to measure the surface fractal dimension (D_s) of raw and ground particles. The results show that the surface fractal dimensions of $CaCO_3$ and KCl particles are independent of scale or grinding. This is a strong indication that the fracture process is self-similar. The surfaces of $CaCO_3$ and KCl particles are modeled very well by fractal surfaces. For the materials of $CaCO_3$ and KCl, a relationship between the macro-mechanical property and the micro-structure is built. The fractal dimension of the fracture surface increases with energy per unit surface area for fracture.

The dissertation also investigates the fractal behavior of the following Polypropylene (PP) based polymer composites performance during impact testing and establishes a quantitative relationship between the evolution of microstructure and fracture macro-mechanical properties by fractal theory. The results show that the Izod impact strength increases, as the fractal dimension of composite's impact-fractured surface increases.

PP is compounded with large un-milled , small milled, as well as small and produced by the simultaneous milling and coating with nano-silica Calcium carbonate at the 10 and 20 wt% levels. The Izod impact strengths of the composites are obtained and their values are related to their Surface Fractal Dimension. The results establish an excellent relationship, strongly indicating that increasing fracture surface roughness shows more inter-particle ligaments in the composites resulting tougher materials.

INVESTIGATION OF THE FRACTURE PHENOMENA DURING THE MILLING PROCESS OF INORGANIC PARTICULATES AND BRITTLE FRACTURE OF POLYMER COMPOSITES USING FRACTAL THEORY

by
Zheng Qian

A Dissertation
Submitted to the Faculty of
New Jersey Institute of Technology
in Partial Fulfillment of the Requirements for the Degree of
Doctor of Philosophy in Chemical Engineering

Otto H. York Department of
Chemical, Biological and Pharmaceutical Engineering

May 2012

.

APPROVAL PAGE

INVESTIGATION OF THE FRACTURE PHENOMENA DURING THE MILLING PROCESS OF INORGANIC PARTICULATES AND BRITTLE FRACTURE OF POLYMER COMPOSITES USING FRACTAL THEORY

Zheng Qian

Dr. Costas G. Gogos, Dissertation Advisor — Date
Distinguished Research Professor, Otto H. York Department of
Chemical, Biological and Pharmaceutical Engineering, NJIT

Dr. Marino Xanthos, Committee Member — Date
Professor, Otto H. York Department of
Chemical, Biological and Pharmaceutical Engineering, NJIT

Dr. John Tavantzis, Committee Member — Date
Professor Emeritus, Department of Mathematical Sciences, NJIT

Dr. Kwabena A. Narh, Committee Member — Date
Professor, Department of Mechanical and Industrial Engineering, NJIT

Dr. Ecevit A. Bilgili, Committee Member — Date
Assistant Professor, Otto H. York Department of
Chemical, Biological and Pharmaceutical Engineering, NJIT

BIOGRAPHICAL SKETCH

Author: Zheng Qian

Degree: Doctor of Philosophy

Date: May 2012

Undergraduate and Graduate Education:

- Doctor of Philosophy in Chemical Engineering,
  New Jersey Institute of Technology, Newark, NJ, 2012

- Bachelor of Science in Chemical Engineering,
  Zhejiang University, Hangzhou, P. R. China, 2001

Major: Chemical Engineering

Presentations and Publications:

Qian, Z., P. Wang and C.G. Gogos, *A novel method for preparation nanoparticle-coated additives used in polypropylene composites*. Polymer Engineering & Science (DOI 10.1002/pen.22187).

Qian, Z., P. Wang and C.G. Gogos, *Modifying $CaCO_3$ fillers with nanoparticles using a fluid energy mill*. Annual Technical Conference, ANTEC 2011, Conference Proceedings 1: p. 665-672.

Gogos, C.G., Z. Qian, H. Liu, Q. Zhang and C. Lu, *Dispersed nanoparticles give stronger plastics*. Society of Plastics Engineers Plastics Research Online (DOI 10.1002/spepro.004059).

Suwardie, H., P. Wang, Z. Qian and C.G. Gogos, *Rheological Characterization of Polypropylene Mixed with Specially Modified Calcium Carbonate*. Annual Technical Conference, ANTEC 2011, Conference Proceedings 3: p. 2296-2299.

He, Z., X. Wang, Y. Pu and Z. Qian, *Fundamental understanding of the role of potassium on the activity of Pt/CeO_2 for the hydrogen production from ethanol*. International Journal of Hydrogen Energy (DOI:10.1016/j.ijhydene.2011.12.054)

Zhang, Q., P. Wang, S. Teng, Z. Qian, L. Zhu and C.G. Gogos, *Simultaneous Milling and Coating of Inorganic Particulates With Polymeric Coating Materials Using a Fluid Energy Mill*. Polymer Engineering & Science, 2010. 50: p. 2366-2374.

Qian, Z., P. Wang and C.G. Gogos, *A Novel Method for Preparation of Nanoparticle-Coated Additives for Polymer Composites*. Poster Competition at Vinyltec 2010, Newark, NJ

To my beloved son, Ethan Qian; wife, Bo Xie;
my parents-in-law, Changyou Xie and Meijuan Lu;
my parents, Jianhua Qian and Xiaoping Zhu

ACKNOWLEDGMENT

I would like to show my deep gratitude to my advisor, Prof. Costas G. Gogos, for his insightful guidance, support and encouragement throughout my PhD study.

Special thanks are given to Prof. John Tavantzis, Prof. Marino Xanthos, Prof. Kwabena A. Narh and Prof. Ecevit A. Bilgili for their active participation in my dissertation committee and valuable suggestions. In particular I want to thank Prof. John Tavantzis for his active discussion and valuable suggestions about the mathematical part of my dissertation.

I am deeply grateful to Prof. Peng Wang, who was my committee and regretfully passed away in a car accident in February 6th, 2012, for his guidance, mentorship and encouragement.

I wish to acknowledge the financial support throughout my doctoral studies from the US Department of the Army, Contract DAAE30-03-D-1015, titled *Advanced Cluster Energetics (ACE^{TM})*. ACE is a collaborative R&D program between the ARDEC at Picatinny Arsenal, NJIT and Polymer Processing Institute (PPI). I would like to express my gratitude to Mr. Peter C. Bonnett of ARDEC for his constant support.

I would like to thank the staff of PPI for their generous help and cooperation. I feel very lucky that I had a chance to work in so warm and friendly environment with so many smart professionals. I extend my deep thanks to Dr. Ming-Wan Young and Dr. Linjie Zhu of PPI for their technical input and for making PPI equipment available for this dissertation. I want to thank Dr. Herman Suwardie, Dr. Kuan-Yin Lin and Mr. Viral Panchal for their assistance in the parts of polymer composites. I also want to address my

deep thanks to all my friends for their friendship and support: Dr. Shuli Teng, Dr. Qi Zhang, Dr. Huiju Liu, Dr. Nicolas Ioannidis, Dr. Min Yang, Graciela Terife, Dr. Jin Uk Ha, Zhong He, Bin Lin and Shasha Zhang.

Finally, I express deeply gratitude to my parents, Jianhua Qian and Xiaoping Zhu; my parents-in-law, Changyou Xie and Meijuan Lu; my wife, Bo Xie and my son, Ethan Qian. Their love, understanding, support and sacrifice made my pursuing PhD possible.

TABLE OF CONTENTS

Chapter **Page**

LIST OF TABLES

LIST OF FIGURES

LIST OF FIGURES
(Continued)

Figure **Page**

LIST OF FIGURES
(Continued)

Figure **Page**

LIST OF FIGURES
(Continued)

Figure **Page**

LIST OF SYMBOLS

D	Fractal dimension
M	The fraction of the particles smaller than the Size r
k	Size modulus which is the upper limit of particle size in the size distribution
n	Distribution modulus which is the index of uniformity given by the steepness of the PSD curve
D_b	The box-counting dimension
P	The cumulative distribution of particles with size greater than r
$p(r)$	The probability density function
$\emptyset$	A time-averaged quantity
$\emptyset'$	The fluctuating part of a time-averaged quantity
ρ	The density of the gas, kg/m^3
κ	Turbulent kinetic energy
ε	Turbulent dissipation rate
μ_t	The turbulent viscosity
p_{op}	The operating pressure
F_x	An additional acceleration (force/unit particle mass) term
$F_D(u-u_p)$	The drag force per unit particle mass
u	The fluid phase velocity
u_p	The particle velocity
μ	The molecular viscosity of the fluid

d_p	The particle diameter
ρ_p	The density of the particle, kg/m^3
Re	The relative Reynolds number
C_D	Drag coefficient
$\dot{m}_p$	Mass flow rate of the particles
Δt	Time step
F_{other}	Other interaction forces
ρ_s	Density of solid, kg/m^3
v	Poisson's ratio
Y	Young's molulus, GPa
σ_c	critical fracture stress, MPa
E_K	The total kinetic energy of particles in a specific particle size distribution
$v(r)$	The first impact velocity of particle with a function of particle, m/s
p	Grindability, m^2/kJ
D_s	Surface fractal dimension

CHAPTER 1

INTRODUCTION

1.1 Historical Perspectives and Objectives

The field of fractal geometry was advanced and definitively described by Mandelbrot [1] for the purpose of developing the ability to geometrically describe highly irregular structures occurring in nature. Usually such structures have irregularities or "roughness" of various sizes or at various scales and, as such, they are associated with each other by "scaling" relationships, which give them a geometric scaling hierarchy: each level in this scaling hierarchy, as the scale is reduced, is a smaller version than the just larger one.

Surfaces of fractured solids vary as to their roughness and irregularity, as well as the size of such irregular features. Thus, they are very good candidates to be described or characterized by fractal geometry. It should be noted here that the term "fractal" used by Mandelbrot shows the same Latin root with the word "fracture". Now, irregularities and roughness of fracture surfaces are the results of the solid's micro-structure or macro-structural characteristics (grains, crystallographic defects and dislocations, or inclusions of matter different from the solid matrix). They may also be affected, perhaps to a lesser degree, by macroscopic effects, such as the notch on an impact fracture test specimen, or in the case of particulates the shape of a large particulate colliding with another, or with a solid wall. Thus, it is not surprising that two years after 1982, when the seminal work of Mandelbrot "The Fractal Geometry of Nature" was published, he published a "letter" in Nature entitled "Fractal Character of Fracture Surfaces in Metals" [2]. In it, he and two IBM colleagues reported on experiments which "reveal the existence of broad and clearly distinct zone of intermediate scales (between macro and micro) in which the surface

structure is modeled very well by a fractal surface" [2]. They then obtained experimentally the basic quantity called fractal dimension, *D*, of the impact fracture surfaces of six identical 300 grade Maraging steel Charpy impact specimens, which were heat-treated at six different temperatures before impact testing, thus of different polycrystalline morphologies. *D* can range from 2, when the surface is smooth, increasing up to 3 with increasing surface roughness. The "fractal dimensional increment" of a surface is (*D-2*), which increases from 0 to 1 as the irregularities become increasingly predominant and the overall shape (form) of the surface becomes progressively less meaningful. *Figure 1.1 relates the fractal dimensional increment increase, which is the fracture surface roughness increase, to a linear decrease of the experimentally obtained impact energy. Relating complex and irregular fracture surface roughness characteristics*, dependent on both micro and macro material and morphological features, *through the simply obtained fractal dimensional increment D-2, to primary mechanical properties, such as the impact fracture energy, opened up new investigation horizons in fracture mechanics.* As shown in Figure 1.2, the number of yearly research publications, since 1986, dealing with both fractal and fracture increased in the early 1990's and have mirrored the growth of publications dealing with fractals solely. [3]

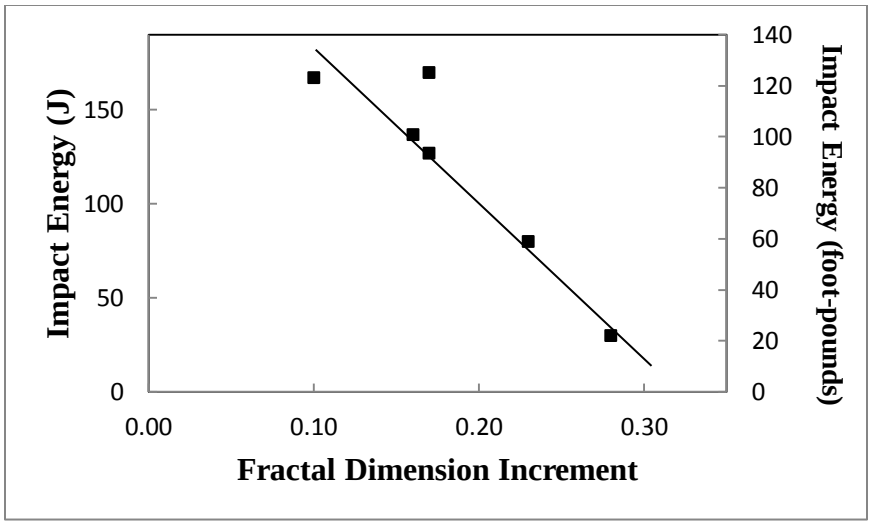

Figure 1.1 Impact energy versus fractal dimensional increment, 300-Grade Maraging steel, room temperature, Charpy impact. [2]

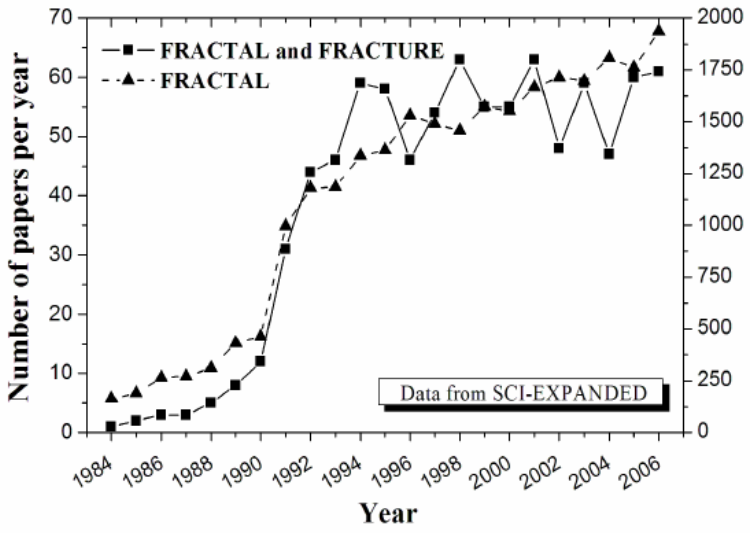

Figure 1.2 The number of papers published per year (1984 onwards), where the papers refer to those containing terms "Fractal" (on the right-hand axis) or "Fractal and Fracture" (on the left-hand axis) in their titles, abstracts, or keyword lists. [3]

The original thought for considering fractals in describing or predicting fracture mechanics processes and products in the Fluid Energy Mill (FEM) is that the solids of repeated fracture occurrences through FEM will be "self-similar" which includes two

aspects. First, the shape and morphology of un-milled and milled particles are similar independent of the scale, shown in Figure 1.3.

Second, the size distribution of particulates generated by grinding, milling and crushing operations can be described by a relatively uncomplicated Gaudin-Schuhmann distribution which is an approximation of Weibull distribution or Rosin-Rammler distribution. The Gaudin-Schuhmann distribution has the form:

$$M = \left(\frac{r}{k}\right)^n \tag{1.1}$$

where, M is the fraction of the particles smaller than the size r, k is the size modulus which is the upper limit of particle size in the size distribution and n is the distribution modulus which is the index of uniformity given by the steepness of the particle size distribution curve. Theoretically, lower values of n would suggest more fines or large particles, and fewer particles in the middle range [1]. The Gaudin-Schuhmann equation represents a scale invariance whose function of monomials is [4]:

$$f(x) = x^n \tag{1.2}$$

And scale invariance is a basic property possessed by a fractal distribution. [5]

With the above in mind, this study is commenced and attempts are made to apply fractal theory to build a linkage between the evolution of Single-Event Fluid Mill (SEFM) -obtained microstructures and macro-mechanical properties.

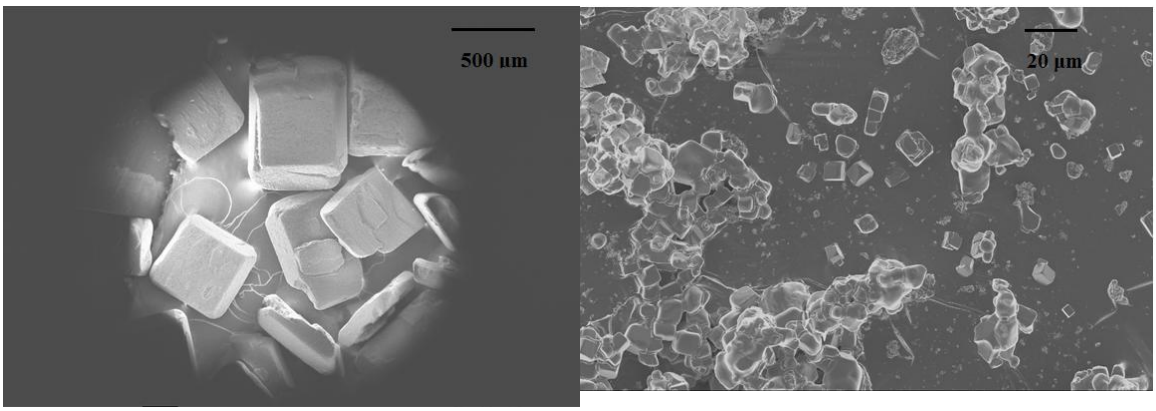

KCl (280 µm) FEM-milled KCl

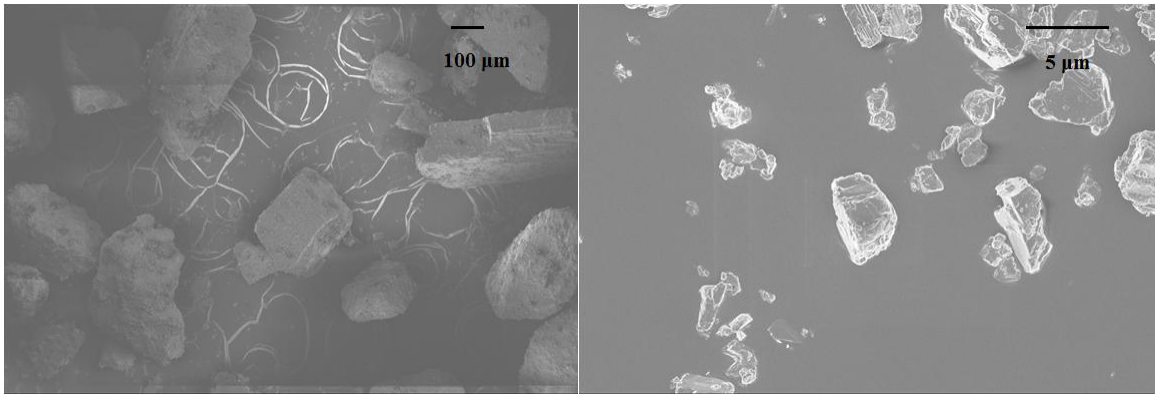

$CaCO_3$ (75~280 µm) FEM-milled $CaCO_3$

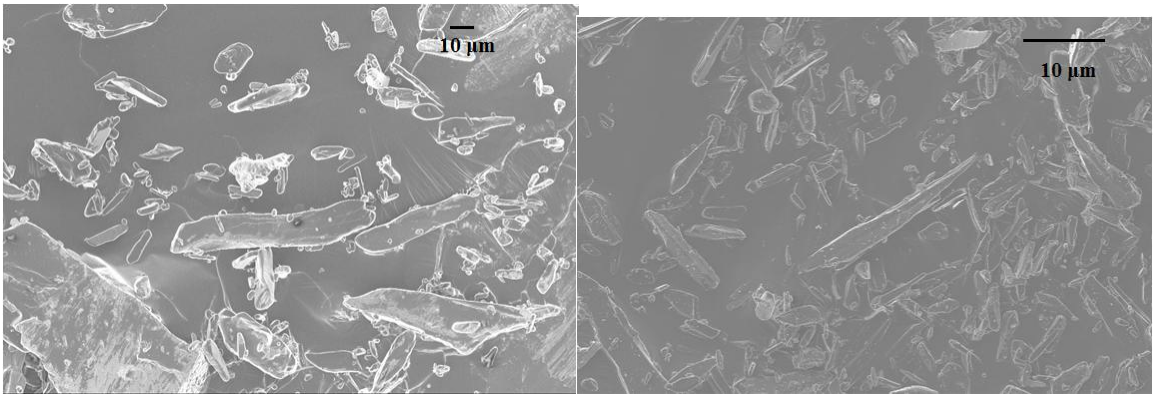

Acetaminophen (19 µm) FEM-milled Acetaminophen

Figure 1.3 SEM pictures of the studied solids.

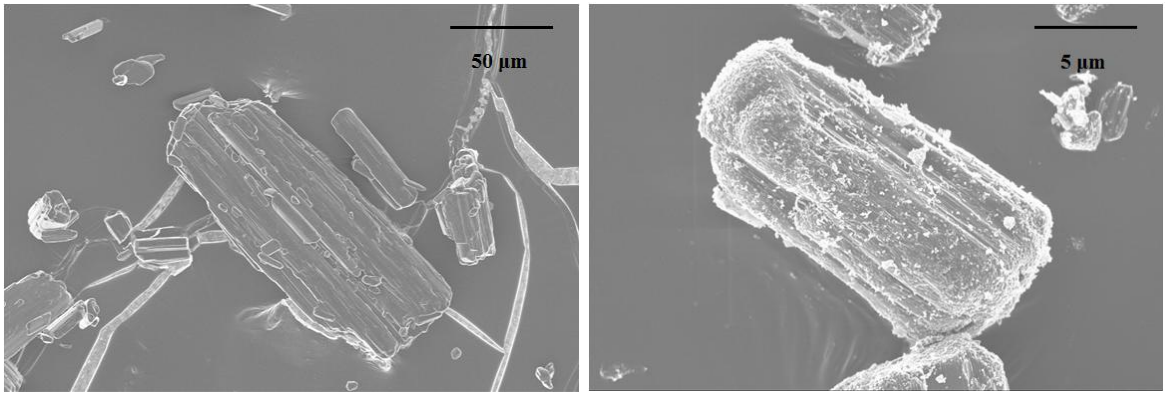

Guaifenesin FEM-milled Guaifenesin

Figure 1.3 SEM pictures of the studied solids (Continued).

1.2 Fractals

A fractal is a rough or fragmented geometric shape that can be split into parts, each of which is (at least approximately) a reduced-size copy of the whole [1]. Figures 1.4 and 1.5 represent two natural self-similar objects, images of fern and Romanesco broccoli, which are approximated by fractals to a degree. The image in Figure 1.4 is a self-similar, albeit mathematically generated. True ferns, however, will be extremely close to true self similarity. The broccoli's shape approximates a natural fractal; each bud is composed of a series of smaller buds, all arranged in yet another logarithmic spiral. This self-similar pattern continues at several smaller levels [6].

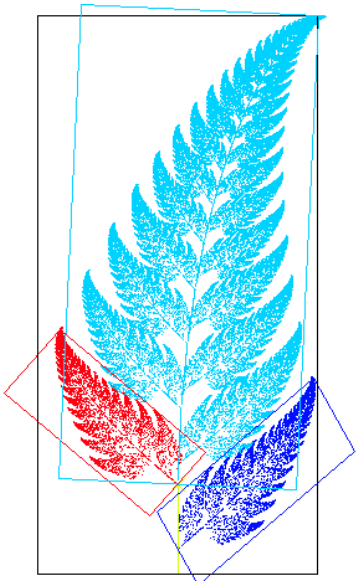

Figure 1.4 An image of a fern. [7]

Figure 1.5 Romanesco broccoli. [8]

A typical property of fractals is *self-similarity*. In mathematics, *a self-similar object* is *exactly* or *approximately similar to a part of itself* (i.e., the whole has the same shape as one or more of the parts). Many objects in the real world, such as coastlines, are *statistically self-similar*: parts of them show the same statistical properties such as configuration, shape, morphology, length etc. at many scales. [9] In summary, the types of self-similarity are listed below:

- **Exact self-similarity** – This is the strongest type of self-similarity; the fractal appears identical at different scales. Fractals defined by iterated function systems often display exact self-similarity. For example, the Sierpinski triangle exhibits exact self-similarity. [10]
- **Quasi-self-similarity** – This is a looser form of self-similarity; the fractal appears approximately (but not exactly) identical at different scales. Quasi-self-similar fractals contain small copies of the entire fractal in distorted and degenerate forms. Fractals defined by recurrence relations are usually quasi-self-similar but not exactly self-similar. The Mandelbrot set is quasi-self-similar, as the satellites are approximations of the entire set, but not exact copies. [10]
- **Statistical self-similarity** – This is the weakest type of self-similarity; the fractal has numerical or statistical measures which are preserved across scales. Most reasonable definitions of "fractal" trivially imply some form of statistical self-

> similarity. (Fractal dimension itself is a numerical measure which is preserved across scales.) Random fractals are examples of fractals which are statistically self-similar, but neither exactly nor quasi-self-similar. The coastline of Britain is another example; one cannot expect to find microscopic Britains (even distorted ones) by looking at a small section of the coast with a magnifying glass. [10]

Possessing self-similarity is not the sole criterion for an object to be termed a fractal. Examples of self-similar objects that are not fractals include straight lines, which do contain copies of themselves at increasingly small scales. These do not qualify as fractals, since they have the same Hausdorff dimension as topological dimension. [10]

Scale invariance is an exact form of self-similarity where at any magnification there is a smaller piece of the object that is similar to the whole [9]. In physics and mathematics, *scale invariance is a feature of objects or laws that do not change if length scales (or energy scales) are multiplied by a common scalar factor* [4].

Appendix A briefly describes the development of the mathematics behind fractals, which began three centuries ago.

1.3 Fractal Dimension

In fractal geometry, the fractal dimension, *D*, is a statistical quantity that gives an indication of how completely a fractal appears to fill space, as one zooms down to finer and finer scales. There are many specific definitions of fractal dimension. The most important theoretical fractal dimensions are the Rényi dimension, the Hausdorff dimension and the packing dimension. [11]

In mathematics, the Hausdorff dimension (also known as the Hausdorff–Besicovitch dimension) is an extended non-negative real number associated with any metric space. [12] The Hausdorff dimension generalizes the notion of the dimension of a real vector space. That is, the Hausdorff dimension of an n-dimensional vector space

equals n. This means, for example, the Hausdorff dimension of a point is zero, the Hausdorff dimension of a line is one, and the Hausdorff dimension of the plane is two. There are, however, many irregular sets that have a non-integer Hausdorff dimension. The concept was introduced in 1918 by the mathematician Felix Hausdorff. [12]

Intuitively, the dimension of a set (for example, a subset of Euclidean space) is the number of independent parameters needed to describe a point in the set. One mathematical concept which closely models this idea is that of topological dimension of a set. For example *a point in the plane* is described by two independent parameters (the Cartesian coordinates of the point), so in this sense, the plane is two-dimensional. As one would expect, the topological dimension is always a natural number. However, topological dimension behaves in quite unexpected ways on certain highly irregular sets such as fractals. [12]

To define the Hausdorff dimension for a metric space X as a non-negative real number (that is, a number in the half-closed infinite interval $[0, \infty)$), the number $N(r)$ of balls of radius r required to cover X completely is first considered. Clearly, as r gets smaller $N(r)$ gets larger. [12] Assuming there is an inverse proportion between $N(r)$ and r^D, $N(r) \sim 1/r^D$. As r is squeezed down towards zero, $D = -lim_{r \to o} \frac{log\, N}{log\, r}$, where D is the Hausdorff dimension of X. Figure 1.6 is the estimation of the Hausdorff dimension D of the coast of Great Britain.

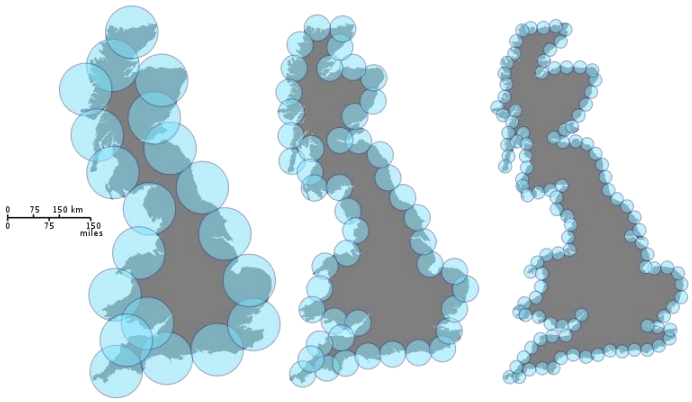

Figure 1.6 Estimating the Hausdorff dimension of the coast of Great Britain. [13]

There is a special geometry, which is composed by n number of non-overlapping smaller geometries with the same size. If the shapes of these smaller geometries are similar to those of the original geometry and the ratio of the smaller geometries to the original geometry is 1: m, the Hausdorff dimension of the special geometry is $D = \frac{log(n)}{log(m)}$.

For Euclidean geometries, such as the one shown in Figure 1.7, their Hausdorff dimensions $D = \frac{log(N)}{log(r)}$ equal their topological dimensions, which are integers. But for a fractal geometric object, such as the Koch curve shown in Figure 1.8, its Hausdorff dimension is a non-integer which is greater than its topological dimension. [14] The Koch curve is defined as follows: first, begin with a straight line of length 1, called the initiator. Then remove the middle third of the line, and replace it with two lines that each has the same length of 1/3 as the remaining lines on each side. This new form is called the generator, because it specifies a rule that is used to generate a new form. The rule dictates to take each line and replace it with four lines, each 1/3 the length of the original. Do this iteratively without end to generate a Koch curve. The length of a Koch curve increases

with each iteration and is infinite. [14] The Hausdorff dimension of a Koch curve is $D = \frac{log(4)}{log(3)} = 1.26 > 1.$

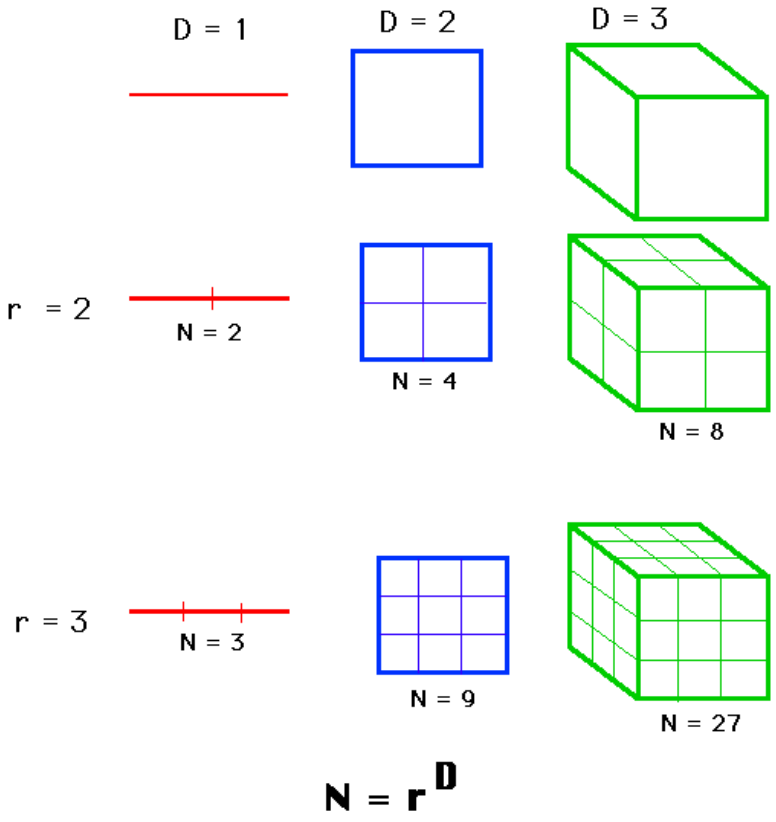

Figure 1.7 Defining dimension from a unit Euclidian object. [14]

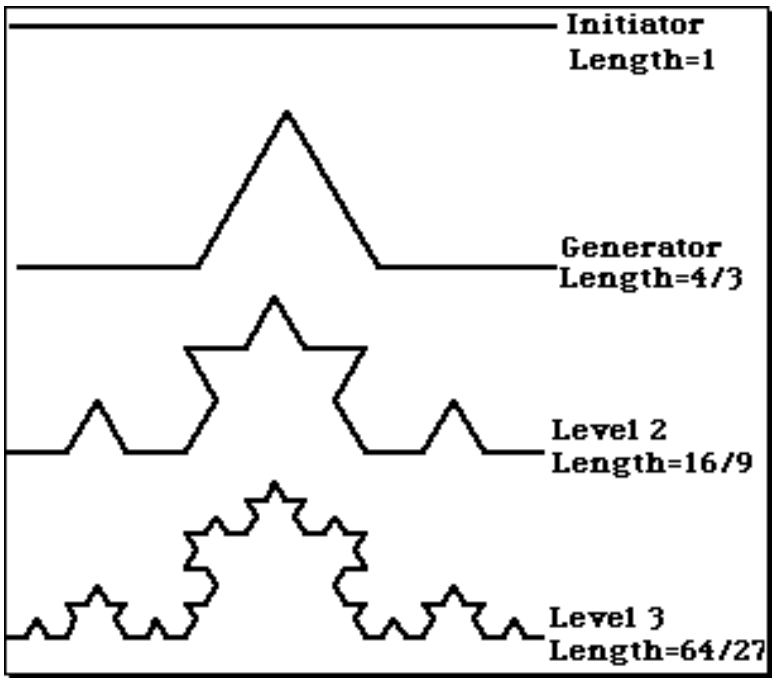

Figure 1.8 Koch curve, *D*=1.26. [14]

With the strict rule of self-similarity, the Hausdorff dimension can be easily obtained. But for a fractal structure which has a statistical self-similarity without a strict rule, such as the coastline in Figure 1.6, the Hausdorff dimension is not easy to derive directly. Therefore, for practical reasons, the "box-counting dimension" is widely used [15], partly due to its ease of implementation.

To calculate the box-counting dimension for a fractal, imagine this fractal lying on an evenly-spaced grid, and count how many boxes are required to cover the set. The box-counting dimension is calculated by seeing how this number changes as the grid becomes finer. [15] In a box counting algorithm the number of boxes covering the point set is a power law function of the box side. The fractal dimension is estimated to be the exponent of such power law. [11] Suppose that *N(r)* is the number of boxes of side length *r* required to cover the set. Then construct a log-log diagram of *log(N)* vs. *log (r)*. By fitting a straight line to the graph, the slope D_b was obtained. The value of D_b is the box-

counting dimension. Figure 1.9 gives an example of estimating the box-counting dimension of the coast of Great Britain. In Figure 1.9, N_a=194, r_a=1/24; N_b=283, r_b=1/32, so the box-counting dimension of the coastline of Great Britain is $D_b = \frac{(\log 283 - \log 194)}{(\log 32 - \log 24)} \approx 1.31$.

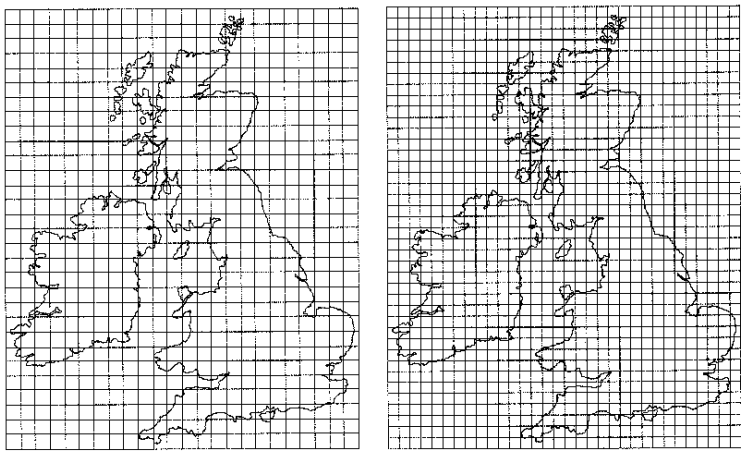

a b

Figure 1.9 Estimating the box-counting dimension of the coast of Great Britain, D_b=1.31. [16]

1.4 Fractal Dimension Describing Particle Size Distribution

Fragmentation, milling, and comminution [17] play an important role in a variety of phenomena and processes, both natural and man-made. Although fragmentation is of considerable economic importance and many experimental, numerical, and theoretical studies have been carried out on fragmentation, relatively little progress has been made in developing comprehensive theories that describe it. A primary reason of little progress in theories is that fragmentation involves the initiation and propagation of fractures. Fracture propagation is a highly physical nonlinear process requiring complex models for even the simplest configuration. Fragmentation involves the interaction between fracture

events over a wide range of scales and, thus, fractal distributions of number versus size are expected. [18] A variety of statistical relations has been used to correlate data on the size distribution of fragments, and a simple power-law relationship is often used.

For the distribution to be fractal, the number of objects *N* with a characteristic linear dimension greater than r, *N(>r)*, should satisfy the following "Power Law" relation

$$N(>r) = \frac{C}{r^D} \tag{1.3}$$

where, *C* is a constant of proportionality and *D* is the fractal dimension describing the particle size distribution. Then the total number of objects is given by

$$N(>r_{min}) = \frac{C}{r_{min}^D} \tag{1.4}$$

The cumulative distribution of particles with size greater than *r* is given by

$$P(>r) = \frac{N(>r)}{N(>r_{min})} = \left(\frac{r_{min}}{r}\right)^D \tag{1.5}$$

And, consequently, the complementary cumulative distribution of particles with size smaller than *r* is given by

$$P(<r) = 1 - \left(\frac{r_{min}}{r}\right)^D \tag{1.6}$$

where, experimentally it is typically found that *D* has values between 2 and 3 [18]. The related boundary conditions are:

$$P(<r_{min}) = 0 \tag{1.7}$$

$$P(\leq r_{max}) \cong 1 \tag{1.8}$$

if $r_{min} \ll r_{max}$. [19]

The probability density function *p(r)* multiplied by the interval amplitude *dr* represents the fraction of particles with size intermediate between *r* and *r*+*dr*. It is given by differentiating the cumulative distribution function, Equation (1.6), [18]:

$$p(r) = \frac{dP(<r)}{dr} = D\frac{r_{min}^{D}}{r^{D+1}} \tag{1.9}$$

The total volume of the particles is given by

$$V_{total} = \int_{r_{min}}^{r_{max}} \frac{1}{6}\pi r^3 N_p p(r) dr = \frac{1}{6}\pi N_p \frac{D}{3-D} r_{min}^{D}(r_{max}^{3-D} - r_{min}^{3-D}) \tag{1.10}$$

$$\cong \frac{1}{6}\pi N_p \frac{D}{3-D} r_{min}^{D} r_{max}^{3-D}$$

where N_p is number of particles.

Consequently, the volume of the particles with size smaller than *r* is given by

$$V(<r) = \int_{r_{min}}^{r} \frac{1}{6}\pi r^3 N_p p(r) dr \cong \frac{1}{6}\pi N_p \frac{D}{3-D} r_{min}^{D} r^{3-D} \tag{1.11}$$

Utilizing Equation (1.11) to compute the mass of the particles with size smaller than *r*:

$$M(<r) \cong \frac{1}{6}\pi N_p \rho_m \frac{D}{3-D} r_{min}^{D} r^{3-D} \tag{1.12}$$

where ρ_m is the material density, so that the ratio of this partial mass to the total mass is given by

$$\frac{M(<r)}{M(<r_{max})} \cong \left(\frac{r}{r_{max}}\right)^{3-D} \tag{1.13}$$

The logarithmic form of Equation (1.13) becomes

$$log\left(\frac{M(<r)}{M(<r_{max})}\right) \cong (3-D)\, log\frac{r}{r_{max}} \tag{1.14}$$

Equation (1.14) represents a straight line passing through the origin, where $r=r_{max,}$ in the bi-logarithmic plane, i.e., a fractal law, with slope equal to *3-D*. [19]

A simple model can illustrate how fragmentation can result in a fractal distribution. [18] This model is illustrated in Figure 1.10. A cube with a linear dimension *h* is referred to as a zero-order cell; there are N_0 of these cells. Each zero-order cell may be divided into eight equal-sized zero-order cubic elements with dimensions *h*/2. The volume V_1 of each of these elements is given by

$$V_1 = \frac{1}{8}V_0 \tag{1.15}$$

where, V_0 is the volume of the zero-order cells. The probability that a zero-order cell will undergo fragmentation to produce eight zero-order elements is taken to be *f*. The number of zero-order elements produced by fragmentation is

$$N_1 = 8fN_0 \tag{1.16}$$

After fragmentation the number of zero-order cells which have not been fragmented, N_{0a}, is given by

$$N_{0a} = (1-f)N_0 \tag{1.17}$$

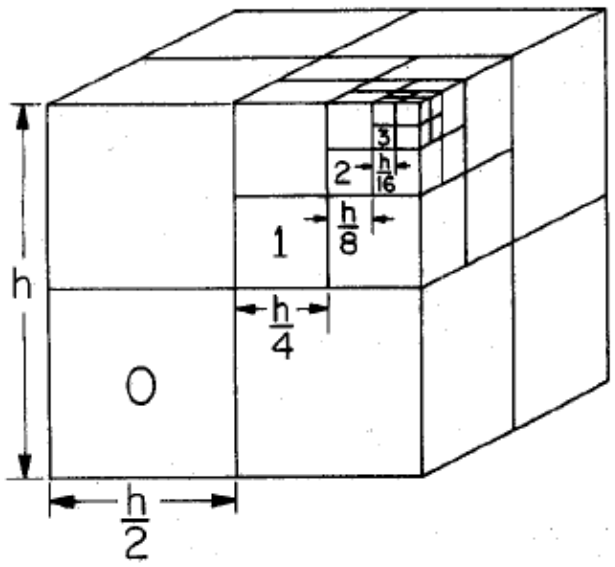

Figure 1.10 Idealized model for fractal fragmentation. [18]

Each of the zero-order elements is now taken to be a first-order cell. Each first-order cell may be fragmented again into eight equal-sized, first-order cubic elements with dimensions *h*/4. The fragmentation process is repeated for these smaller cubes. The problem is re-normalized and the cubes with dimension *h*/2 are treated in exactly the same way that the cubes with linear dimension *h* were treated above. Each of the fragmented cubic elements with linear dimension *h*/2 is taken to be a first-order cell; each of these cells is divided into eight first-order cubic elements with linear dimensions *h*/4 as illustrated in Figure 1.10. The volume of each first-order element is

$$V_2 = \frac{1}{8}V_1 = \frac{1}{8^2}V_0 \tag{1.18}$$

The probability that a first-order cell will fragment is again taken to be f to preserve scale invariance. The number of fragmented first-order elements is

$$N_2 = 8fN_1 = (8f)^2 N_0 \tag{1.19}$$

After fragmentation the number of first-order cells that have not been fragmented is given by

$$N_{1a} = 8f(1-f)N_0 \tag{1.20}$$

This process is repeated at successively higher orders. The volume of the nth-order cell V_n is given by

$$V_n = \frac{1}{8^n} V_0 \tag{1.21}$$

After fragmentation the number of nth-order cells is given by

$$N_{na} = (8f)^n (1-f) N_0 = (8f)^n N_{0a} \tag{1.22}$$

Taking the natural logarithm of both sides Equations (1.21) and (1.22) can be obtained as

$$ln\left(\frac{V_n}{V_0}\right) = -n\, ln\, 8 \tag{1.23}$$

$$ln\left(\frac{N_{na}}{N_{0a}}\right) = n\, ln(8f) \tag{1.24}$$

Dividing Equation (1.24) by Equation (1.23) gives:

$$\frac{ln\left(\frac{N_{na}}{N_{0a}}\right)}{ln\left(\frac{V_n}{V_0}\right)} = -\frac{ln(8f)}{ln\, 8} \tag{1.25}$$

Rearranging Equation (1.25) gives:

$$ln\left(\frac{N_{na}}{N_{0a}}\right) = ln\left(\frac{V_n}{V_0}\right)^{-ln(8f)/ln\, 8} \tag{1.25}$$

Equation (1.25) leads to:

$$\frac{N_{na}}{N_{0a}} = \left(\frac{V_n}{V_0}\right)^{-ln(8f)/ln\, 8} \tag{1.25}$$

Comparison with Equation (1.3) shows that this is a fractal distribution with

$$D = 3\frac{ln(8f)}{ln\, 8} \tag{1.26}$$

Although this model is idealized and non-unique, it illustrates the basic principles of how scale-invariant fragmentation leads to a fractal distribution. The division into 8 fragments is an arbitrary choice, however. Nevertheless, other choices such as the division into 2 or 16 fragments will give the same result. [18]

For this model, the allowed range of f is $1/8<f<1$ and the equivalent range of D is $0<D<3$ [18]. However, *experimentally the range of fractal dimension describing particle size distribution is $2<D<3$. For the first extreme case of $D=3$,* the probability that cells in every order will fragment is 1, which means that *every cell in each order will be divided into cells in the next higher order*. So all the cells in this distribution will have the same size and *this particle size distribution will be a mono-dispersed one, as shown as Figure 1.11*. On the other hand, for *the other extreme case of $D=2$,* the probability that cells in every order will fragment is 0.5, *which means that half the number of cells in each order will be divided into cells in the next higher order and the other half of the cells will stay un-fragmented*. So the number of cells in each order will be the same, which is half of the number of original cells and this distribution is *a uniform one, as shown as Figure 1.12*. Therefore, the fractal dimension describing a particle size distribution D indicates the uniformity of particle size. As D increases, the PSD becomes narrower.

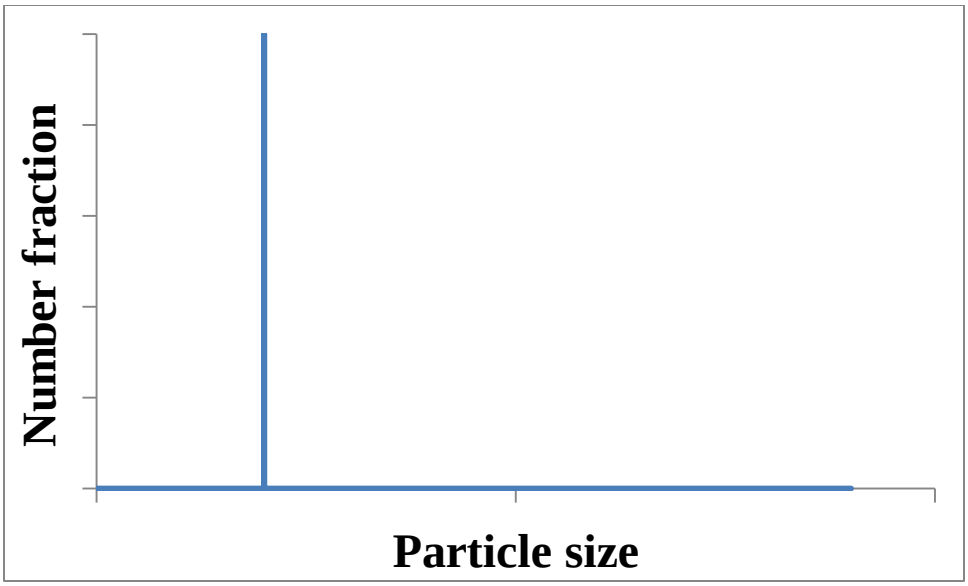

Figure 1.11 Mono-dispersed particle size distribution.

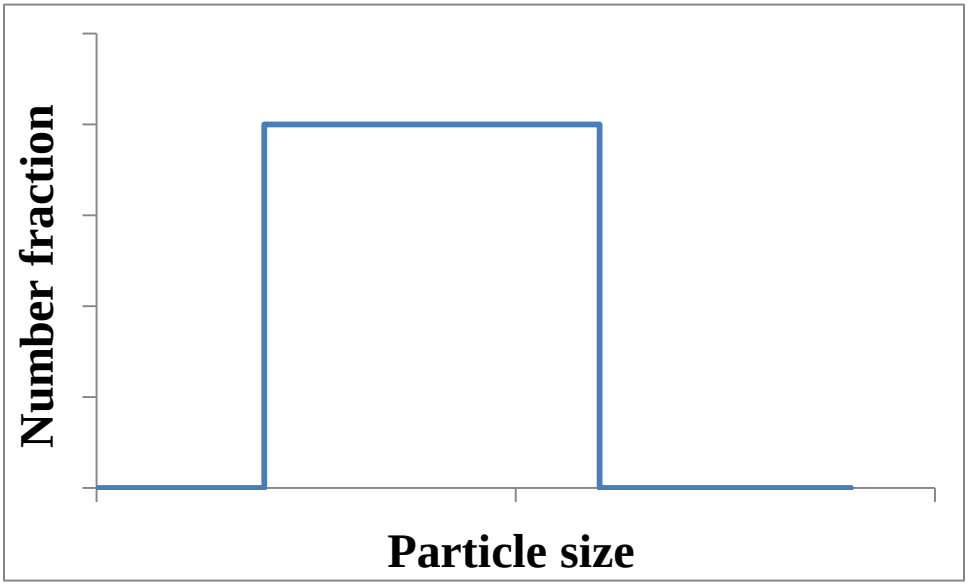

Figure 1.12 A uniform particle size distribution.

CHAPTER 2

FRACTAL PHENOMENA IN FRACTURE OF BRITTLE INORGANIC MATERIALS

2.1 Experimental

2.1.1 Materials Used in the Experimental Work

Cubic shaped Potassium Chloride (KCl) with density of 1.987 g/cc is purchased from REHEIS, Inc. (Berkeley Heights, NJ). The mean particle size of the raw KCl is 238.8 μm and the cumulative particle size distribution is shown in Figure 2.1.

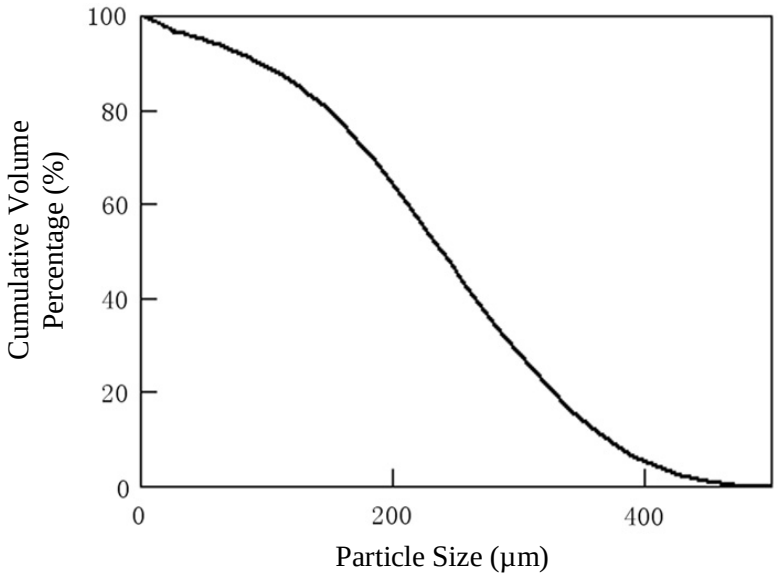

Figure 2.1 The cumulative size distribution of the raw KCl. [20]

Natural Carnauba wax particles (S-5021) with a mean particle size of 5-8 μm are supplied from Shamrock Technologies Inc. (Newark, NJ).

Calcium carbonate (CC) HUBERCARB® Q40-200 (cubic shape; particle size range of 75~380 μm) is obtained from J.M. Huber Corporation, Quincy, IL.

2.1.2 Equipment

2.1.2.1 Fluid Energy Mill (FEM). Previous milling research in our group focused on the performance and breakage mechanism of particulates in the Qualification Micronizer/ Fluid Energy Mill (FEM) manufactured by Sturtevant (Hanover, MA). FEMs of the vortex type are well known and widely employed in a variety of industries because of their efficiency and operational safety in the comminution of particulate solids, especially energetic ones, since there are no moving equipment parts.

FEMs are often employed in the industry to achieve ultra-fine grinding of minerals, pigments or metal oxides. Advantages of using an FEM include the ability to generate micron-sized particles with narrow size distributions, being essentially size classifying device, allowing only a narrow range of sizes to exit the milling chambers. Important factors are also the absence of contamination (again because there are no moving parts) and the ability of grinding heat-sensitive or energetic materials. FEMs are also particularly useful in the pharmaceutical industry, where micronization is used to increase drug activity and bio-availability by increasing particle specific surface, or by allowing pharmaceutically active substances to reach their site of action by reducing particle size. [21]

Figures 2.2 (a) and (b) show the entire system of the grinding equipment and the cross-sectional view of the Qualification FEM unit used, respectively. The FEM Qualification unit includes three air inlets: *one feed air inlet* and *two grinding air inlets*. After been controlled-fed into the feed funnel, the particles are “sucked” into the chamber through the Venturi effect created by the feed air stream. Under the influence of the grinding air jets which locally change their predominantly circular path, particles collide

with the peripheral wall and mainly with each other violently, causing comminution. The particles circulate inside the chamber until their sizes decrease to certain narrow value range determined by the feed and grinding air pressures, as well as the particle feed rate, which are the three process operation variables. When the drag forces imposing on a certain size particulate overcome the centrifugal force acting on it by virtue of the circular flow, the comminuted particles will exit through the center outlet.

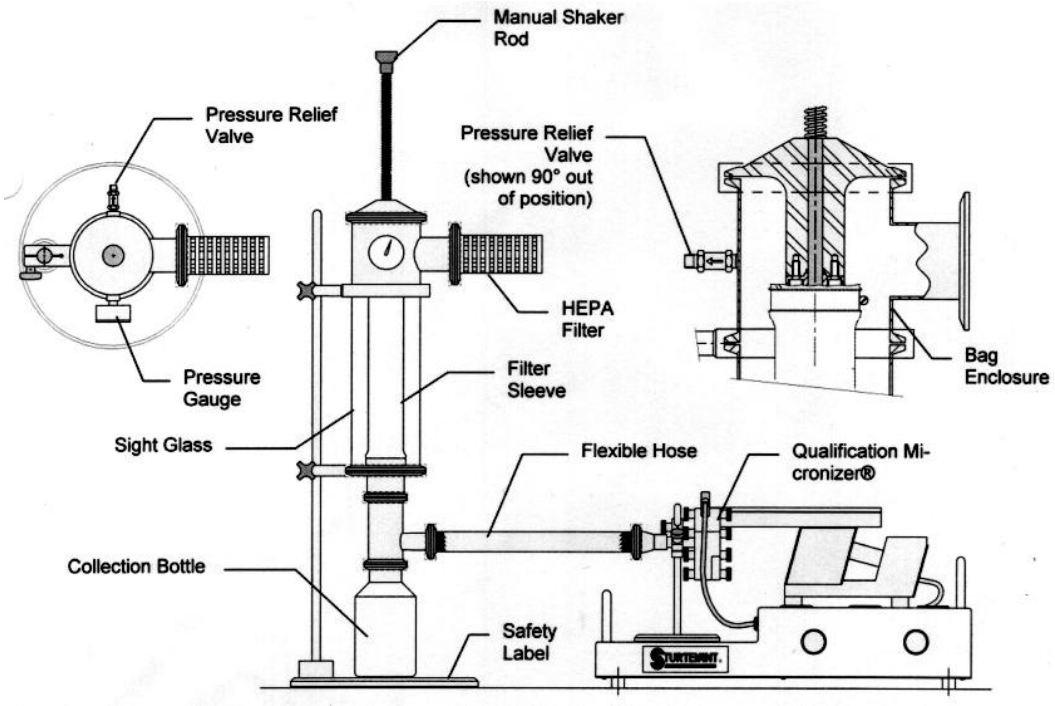

(a)

Figure 2.2 The whole FEM grinding system with the qualification milling chamber and accessories (a) and cross-section view of the qualification milling chamber (b). [22]

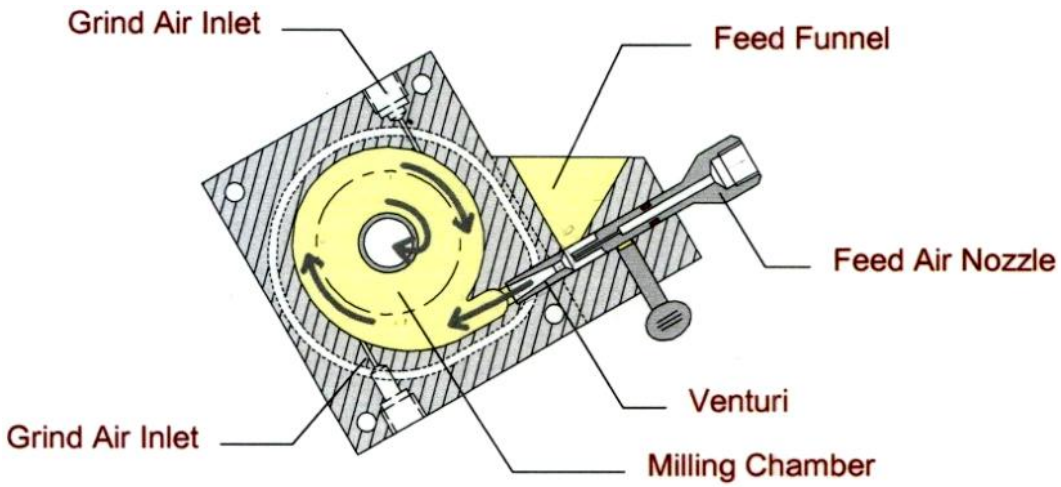

(b)

Figure 2.2 The whole FEM grinding system with the qualification milling chamber and accessories (a) and cross-section view of the qualification milling chamber (b). [22] (Continued).

2.1.2.2 Single-Event Fluid Mill. Because there are myriads of collisions occurring between particles and the FEM walls, the concept that the FEM milling can be viewed from a series of "Elementary Breakage Steps" is introduced. Then an apparatus of the "Single-event Fluid Mill" (SEFM) is constructed and used to experimentally characterize such Elementary Breakage Steps. The specially constructed Single-event Fluid Mill, shown schematically in Figure 2.3, creates similar breakage phenomena to those taking place in the FEM. The particles are fed from the feed funnel, accelerated by the air through the Venturi region and collide with the wall. Particle breakage is realized through both particle-wall and particle-particle collisions during the process. In this first cycle of milling in the SEFM, particles go through far fewer collision events than that in the FEM. The product of the first pass in the SEFM is fed into the device subsequent times, and each time the PSD is characterized. In the SEFM, a low air pressure is intentionally used

to ensure a small degree of breakage so that the particle breakage through each-pass of the SEFM may be utilized to represent the elementary breakage event in the FEM milling process. [20] The effect of the sum of 5-7 passes in the SEFM has the same effect as milling in the FEM.

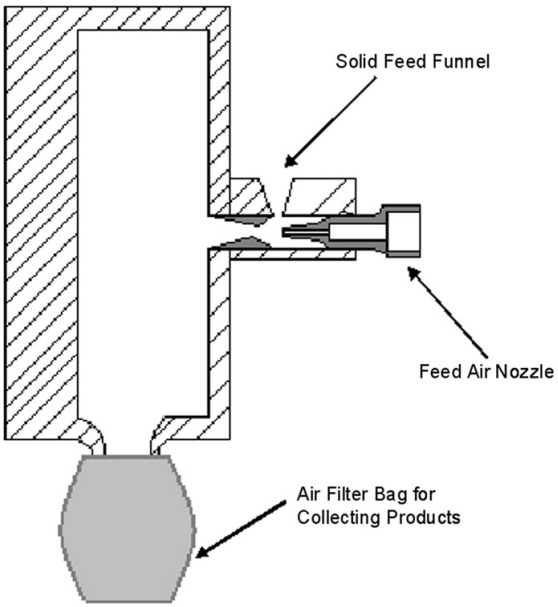

Figure 2.3 Schematic diagram of the single-event fluid mill. [20]

The Single-event Fluid Mill has a grinding chamber 76 mm high, 11 mm wide and 12 mm deep. The apparatus has the same air inlet, solid feed funnel and Venturi structure as the Qualification FEM. To maintain steady feeding of the particulate matter, a screw feeder (SCHENCK ACCURATE Co., White Water, WI) and a vibration feeder (Sturtevant Inc. Hanover, MA) are used in tandem to ensure the stability of the feed rate.

The original large KCl particles are dry-coated in a rotating tumbler coater with Carnauba wax particles. Both the un-coated and wax coated material are separately and carefully sieved with standard sieves to the single size interval of 250~420 μm. Un-coated KCl and wax coated KCl with such single size interval are used as the feed

materials and go through the Single-event Fluid Mill six consecutive passes. Raw uncoated $CaCO_3$ particles are fed through the SEFM eight consecutive passes.

2.1.3 Characterization

Field Emission Scanning Electron Microscopy (LEO 1530VP) is used to examine the morphology of particles.

LS230 laser diffraction Particle Size Analyzer (from Beckman Coulter, Fullerton, CA) is used to measure the particle size and size distribution of the ground product after each single pass through the grinding chamber. The operating conditions for all the materials used in the experimental work are kept identical for all consecutive passes. They are: Solid Feed Rate 5g/min and Air Inlet Pressure of either 68.9kPa (10psi), or 275.8kPa (40psi). [20] Note that the air feed pressure is also the grinding pressure in the SEFM.

Atomic force microscopy (AFM) (Digital Instrument Nanoscope III MultiMode Scanning Probe Microscope) and the free software Gwyddion 2.25 are used to analyze the surface fractal dimension (D_s) of the ground product after each single pass through the grinding chamber. AFM is applied in tapping mode. In the software Gwyddion 2.25, the cube counting method is applied for fractal analysis. The cube counting method is derived directly from the definition of box-counting fractal dimension. The algorithm is based on the following steps: a cubic lattice with lattice constant l is superimposed on the z-expanded surface. Initially l is set at $X/2$ (where X is length of edge of the surface), resulting in a lattice of $2\times2\times2 = 8$ cubes. Then $N(l)$ is the number of all cubes that contain at least one pixel of the image. The lattice constant l is then reduced stepwise by factor of

2 and the process repeated until *l* equals to the distance between two adjacent pixels. The slope of the plot *logN(l)* versus *log*1/*l* gives the surface fractal dimension D_s directly. [23]

2.1.4 Simulation

To obtain the Specific Kinetic Energy of particles fed in the SEFM, ANSYS FLUENT 12 (ANSYS, Inc. Canonsburg, PA), the widely used commercial CFD software, is employed as the tool to simulate the gas-solid two-phase flow. The Reynolds Averaged Navier-Stokes equations together with the κ - ε turbulent model are employed to describe the turbulent gas flow. [24] The interactions between the gas and solid phases only include momentum transfer because KCl and $CaCO_3$ are brittle materials where collision kinetic energy results in fracture and not plastic deformation, which, being dissipative, would generate heat. The Lagrangian Discrete Phase model is applied to simulate the gas-solid two-phase flow in the SEFM due to the low volume fraction of the dispersed second phase in the continuous gas phase. The Lagrangian Discrete Phase model in ANSYS FLUENT follows the Euler-Lagrange approach. The fluid phase is treated as a continuum by solving the Navier-Stokes equations, while the dispersed phase is solved by tracking a large number of particles, bubbles, or droplets through the calculated flow field.

2.1.4.1 Modeling the Turbulent Fluid Flow. The gas flow inside the grinding chamber is a three-dimensional time-dependent turbulent flow consisting of eddies superimposed on the mean flow. Instead of the instantaneous Navier–Stokes equations, the Reynolds-Averaged Navier–Stokes equations are used to describe the turbulent flow. The variables are divided into a time-averaged quantity and a fluctuating part as:

$$\emptyset = \overline{\emptyset} + \emptyset' \tag{2.1}$$

where $\overline{\emptyset}$ is the time-averaged quantity and $\emptyset'$ is the fluctuating part.[25]

Substituting the variables into the instantaneous continuity and momentum equations and taking a time average on those two equations yields Reynolds-averaged Navier–Stokes equations [26]:

$$\frac{\partial \rho}{\partial t} + \frac{\partial}{\partial x_i}(\rho \bar{u}_i) = 0 \tag{2.2}$$

$$\frac{\partial}{\partial t}(\rho \bar{u}_i) + \frac{\partial}{\partial x_j}\left(\rho \bar{u}_i \bar{u}_j\right) = -\frac{\partial \bar{p}}{\partial x_i} + \frac{\partial}{\partial x_j}\left[\mu\left(\frac{\partial \bar{u}_i}{\partial x_j} + \frac{\partial \bar{u}_j}{\partial x_i} - \frac{2}{3}\delta_{ij}\frac{\partial \bar{u}_l}{\partial x_l}\right)\right] + \frac{\partial}{\partial x_j}\left(-\rho\overline{u_i' u_j'}\right) \tag{2.3}$$

where ρ is the density of the gas, $\bar{u}_i$ and u_i' are the mean and fluctuating velocity components (i=1,2,3).

These equations have the same general form as the instantaneous equations, except that the Reynolds stresses term $-\rho\overline{u_i' u_j'}$ appear in the momentum equation. The above equations can only be used for incompressible turbulent flow. Although the approach of permitting a solution for the mean flow variables greatly reduces the computational effort, additional terms are added to the governing equations that need to be modeled to have sufficient number of equations for all the unknowns. [25]

The κ- ε model is one of the most simple and commonly used turbulence models, which is widely adopted for practical engineering applications. It is a semi-empirical model and contains two variables (turbulent kinetic energy κ and turbulent dissipation rate ε) and two extra transport equations [27]:

$$\frac{\partial}{\partial t}(\rho\kappa) + \frac{\partial}{\partial x_i}(\rho\kappa \bar{u}_i) = \frac{\partial}{\partial x_j}\left[\left(\mu + \frac{\mu_t}{\sigma_\kappa}\right)\frac{\partial \kappa}{\partial x_j}\right] + G_\kappa + G_b - \rho\varepsilon - Y_M \tag{2.4}$$

$$\frac{\partial}{\partial t}(\rho\varepsilon) + \frac{\partial}{\partial x_i}(\rho\varepsilon \bar{u}_i) = \frac{\partial}{\partial x_j}\left[\left(\mu + \frac{\mu_t}{\sigma_\varepsilon}\right)\frac{\partial \varepsilon}{\partial x_j}\right] + C_{1\varepsilon}\frac{\varepsilon}{\kappa}(G_\kappa + C_{3\varepsilon}G_b) - C_{2\varepsilon}\rho\frac{\varepsilon^2}{\kappa} \tag{2.5}$$

where G_κ is the generation of turbulence kinetic energy due to the mean velocity gradients, Y_M is the contribution of the fluctuating dilatation in compressible turbulence to the overall dissipation rate, G_b is the generation of turbulence kinetic energy due to buoyancy, $C_{1\varepsilon}$, $C_{2\varepsilon}$ and $C_{3\varepsilon}$ are constants, σ and σ_ε are the turbulent Prandtl numbers for κ and ε, respectively. μ_t is the turbulent viscosity and is computed as follows:

$$\mu_t = \rho C_\mu \frac{\kappa^2}{\varepsilon} \tag{2.6}$$

where C_μ is a constant.

The constants in the model are assigned with the following values, which were found to work fairly well for a wide range of turbulent flow:

$$C_{1\varepsilon} = 1.44 \;\; C_{2\varepsilon} = 1.92 \;\; C_\mu = 0.09 \;\; \sigma_\kappa = 1.0 \;\; \sigma_\varepsilon = 1.3$$

By employing the Boussinesq hypothesis, the additional Reynolds stresses term can be related to the mean velocity gradients, turbulent kinetic energy and turbulent viscosity:

$$-\rho\overline{u_i' u_j'} = \mu_t \left(\frac{\partial \bar{u}_i}{\partial x_j} + \frac{\partial \bar{u}_j}{\partial x_i}\right) - \frac{2}{3}\left(\rho\kappa + \mu_t \frac{\partial \bar{u}_i}{\partial x_i}\right)\delta_{ij} \tag{2.7}$$

Thus, the Reynolds stresses term can be solved by combining Eqs. (2.4) – (2.7). Once the Reynolds stresses term is known, the Reynolds averaged Navier–Stokes equations can be solved for the turbulent flow. [25]

2.1.4.2 Solver Selection and Simulation Strategy. ANSYS FLUENT offers two numerical solvers: pressure-based solver and density-based solver. Both of them adopt the concept of the control volume technique to solve the governing equations; however, the detailed approach to linearize and solve the algebraic equations is different. In this study, the pressure-based solver was employed to carry out the simulations. Within this

solver, there are two algorithms: a segregated algorithm and a coupled algorithm. In this case, the pressure-based segregated algorithm was selected.

Unlike laminar flow or inviscid flow, it is difficult to get a converged solution for the compressible turbulent flow directly. Thus, a solving strategy has to be utilized here to achieve a converged solution. Firstly, by treating the gas flow in the FEM as a laminar flow and regarding the density of the air as a constant (1.225kg/m^3), the converged solution is easily obtained. The convergence standards are set as 10^{-3} for continuity and velocity components. Then to treat turbulent flow, the κ-ε model is selected to simulate turbulence flow by applying the previous solution as the initial condition while keeping the air density as a constant. The convergence standards are not changed, but the turbulence parameters (κ, ε) are added. It is worth mentioning that no energy equation is included in the previous two steps. After obtaining the converged solution, the density of the air is assigned an initial value calculated by the following equation:

$$\rho = \frac{p_{op}}{\frac{R}{MW}T} \tag{2.7}$$

where p_{op} is the operating pressure, set at the atmospheric value. In FLUENT, the above rule of the air density is named "incompressible ideal gas law". [28] And again more iterations are carried out to get converged solution. The energy equation is implanted automatically by activating the "incompressible ideal gas law". The convergence standard for energy is set at 10^{-6}, whereas the standards of the rest variables are kept at 10^{-3}. Finally, the ideal gas law ias used to define the density, in which it not only depends on the operating pressure, but also on local gauge pressure. *This ultimate solution* is the *simulation result of the compressible turbulence flow in the FEM*. In the final step, the

convergence standards are set as follows: 10^{-4} for continuity, velocity components and turbulence parameters (κ , ε) and 10^{-6} for energy. [29]

2.1.4.3 Discrete Phase Particle. ANSYS FLUENT predicts the trajectory of a discrete phase particle by integrating the force balance on the particle, which is written in a Lagrangian reference frame. This force balance equates the particle inertia with the forces acting on the particle, and can be written (for the x direction in Cartesian coordinates) as

$$\frac{du_p}{dt} = F_D(u - u_p) + \frac{g_x(\rho_p - \rho)}{\rho_p} + F_x \tag{2.9}$$

where F_x is an additional acceleration (force/unit particle mass) term, $F_D(u - u_p)$ is the drag force per unit particle mass and

$$F_D = \frac{18\mu}{\rho_p d_p^2}\frac{C_D Re}{24} \tag{2.10}$$

Here u is the fluid phase velocity, u_p is the particle velocity, μ is the molecular viscosity of the fluid, ρ is the fluid density, ρ_p is the density of the particle, and d_p is the particle diameter. Re is the relative Reynolds number, which is defined as

$$Re \equiv \frac{\rho d_p |u_p - u|}{\mu} \tag{2.11}$$

For considering the mutual interactions between gas and solid phases, two-way coupling is used to simulate the momentum exchange between the two phases. The momentum transfer from the continuous phase to the discrete phase is computed in ANSYS FLUENT by examining the change in momentum of a particle as it passes through each control volume in the ANSYS FLUENT model. This momentum change is computed as

$$F = \sum \left(\frac{18\mu C_D Re}{\rho_p d_p^2 24} (u_p - u) + F_{other} \right) \dot{m}_p \, \Delta t \tag{2.12}$$

where μ = viscosity of the fluid

ρ_p = density of the particle

d_p = diameter of the particle

Re = relative Reynolds number

u_p = velocity of the particle

u = velocity of the fluid

C_D = drag coefficient

$\dot{m}_p$ = mass flow rate of the particles

Δt = time step

F_{other} = other interaction forces

This momentum change appears as a momentum source in the continuous phase momentum balance in any subsequent calculations of the continuous phase flow field and can be reported by ANSYS FLUENT.

2.1.4.4 Simulation Setup. In the two-phase simulation, only the main chamber and air feed funnel are investigated, as shown in Figure 2.4. For the CFD calculations, the main chamber and feed funnel are meshed into 22,144 tetrahedral elements. Particles are generated on the surface of the circular air inlet. KCl or $CaCO_3$ particles with size from 1 - 500 μm are introduced into the two-phase flow and the velocities of the particles' first impact at the wall opposite to the entrance of chamber are recorded.

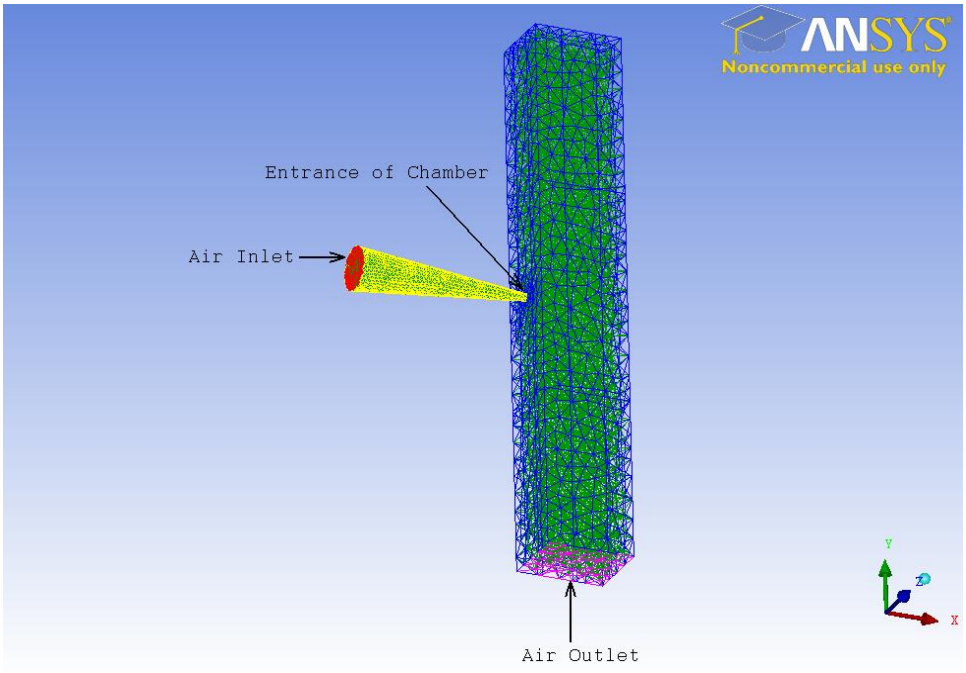

Figure 2.4 Geometry and mesh of the chamber of SEFM.

2.2 Results and Discussion

2.2.1 Macro-mechanical Properties

KCl in the size range of 250-420 μm and $CaCO_3$ with the mean particle size of 358 μm are subjected to repeated impacts at the same air inlet pressure. The whole fraction of particles (broken and unbroken) is re-impacted. Figure 2.5 shows the change of the mean size of the impacted particles as a function of the number of impacts for different air inlet pressure. In Figure 2.5, the mean velocities of $CaCO_3$ samples with the air inlet pressures of 68.9 kPa, 137.9 kPa and 275.8 kPa are around 10.8 m/s, 16.8 m/s and 24.5 m/s, respectively, while those of KCl samples with the air inlet pressure of 68.9 kPa and 275.8 kPa are around 12.5 m/s and 28.5 m/s, respectively. The mean velocities are the median of the cumulative distribution by a number obtained by simulation. [30]

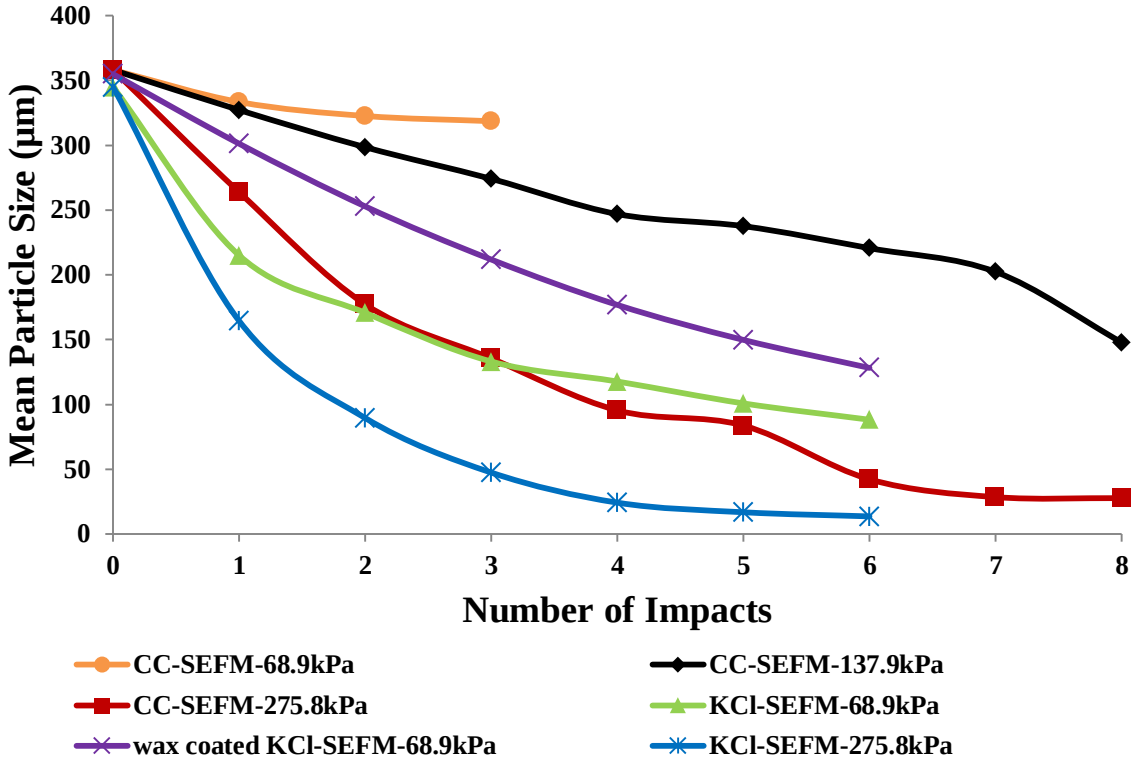

Figure 2.5 The evolution of mean size of impacted KCl and $CaCO_3$ particles with the number of impacts.

For the $CaCO_3$ with the air pressure of 68.9 kPa, no matter what the number of impacts is, no or negligible breakage occurs. This is because $CaCO_3$ particles under the air pressure of 68.9 kPa have a velocity of around 10.8 m/s which is the velocity attrition threshold representing the minimum velocity needed to cause the $CaCO_3$ particulates to fracture. For the cases under air pressure of 137.9 kPa and 275.8 kPa whose particle velocities are around 16.8 m/s and 24.5 m/s, respectively, there is size reduction with successive impact number because the velocities in these cases are above the velocity attrition threshold. For the $CaCO_3$ under air pressure of 275.8 kPa, mean particle size appears to plateau to a constant value after the sixth impact. Further impacts did not break the particles significantly suggesting asymptotical behavior and showing that some fraction of the particles is too strong to break at the velocity used, that is, had a high

threshold. [31] More impacts are needed to reach a threshold for the $CaCO_3$ under air pressure of 137.9 kPa. For the un-coated KCl under air pressure of 275.8 kPa, mean size of particles tends to be constant after the fifth impact. More impacts are needed to reach a threshold for the un-coated KCl and wax-coated KCl under air pressure of 68.9 kPa. At similar particle velocities, KCl can be milled to smaller size than $CaCO_3$. Similarly, KCl should have a smaller attrition threshold than $CaCO_3$ whose attrition threshold is 10.8 m/s for the mean particle size of 358.1 μm. For all the cases, as number of impact keeps going up, there is always an asymptotical behavior. This can be explained by the following reasons: 1) Particle size decreases with the increasing number of impacts, and the smaller particles break with more difficulty, thus lowering the breaking probability [32]; 2) As the particle size decreases the specific kinetic energy of the particle decreases; 3) Some fine particles will aggregate. Among the above reasons, the first one most probably dominates.

Relying on the Hertzian theory [33], Equation (2.13) was derived to evaluate the velocity fracture threshold V_{s0} to cause fracture during impact of different materials with walls [34].

$$V_{s0} = \left(\frac{4.99}{\pi\rho_s}\right)^{1/2} \left(\frac{1-\nu^2}{Y}\right)^{2/6} \left(\frac{\pi\sigma_c(28+20\nu)}{84}\right)^{5/6} \tag{2.13}$$

where ρ_s, density of solid; ν, Poisson's ratio; Y, Young's molulus (in compression); σ_c, critical fracture stress.

From literature, physical and mechanical property data for $CaCO_3$ particles are found and they are: ρ_s=2700 kg/m^3, ν=0.309 [35], Y=88 GPa [36] and σ_c=25 MPa [35]. The calculated V_{s0} using Equation (2.13), $V_{s0\text{-}calculated}$ is 9.5 m/s. $V_{s0\text{-}calculated}$ correlates very well with $V_{s0\text{-}experiment}$=10.8 m/s. The V_{s0} ≥10.8 m/s value is obtained by the simulation

used, as the simulated velocity when breakage of $CaCO_3$ is observed experimentally in the SEFM. V=10.8 m/s is simulated for $CaCO_3$ at 68.9 kPa, where only the beginning of breakage is observed. No such data is found for KCl.

Figure 2.6 shows the change of specific surface area of the impacted KCl and $CaCO_3$ as a function of the number of impacts. The specific surface area a_s (m^2/kg), derived from $a_s = \frac{6}{(\rho_s d(3.2))}$ where ρ_s is the specific gravity for solid (kg/m^3) and d(3.2) is the surface-volume diameter, or the Sauter mean diameter, calculated from the Malvern MasterSizer according to: $d(3.2) = \frac{\sum x_k dk^3}{\sum x_k dk^2}$ where dk is mean size of detected class (μm) and x_k is number fraction of detected size dk (number %). [37]

Energy imparted is a function of air inlet pressure and therefore with higher air inlet pressure larger surface area is obtained. Under the same air inlet pressure, fracturing of KCl particles generates larger surface area than $CaCO_3$ for the same number of impacts, because the threshold velocity V_{s0}, or threshold kinetic energy, KE=1/2ρV_{s0}, of KCl is smaller than that of $CaCO_3$. For the same number of impacts, fracturing of un-coated KCl particles generates larger surface area than the wax-coated KCl due to the partial dissipation of the kinetic energy by the “squeezing flow” of the wax coat during impact. This assumes that V_{s0} or the associated threshold kinetic energy is independent of the particle size, which may not be true.

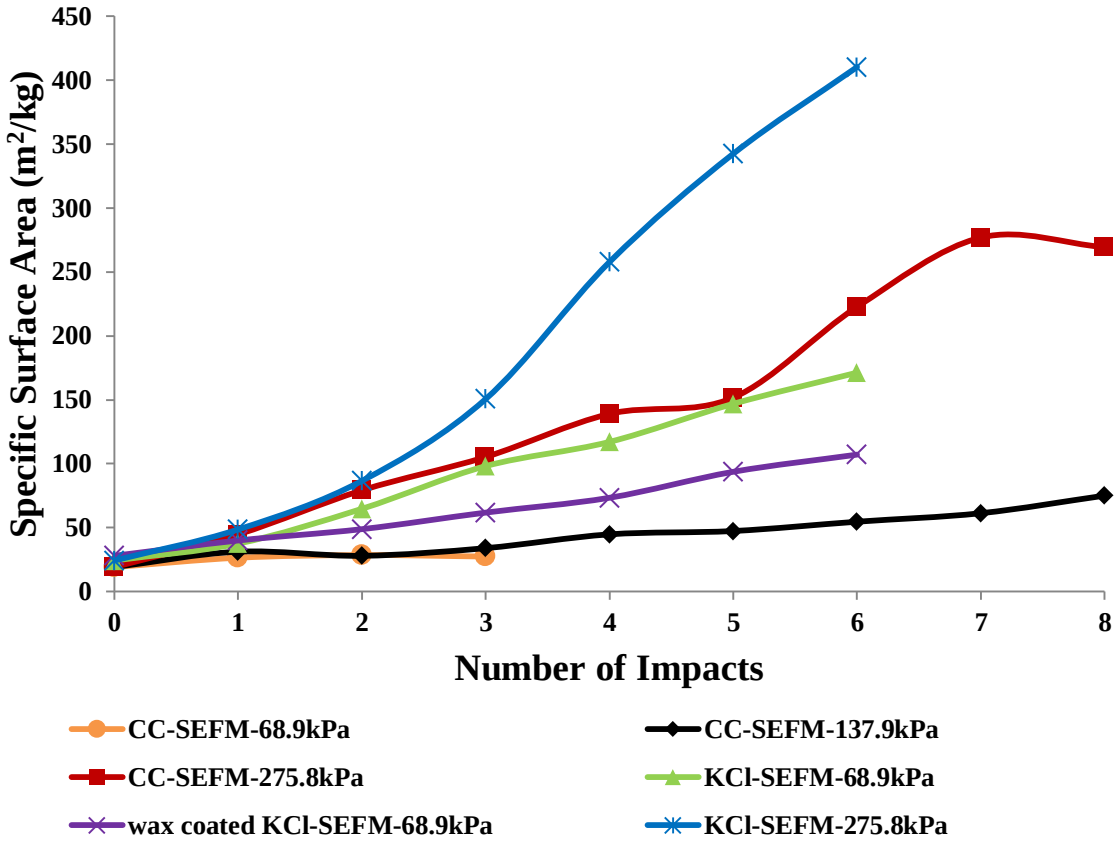

Figure 2.6 The evolution of specific surface area of the impacted KCl and $CaCO_3$ particles with the number of impacts.

Figure 2.7 illustrates the variation of the specific surface area vs. the specific kinetic energy for impacted KCl and $CaCO_3$. The specific kinetic energy (E_{SK}) is obtained from:

$$E_{SK} = \frac{E_K}{M} = \frac{\frac{1}{2}\int_{r_{min}}^{r_{max}} M(r)v^2(r)dr}{M} \tag{2.14}$$

where E_K is the total kinetic energy of particles in a specific particle size distribution, M is the total mass of particles in that specific particle size distribution and $v(r)$ is the first impact velocity of particle as a function of particle size.

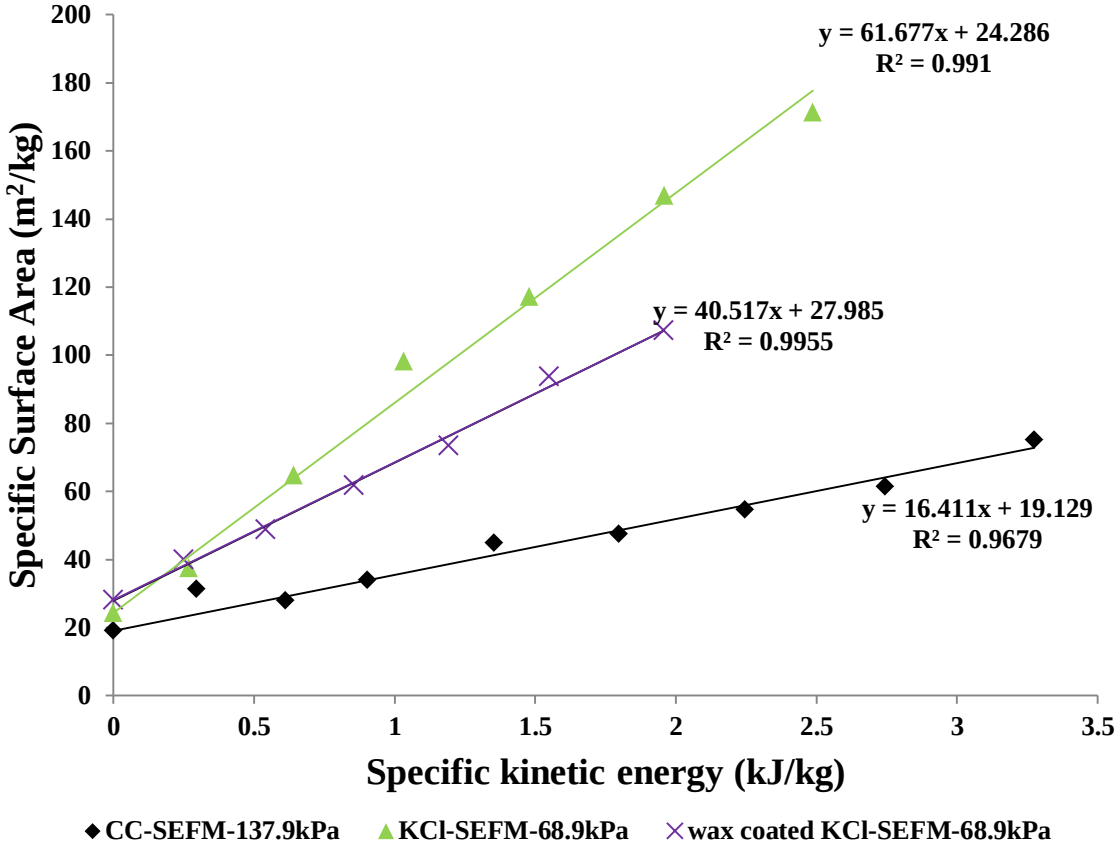

Figure 2.7 The evolution of specific surface area for $CaCO_3$, un-coated KCl and wax coated KCl with specific kinetic energy.

Only the velocities of the particles' first impact at the wall opposite to the entrance of chamber were recorded since most of the fracturing will occur during the first impact. The fractured particles will rarely result in a second fracture since they have very low kinetic energy after the initial fracturing. Because the velocity and kinetic energy of particles during the first impact is much higher compared to the following impacts, even particles that do not facture during the first impact will be unable to be fractured in subsequent impacts.

An example for the simulated particle velocities and trajectories can be seen in Figure 2.8. A single KCl particle with the size of 100 microns is introduced into SEFM. Figure 2.8 shows the path line of particle. The color scale indicates the particle velocity. The velocity of the first impact is 23 m/s, while the velocities of the following impacts are less than 10 m/s. The first impact velocity is quite capable of causing KCl fracture. The subsequent ones are "borderlines".

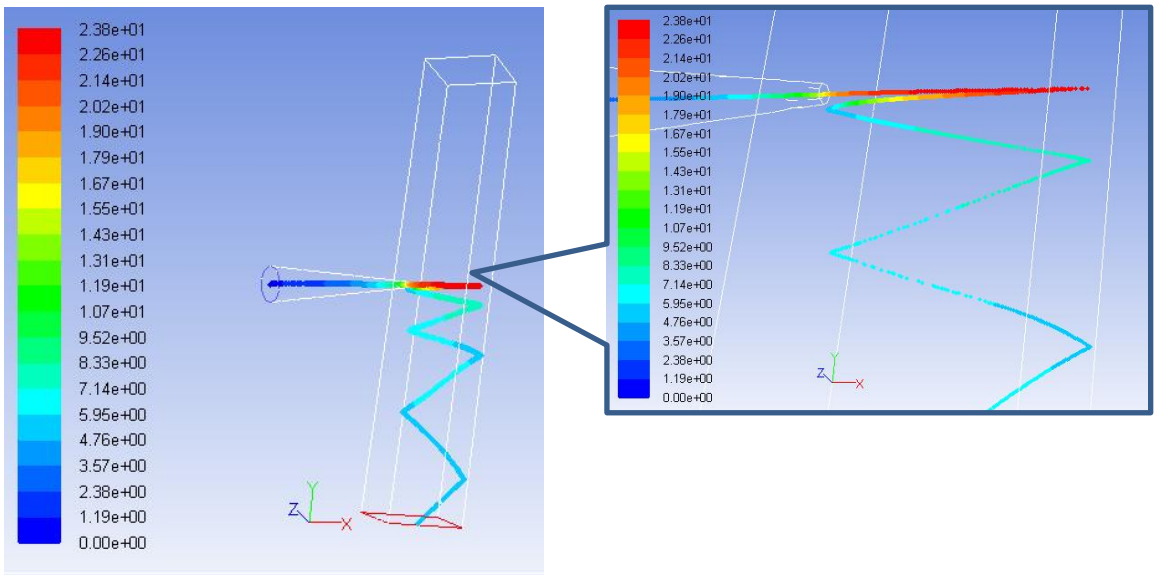

Figure 2.8 Path line image of KCl particle with the size of 100 µm introduced into SEFM under the feed pressure of 68.9 kPa.

Further evidence to prove that the velocities of particles during the first impact is much larger than those during the subsequent impacts, and that most of the fractures will occur during the first impact is shown in Figure 2.9. After feeding $CaCO_3$ to SEFM six consecutive times under feeding pressure of 275.8 kPa, the aluminum wall opposite to the entrance of SEFM chamber is eroded creating a hole with a diameter of 5 mm and a depth of 1 mm, while the other walls in the chamber are for all practical purposes unaffected.

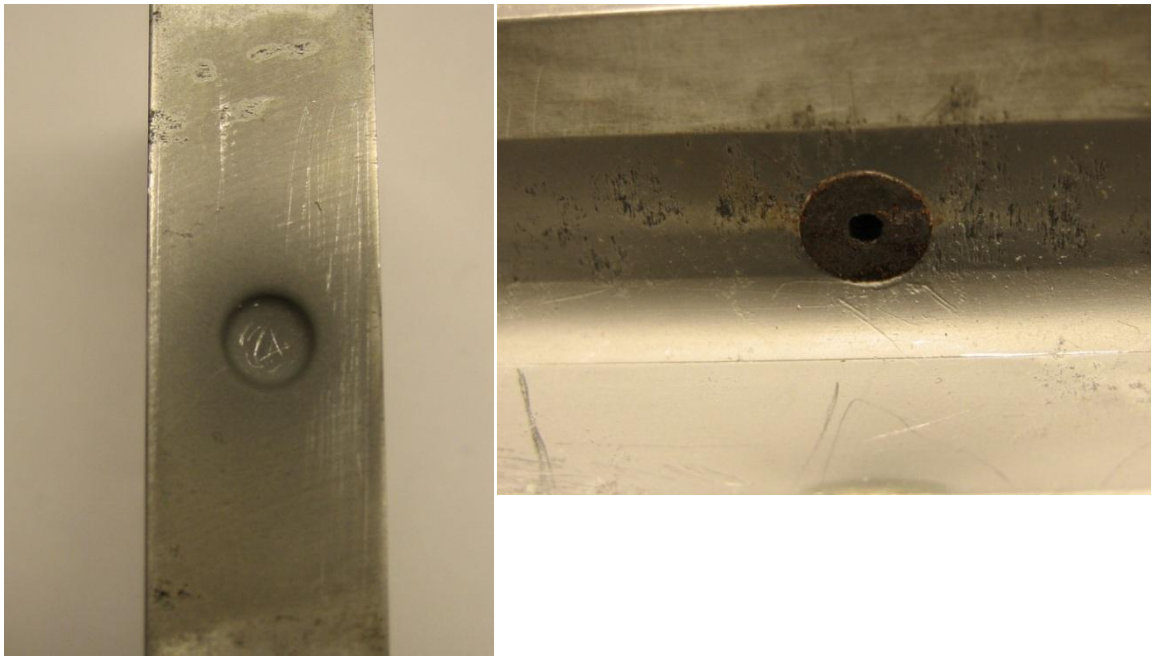

(a) (b)

Figure 2.9 Single-Event Fluid Mill chamber. (a) The eroded wall opposite to the entrance of chamber; (b) the entrance of chamber and the wall next to it.

Now return to the discussion of the specific kinetic energy of particles in a specific particle size distribution.

From Equation (1.10), gives:

$$M = \int_{r_{min}}^{r_{max}} N_p \rho_m \left(\frac{1}{6}\pi r^3\right) p(r) dr \tag{2.15}$$

Introducing Equation (2.15) into Equation (2.14) and rearranging obtains:

$$E_{SK} = \frac{(3-D)}{2} \frac{\int_{r_{min}}^{r_{max}} r^{2-D} v^2(r) dr}{r_{max}^{3-D} - r_{min}^{3-D}} \tag{2.16}$$

where D is the fractal dimension of particle size distribution before every impact.

$v^2(r)$, which is the particle velocity component of the kinetic energy, can be obtained from simulation, shown as follows. For KCl particles under air inlet pressure of 68.9 kPa in SEFM:

$$v(r) = -1.337r^2 + 21.444r - 17.449 \ (1\mu m \le r \le 10\mu m)$$

$$v(r) = 220.18r^{-0.49} \ (10\mu m \le r \le 500\mu m) \quad (2.17)$$

For KCl particles under air inlet pressure of 275.8 kPa in SEFM:

$$v(r) = 0.4664r^3 - 11.042r^2 + 81.243r - 46.393 \ (1\ \mu m \le r \le 10\ \mu m)$$

$$v(r) = 359.37r^{-0.434} \ (10\ \mu m \le r \le 500\ \mu m) \quad (2.18)$$

For $CaCO_3$ particles under air inlet pressure of 68.9 kPa in SEFM:

$$v(r) = 0.1237r^3 - 4.124r^2 + 36.193r - 29.225 \ (1\ \mu m \le r \le 7\ \mu m)$$

$$v(r) = 186.8r^{-0.485} \ (7\ \mu m \le r \le 500\ \mu m) \quad (2.19)$$

For $CaCO_3$ particles under air inlet pressure of 137.9 kPa in SEFM:

$$v(r) = 0.4594r^3 - 8.938r^2 + 58.5r - 27.168 \ (1\ \mu m \le r \le 7\ \mu m)$$

$$\mathrm{v(r) = 267.83r^{-0.472}\ (7\ \mu m \le r \le 500\ \mu m)} \quad (2.20)$$

For $CaCO_3$ particles under air inlet pressure of 275.8 kPa in SEFM:

$$v(r) = 4.217r^3 - 49.441r^2 + 194.61r - 123.08 \ (1\ \mu m \le r \le 5\ \mu m)$$

$$v(r) = 311.92r^{-0.433} \ (5\ \mu m \le r \le 500\ \mu m) \quad (2.21)$$

Finally, inserting Equation (2.17) to (2.21) into Equation (2.16), the equations for calculating the specific kinetic energy of KCl and $CaCO_3$ particles in SEFM under various air inlet pressures can be obtained.

For KCl particles under air inlet pressure of 68.9 kPa in SEFM:

$$E_{SK} = \frac{3-D}{2}\frac{1}{r_{max}^{3-D} - r_{min}^{3-D}}\left[\left(\frac{1.79}{7-D}r^{7-D} - \frac{57.35}{6-D}r^{6-D} + \frac{506.50}{5-D}r^{5-D}\right.\right. \quad (2.22)$$

$$\left.\left. - \frac{748.35}{4-D}r^{4-D} + \frac{304.47}{3-D}r^{3-D}\right)\Big|_1^{10} + \frac{48479.23}{2.02-D}r^{2.02-D}\Big|_{10}^{r_{max}}\right]$$

For KCl particles under air inlet pressure of 275.8 kPa in SEFM:

$$E_{SK} = \frac{3-D}{2}\frac{1}{r_{max}^{3-D} - r_{min}^{3-D}}\left[\left(\frac{0.22}{9-D}r^{9-D} - \frac{10.30}{8-D}r^{8-D} + \frac{197.71}{7-D}r^{7-D}\right.\right. \quad (2.23)$$
$$- \frac{1837.45}{6-D}r^{6-D} + \frac{7624.97}{5-D}r^{5-D} - \frac{7538.22}{4-D}r^{4-D}$$
$$\left.\left. + \frac{2152.31}{3-D}r^{3-D}\right)\right|_1^{10} + \left.\frac{129146.80}{2.132-D}r^{2.132-D}\right|_{10}^{r_{max}}\Bigg]$$

For $CaCO_3$ particles under air inlet pressure of 68.9 kPa in SEFM:

$$E_{SK} = \frac{3-D}{2}\frac{1}{r_{max}^{3-D} - r_{min}^{3-D}}\left[\left(\frac{0.015}{9-D}r^{9-D} - \frac{1}{8-D}r^{8-D} + \frac{13.08}{7-D}r^{7-D}\right.\right. \quad (2.24)$$
$$- \frac{305.73}{6-D}r^{6-D} + \frac{1550.96}{5-D}r^{5-D} - \frac{2115.48}{4-D}r^{4-D}$$
$$\left.\left. + \frac{854.1}{3-D}r^{3-D}\right)\right|_1^{7} + \left.\frac{34894.24}{2.03-D}r^{2.03-D}\right|_{7}^{r_{max}}\Bigg]$$

For $CaCO_3$ particles under air inlet pressure of 137.9 kPa in SEFM:

$$E_{SK} = \frac{3-D}{2}\frac{1}{r_{max}^{3-D} - r_{min}^{3-D}}\left[\left(\frac{0.21}{9-D}r^{9-D} - \frac{8.21}{8-D}r^{8-D} + \frac{133.64}{7-D}r^{7-D}\right.\right. \quad (2.25)$$
$$- \frac{11070.7}{6-D}r^{6-D} + \frac{3907.9}{5-D}r^{5-D} - \frac{3178.66}{4-D}r^{4-D}$$
$$\left.\left. + \frac{738.1}{3-D}r^{3-D}\right)\right|_1^{7} + \left.\frac{71732.91}{2.056-D}r^{2.056-D}\right|_{7}^{r_{max}}\Bigg]$$

For $CaCO_3$ particles under air inlet pressure of 275.8 kPa in SEFM:

$$E_{SK} = \frac{3-D}{2}\frac{1}{r_{max}^{3-D} - r_{min}^{3-D}}\left[\left(\frac{17.78}{9-D}r^{9-D} - \frac{416.98}{8-D}r^{8-D} + \frac{4085.71}{7-D}r^{7-D}\right.\right. \quad (2.26)$$
$$- \frac{20281.46}{6-D}r^{6-D} + \frac{50043.45}{5-D}r^{5-D} - \frac{47905.2}{4-D}r^{4-D}$$
$$\left.\left. + \frac{15148.69}{3-D}r^{3-D}\right)\right|_1^{5} + \left.\frac{97294.09}{2.134-D}r^{2.134-D}\right|_{5}^{r_{max}}\Bigg]$$

The slopes, *p*, of the straight lines in Figure 2.7 have the units of m^2/kJ and physically represent the grindability of the particulates. *p* can be interpreted as the amount of created surface per kilojoule, or more precisely as the increase of surface area for an input of energy. [31] For particle breakage in SEFM, it represents the efficiency of breakage including attrition in the nozzle and fracture during impact. The larger the value of *p*, the more surface will be created for a given energy input. The fact that the slope of the curve of un-coated KCl is greater than that of wax coated KCl indicates higher grindability parameter for un-coated KCl. The fact that the slope of the curve of $CaCO_3$ under the air inlet pressure of 137.9 kPa is smaller than that of wax coated KCl under the pressure of 68.9 kPa shows that breakage of $CaCO_3$ (i.e., its grindability) is much less than that of KCl.

Comparing Figure 2.5 and Figure 2.6, during the last impact of un-coated KCl particles under the air inlet pressure of 275.8 kPa, no significant size reduction can be observed but the specific surface area keeps increasing due to the generation of very fine particles that are generated most probably by the side-swipe particle-particle attrition in the nozzle. Therefore, the conclusion is that the attrition in the nozzle should affect the grindability parameter during the breakage of particles in SEFM.

Figure 2.10 shows the evolution of the relative fraction under 40 μm with the number of impacts. The curve of un-coated KCl under the air inlet pressure of 275.8 kPa reaches an asymptote at the fourth impact and remains constant with subsequent impacts, while the curves of two kinds of KCl under the air inlet pressure of 68.9 kPa do not reach an asymptote after 6 impacts. The reason is that the first impact will only break at several polycrystalline imperfections and all the imperfections corresponding to a specific energy

level will only be broken after several impacts. Lower air inlet pressure imparts lower energy, so the possibility of breaking imperfections under lower air inlet pressure is smaller. Therefore, the KCl particles under the air inlet pressure of 68.9 kPa require more impacts to break all the imperfections than those under the air inlet pressure of 275.8 kPa. Similarly, the curve of $CaCO_3$ under the air inlet pressure of 275.8 kPa reaches an asymptote at the sixth impact and remains fixed with subsequent impacts, while the curve of $CaCO_3$ under the air inlet pressure of 137.9 kPa does not reach an asymptote even after 8 impacts.

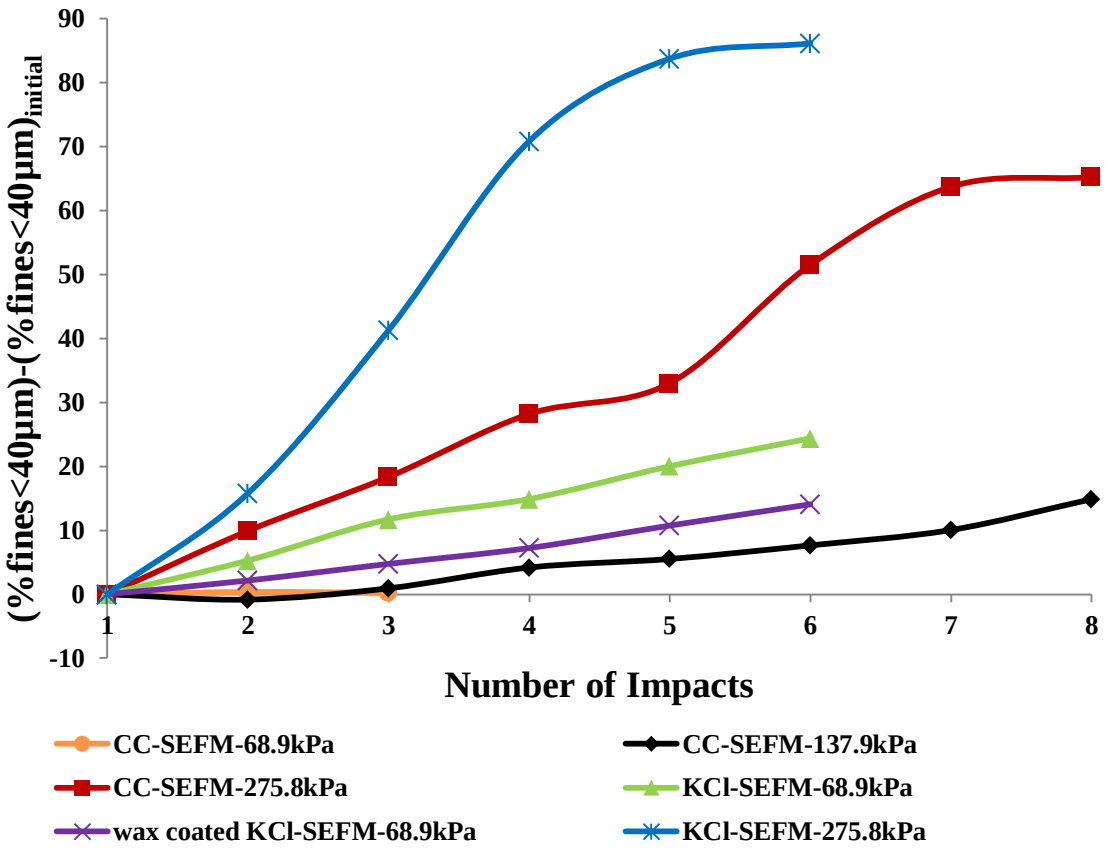

Figure 2.10 The evolution of the relative fraction under 40 μm with the number of impacts.

Figure 2.11 shows the evolution of fractal dimension describing the particle size distribution with the number of impacts. For the power law relationship of a fractal distribution shown in Equation (1.3), based on the assumption of constant material minimum or "quantum" of size r_{min}, the fractal dimension indicates the shape of the curve of particle size distribution and characterizes the mean particle size of the specific particle size distribution. The fractal dimension describing a particle size distribution can range from 2 to 3. Fractal dimension describing particle size distribution with the value of 3 means that all the particles have the same size and the curve of particle size distribution is at the limit of being "narrow", that is, it is *mono-dispersed* and can be represented by a vertical line. As the fractal dimension increases from the value of 2, the curve of particle

size distribution becomes narrower and shifts to smaller scale, as shown in Figures 2.12 to 2.15 for all the particulates systems studied. The mean particle size also decreases with the increasing fractal dimension. Therefore, the slopes of the curves shown in Figure 2.11 can also represent breakage efficiency which is primarily affected by fracture during impact. This is different from the grindability parameter in terms of specific surface area which is predominantly affected by attrition in the nozzle. Therefore, the behavior of curves in Figure 2.11 is similar but opposite to those in Figure 2.5. For the $CaCO_3$ with the air grinding pressure of 68.9 kPa, no matter what the number of impacts is, no fractal dimension describing PSD increase is observed. For the cases under air grinding pressures of 137.9 kPa and 275.8 kPa, the fractal dimension increases with the impact numbers. For the $CaCO_3$ under air pressure of 275.8 kPa, the fractal dimension describing PSD shows an asymptotic trend after the sixth impact. More impacts are needed to reach a constant value for the $CaCO_3$ under air pressure of 137.9 kPa. For the un-coated KCl under air pressure of 275.8 kPa, the fractal dimension describing PSD tends to become constant after the fifth impact. More impact cycles in the SEFM chamber are needed to reach a constant PSD for the un-coated KCl and wax coated KCl with the air grinding pressure of 68.9 kPa. In Figure 2.9, increasing the air inlet pressure increases the efficiency of size reduction due to more energy being imparted. As mentioned earlier, wax coating lowers the extent of size reduction due to the energy dissipated by the squeezing flow of the wax layer during impact. Under the same air grinding pressure, $CaCO_3$ particle size is reduced less than that of the KCl particles due to the higher $CaCO_3$ V_{s0}.

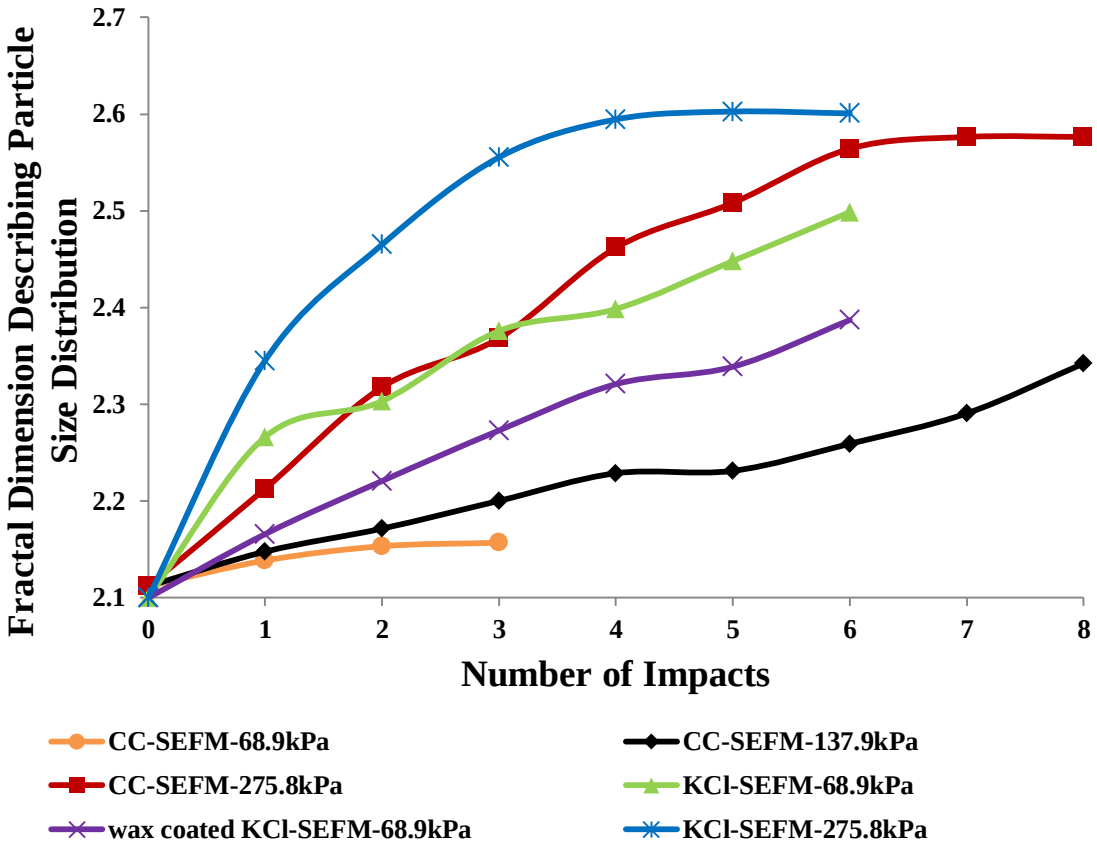

Figure 2.11 The evolution of the fractal dimension describing PSD with the number of impacts.

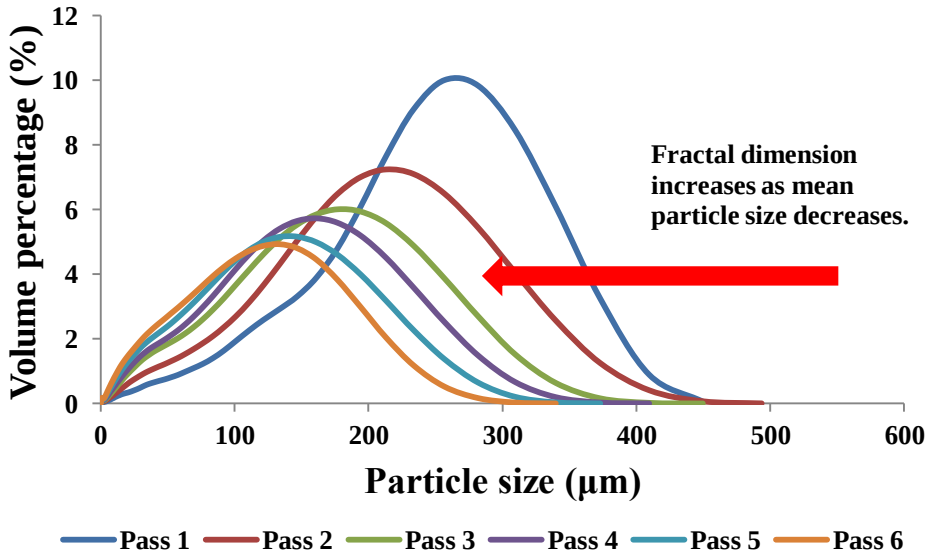

Figure 2.12 Particle size distribution of un-coated KCl through SEFM under the air inlet pressure of 68.9 kPa.

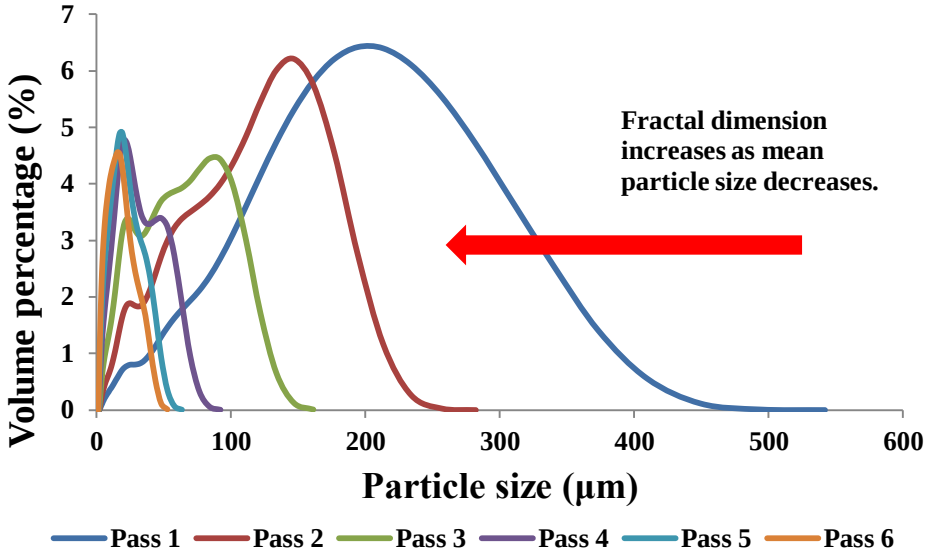

Figure 2.13 Particle size distribution of un-coated KCl through SEFM under the air inlet pressure of 275.8 kPa.

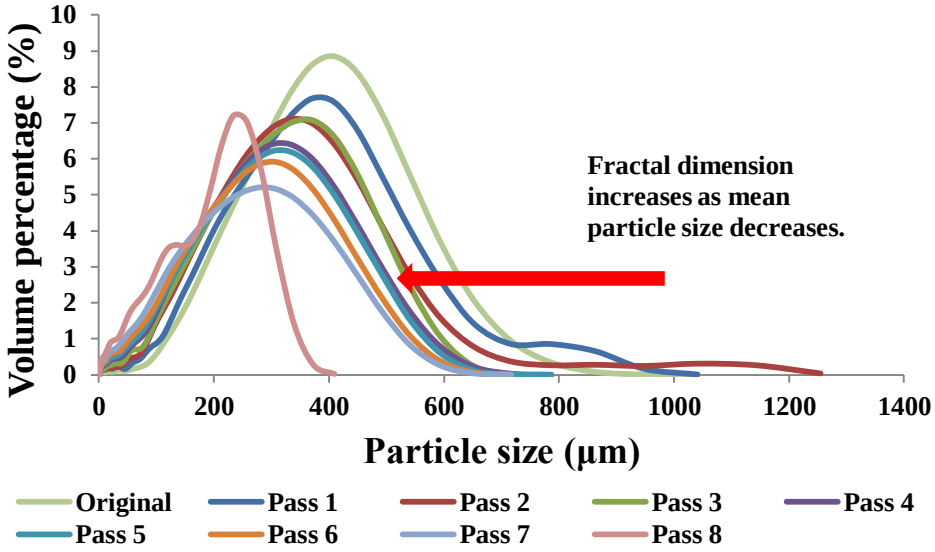

Figure 2.14 Particle size distribution of $CaCO_3$ through SEFM under the air inlet pressure of 137.9 kPa.

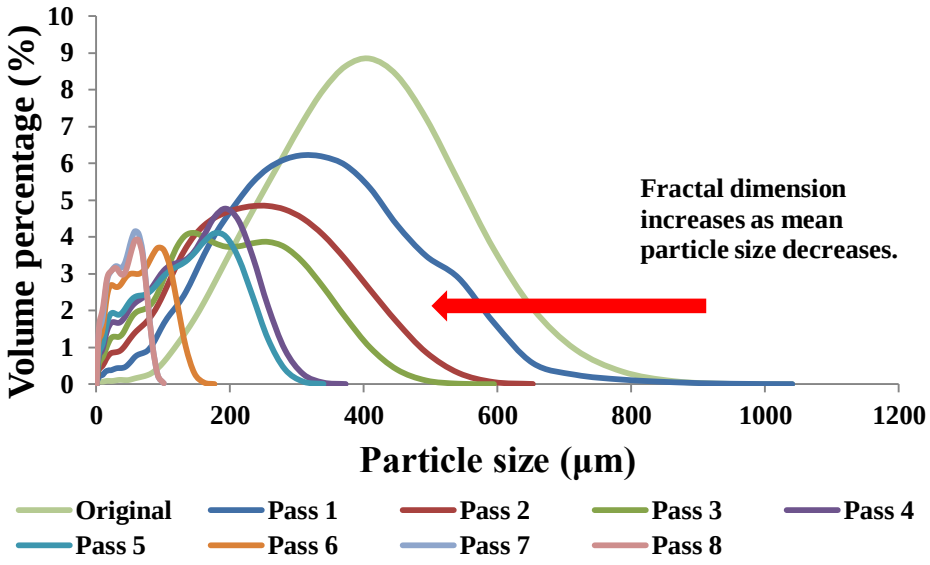

Figure 2.15 Particle size distribution of $CaCO_3$ through SEFM under the air inlet pressure of 275.8 kPa.

For future work, by using Population Balance Model, the specific breakage rate and the breakage distribution function will be introduced to analyze the difference of the evolution of particle size distribution through the consecutive passes of SEFM under different air inlet pressure. The breakage mechanisms, including attrition or fracture, of particles under different air inlet pressure are expected to be different, which can be characterized by the breakage distribution function. [32]

2.2.2 Microstructure

For relating the surface structure of particles to fractal surface description at various scales, Atomic Force Microscopy (AFM) and the free software Gwyddion 2.25 are used to measure the surface fractal dimension (D_s) of raw and ground particles.

Samples measured include: raw $CaCO_3$, ground $CaCO_3$ under the air grinding pressure of 275.8 kPa through SEFM through one to eight passes, raw KCl and ground

KCl under the air grinding pressure of 275.8 kPa through SEFM through one to six passes. For every sample, three individual particles are selected for measuring. For every particle, three locations of the particle surface are selected. For every location, three scanning areas of decreasing size (5×5 μm, 1×1 μm and 0.5×0.5 μm) are scanned. Table 2.1 shows the surface fractal dimensions for all the samples examined.

Fluid air milling produces in both brittle particulates of $CaCO_3$ and KCl, increasingly smaller particles whose surface roughness is almost identical to the one of the raw particles. This means that the myriads of fracture events produce surfaces of roughness that are characteristic of the polycrystalline material, but not the size.

The results show that the surface fractal dimensions of $CaCO_3$ and KCl particles are independent of scale or grinding. This is a good indication that the fracture process is self-similar. The surfaces of $CaCO_3$ and KCl particles are of the same roughness for milled and un-milled particles.

The surface fractal dimension of $CaCO_3$ particles is larger than that of KCl particles indicating greater roughness. The quantitative results do indeed agree with the qualitative appearances of roughness shown in Figure 1.3.

Table 2.1 Surface Fractal Dimension of Sample Particles

Materials	**Surface Fractal Dimension (D_s)**	**Average D_s**	**Mean Size** (μm)
Raw $CaCO_3$	2.35	2.39±0.02	358.1
$CaCO_3$ after 1 pass	2.40		263.8
$CaCO_3$ after 2 passes	2.43		177.2
$CaCO_3$ after 3 passes	2.38		135.5
$CaCO_3$ after 4 passes	2.41		95.4
$CaCO_3$ after 5 passes	2.38		83.7
$CaCO_3$ after 6 passes	2.40		42.2
$CaCO_3$ after 7 passes	2.39		28.5
$CaCO_3$ after 8 passes	2.39		27.7
Raw KCl	2.15	2.18±0.02	345
KCl after 1 pass	2.20		164.4
KCl after 2 passes	2.17		89.5
KCl after 3 passes	2.17		47.4
KCl after 4 passes	2.18		24.2
KCl after 5 passes	2.20		16.8
KCl after 6 passes	2.19		13.6

Switching the columns and rows of Figure 2.7, Figure 2.16 can be obtained. From Figure 2.16, the slope of the fitted straight line is 1/*p*, which represents the energy per unit surface area for fracture.

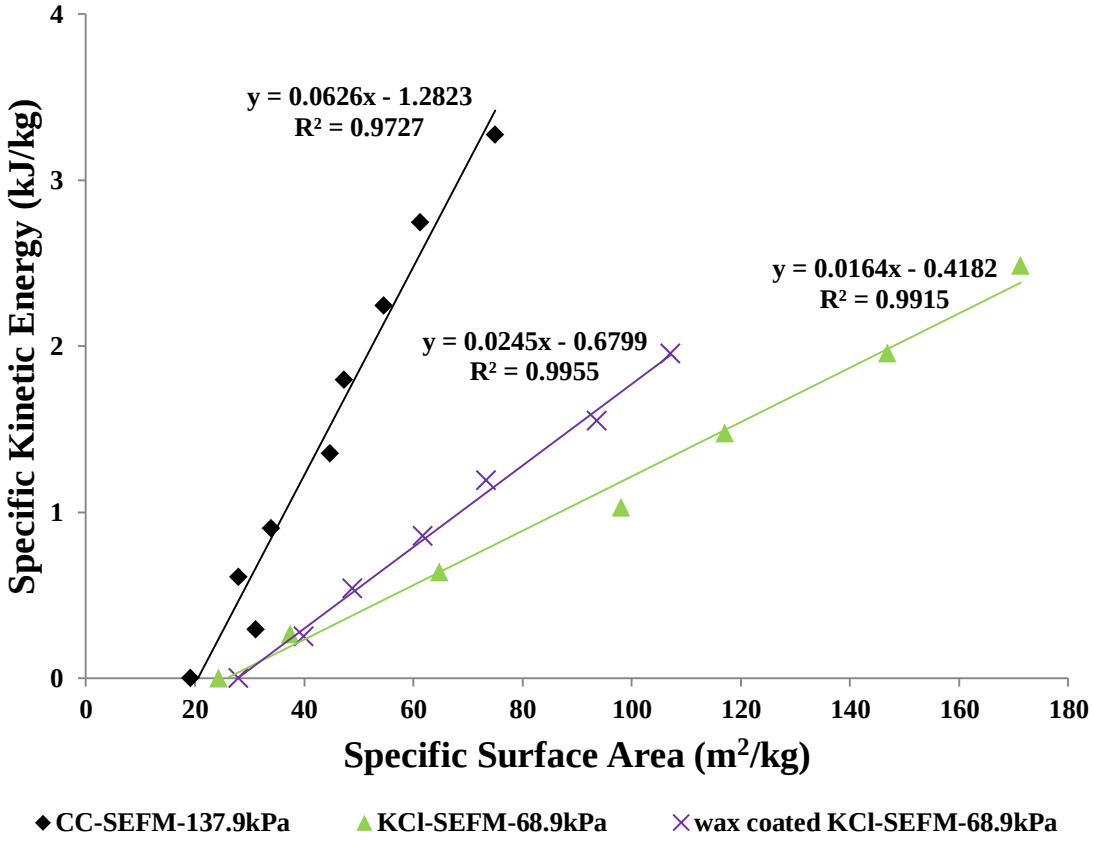

Figure 2.16 The evolution of specific kinetic energy for $CaCO_3$, un-coated KCl and wax coated KCl with specific surface area.

For the $CaCO_3$ and KCl particulates examined, 1/*p* increases with the fractal dimension of the fractured surface, which can be explained by the following. Considering the cases in which the fracture occurring obeys the Griffith energy balance concept. The total potential energy of the system *U*, for a static fracture, is:

$$U = (-W + U_E) + U_S \tag{2.27}$$

where W is the amount of work done by the external forces, U_E is the internal strain potential energy reserved in the elastic body and U_S is an expenditure energy in creating a

new fracture surface. Mechanical energy must decrease with fracturing, while the surface energy will increase because work must be spent to overcome the cohesion force. Therefore, there are two competing influences and at equilibrium there is a balance between them. The condition from equilibrium is:

$$J = -\frac{\partial U}{\partial A_T} = 0 \tag{2.28}$$

where J is identical to the potential energy release rate and A_T is the total area of the fracture surface. If U_E is almost constant during fracturing and the surface energy per unit area $\frac{\partial U}{\partial A_T}$ is constant for minerals or rocks, the Griffith energy balance concept indicates that W is proportional to the total area of the fracture surface produced. If the fracture surface is modeled very well by a fractal surface, the total area of the fracture surface A_T is proportional to r^D where D is the fractal dimension ($2<D<3$) and r the characteristic linear dimension of the fracture surface. Therefore, W can be expressed by:

$$W \propto A_T \propto r^D \tag{2.29}$$

From equation (2.29), the energy per unit surface area for fracture:

$$E \propto r^{D-2} \tag{2.30}$$

Equation (2.30) applied to $CaCO_3$ and KCl indicates that the energy per unit surface area for fracture increases with the fractal dimension of the fractured surface. [38]

2.3 Conclusions

The results in this chapter demonstrate that brittle milled particulates have self-similar shape to the original particulates, which points to the self-similarity property of fractals. PSD (particle size distribution) of milled particulates obeys Power Law expression. This

allows analyzing size reduction efficiency and specific kinetic energy of particulates during SEFM milling using fractal methods.

Under the same feed pressure and as impact numbers increase, KCl can be milled to smaller particle sizes than $CaCO_3$. Moreover, the fractal dimension describing the PSD of KCl increases faster than that of $CaCO_3$, and KCl particles, when milled under the same conditions, generate larger surface area than $CaCO_3$. The grindability of $CaCO_3$, predominantly affected by the attrition in nozzle, is much smaller than that of KCl.

The results from AFM show that the surfaces of $CaCO_3$ and KCl particles are modeled very well by fractal surfaces. The larger surface fractal dimension of $CaCO_3$ particles over KCl particles indicates that the roughness of $CaCO_3$ particles' surface is higher than that of KCl particles' surface. The quantitative results do indeed agree with the qualitative appearances of roughness shown in the SEM images of particles.

First conclusion for AFM: D_s is independent of the degree of milling. That is, the roughness is maintained and is invariant during milling. In milled samples, most surfaces are fresh, fracture generated. Therefore, they must have the same roughness as the original, and this roughness must be related to the polycrystalline morphology of the particulates. Also, SEFM caused fractures are due to cleavage of the bulk and preservation of the surface fracture.

For the materials of $CaCO_3$ and KCl, a relationship between the macro-mechanical property of energy per unit surface area for fracture and the micro-structural property of roughness of particle surface, characterized by the fractal dimension of fracture surface, is established. The energy per unit surface area for fracture increases

with the fractal dimension of the fracture surface, which is consistent with the Equation (2.30) derived from the Griffith energy balance concept.

CHAPTER 3

FRACTAL BEHAVIOR IN FRACTURE OF POLYMER COMPOSITES

3.1 Introduction

In the previous chapter, the fractal phenomena in the SEFM-caused fracture of brittle inorganic particles, such as $CaCO_3$ and KCl were discussed. This chapter investigates whether there are fractal phenomena during the fracturing of polymer composites.

A novel simultaneous milling and coating process has been developed in recent years for pre-coated large particulate materials in our laboratories [39-44]. The process utilizes a fluid energy mill to break and coat pre-coated feed particulate materials. Milling and coating are two processes commonly used to adjust many particulate properties, such as flowability, mechanical properties, dissolution rate, and reactivity. Simultaneous milling and coating is not only more efficient compared to separate processes, but also, and more importantly, is the only process which allows coating of highly cohesive or *very fine particles*, without using solution methods (e.g., slurry coating). Inside the FEM, pre-coated large feed particles are milled and simultaneously coated during particle-particle collisions, before they even have a chance to agglomerate with other particles since both milling and coating occur when particles *are maintained in a high kinetic energy fluidized state*. Previous experimental results demonstrate that the process can be applied to individually coat hydrophilic KCl particles, that otherwise agglomerate almost instantaneously following milling [40].

In this study, the process is applied to mill $CaCO_3$ (CC) particles and simultaneously coat them with silica nanoparticles. Thus, prepared $CaCO_3$ particles are extrusion compounded with polypropylene (PP) to test their performance as polymer

additives. Simply milled (without coating) $CaCO_3$ particles and as-received $CaCO_3$ particles are used as references for comparison. It should be mentioned that $CaCO_3$ particles, including those surface-modified with surfactants, have been widely investigated as an additive for PP [45-48]. However, unlike most of the previous studies, herein the $CaCO_3$ particles are coated with silica nano-particles using the unique FEM in-situ simultaneous milling and coating technology. Our previous studies show that the flowability of micron-sized particles can be dramatically improved with the introduction of nano-particle coating. It is of technologically fundamental interest to find out the answer to the following questions:

1. Can the novel process be used to mill and simultaneously coat $CaCO_3$ with nano-particles?
2. Will thus prepared $CaCO_3$ particles have better flowability compared to those without nano-particulate coating?
3. Will the compounded PP and coated $CaCO_3$ have different mechanical properties from those made with PP and uncoated $CaCO_3$?
4. *Finally and most importantly, is there any fractal phenomenon during the fracture of PP composites?*

The main objective of this chapter is to find out the answer to those questions, and especially the last one.

3.2 Experimental

3.2.1 Materials

Polypropylene homopolymer H110-02N (melt index=2.0 g/10 min at 230 °C and 2.16 kg load and density= 0.9 g/cm^3) was supplied by Dow Chemical Company, Midland, MI. Calcium carbonate HUBERCARB® Q40-200 (cubic shape; particle size of 75~380 μm) was obtained from J.M. Huber Corporation, Quincy, IL. Fumed silica AEROSIL® R972

with an approximate particle size of 16 nm and specific area of 110 m^2/g was supplied by Evonik Degussa, Piscataway, NJ.

3.2.2 Simultaneous Milling and Coating of $CaCO_3$

A FEM qualification unit (diameter: 2 inches) manufactured by Sturtevant Inc. (Hanover, MA) is used. Figure 2.2 (a) and (b) show the entire system of the grinding equipment and the cross-sectional view of the qualification FEM unit used, respectively. The three main operating parameters for the FEM process are: solid feed rate, feed pressure and grinding pressure. In our study, the solid feed rate is controlled by a volumetric screw feeder. The air pressures are controlled by pressure regulators.

A simultaneous milling and coating technology using FEM was developed recently [41]. Figure 3.1 shows schematically the simultaneous FEM milling and coating process, which includes two steps: dry coating in a rotating tumbler coater of the original large core/feed particles with nano-particles, and the simultaneous milling and coating process inside the FEM [44].

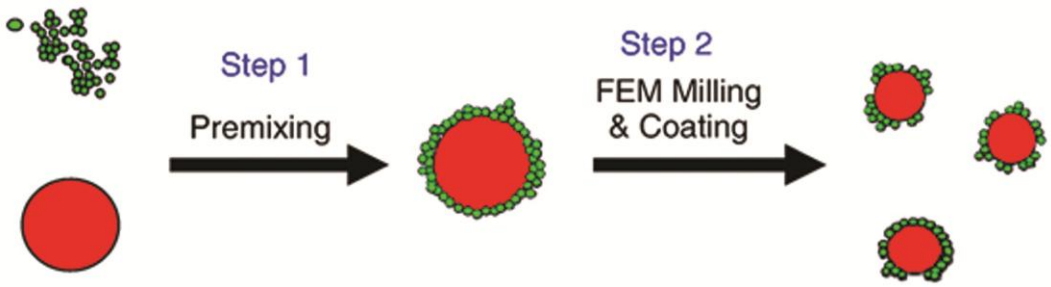

Figure 3.1 Schematic representation of the milling and coating process. [44]

In this study, $CaCO_3$ (CC) particles are first mixed with the desired amount of fumed silica in an in-house-built drum coater operating at 200 rpm for 1 hour. Then, the

pre-coated large $CaCO_3$ particles are fed into the qualification FEM for simultaneous milling and coating. The operating conditions of FEM used in this study are listed in Table 3.1.

Table 3.1 Operating Conditions Used For Milling/Coating in the Qualification FEM

Feed Pressure (kPa)	**Grinding Pressure** (kPa)	**Solid Feed Rate** (g/min)
482.6	482.6	1.5
620.5	620.5	1.5
758.4	758.4	1.5

3.2.3 Characterization of $CaCO_3$ Particles

Field Emission Scanning Electron Microscopy (LEO 1530VP) is used to examine the size and morphology of coated and uncoated particles. The size distribution of particles is determined by an Enhanced Laser Diffraction Particle Size Analyzer (Beckman Coulter LS230). In order to characterize the flowability of FEM milled/coated $CaCO_3$ particles, a Hosokawa powder tester (PT-N)i used to measure their angle of repose (AOR).

3.2.4 Preparation of PP/$CaCO_3$ Composites

PP and $CaCO_3$ are compounded using a Werner & Pfleiderer co-rotating twin screw extruder (ZSK-30, D=30 mm, L/D=44, Coperion Corporation, Ramsey, NJ). The extruder is operated at 125 rpm and the barrel temperature "profile" of 159, 209, 230, 230, 229, 229 °C from the feeding zone to die head. The extrudates are cooled by water, dried and pelletized. Three types of $CaCO_3$, as shown in Table 3.2, are selected as fillers

and compounded into PP. A 90–Ton TOYO Injection Molding Machine (TI-90G, Toyo Machinery & Metal Co. LTD., Hitachi Group, Japan) is used to injection mold samples for the needed ASTM mechanical testing. The temperature profile from the hopper throat to the nozzle is 32, 204, 232, 232, 232, 232 °C. The mold temperature is 32 °C. Tensile, flexural and impact bars of neat PP and the composites are molded to carry out the tests according to ASTM D638, ASTM D790 and ASTM D256 procedures, respectively.

Table 3.2 Three Types of $CaCO_3$ Compounded into the PP Matrix

Filler "code"	**Filler Name**	**Content of Nano-silica** (wt%)	**Operating Parameters in FEM**		
			Feed Pressure (kPa)	**Grinding Pressure** (kPa)	**Solid Feed Rate** (g/min)
cm-CC	coated & milled $CaCO_3$	1	758.4	758.4	1.5
m-CC	milled $CaCO_3$	0	758.4	758.4	1.5
u-CC	un-milled $CaCO_3$	0	-	-	-

3.2.5 Characterization of the Composites

Tensile tests are conducted on a tensile tester (Tinius Olsen) according to ASTM D-638. The speed of test is 5.08 cm/min (2 inch/min). Before conducting tensile testing, a micrometer is used to measure the width and the thickness of the specimens. Five specimens are tested for each composition.

Flexural tests are performed with a flexural tester (Tinius Olsen) according to ASTM D-790. The loading speed is 0.508 cm/min (0.2 inch/min). Before the flexural

testing, the width and the thickness of the specimens are measured with a micrometer. Five specimens from each composition are tested.

Izod impact tests are performed using a plastic impact tester (Tinius Olsen) according to ASTM D-256. Notching is made on a sample notcher (CS-93M-043). Before the impact testing, the thickness of the specimens is measured with a micrometer. Ten specimens from each composition are tested.

Atomic Force Microscopy (AFM) (Digital Instrument Nanoscope III MultiMode Scanning Probe Microscope) and the free software Gwyddion 2.25 are used to analyze the surface fractal dimension (Ds) of the impact-fractured surface of composites.

Field Emission Scanning Electron Microscopy (LEO 1530VP) is used to characterize the fracture surfaces of the Izod and tensile specimens. All SEM specimens are coated with gold to improve the conductivity.

3.3 Results and Discussion

3.3.1 Simultaneous Milling and Coating

Results of previous studies [25] suggest that the feed pressure does not have a significant effect on the mean size and size distribution of product particles. Hence, in the current study the feed pressure of FEM was always set to be the same as the grinding pressure in order to ensure smooth feeding.

From the literature and previous work in our laboratories [29, 49, 50], the effect of solid feed rate on particle size of product is not monotonic. On one hand, particle size may increase with the solid feed rate because of smaller specific energy per particle. On the other hand, it may decrease with increasing solid feed rate because of increasing

collision frequencies. Therefore, there is an optimal solid feed rate for minimum particle size of product for a particular material. In this study, the solid feed rate was fixed at 1.5 g/min.

The mean particle size of pre-coated or uncoated $CaCO_3$ produced under various grinding pressure are shown in Figure 3.2. Figure 3.3 shows the cumulative particle size distributions of $CaCO_3$ pre-coated with 1 wt% of nano-silica and milled under three different grinding pressures. The shapes of cumulative particle size distribution curves of neat $CaCO_3$, $CaCO_3$ pre-coated with 0.5 wt% or 2 wt% of nano-silica and milled under these three grinding pressures are similar to Figure 3.3. Increasing grinding pressure decreases the mean particle size of product due to the higher input energy density. Meanwhile, the particle size distribution of the product is narrowed by increasing grinding pressure. The narrowed size distribution is due to the relatively definite lower particle size for a given particulate material and mill type.

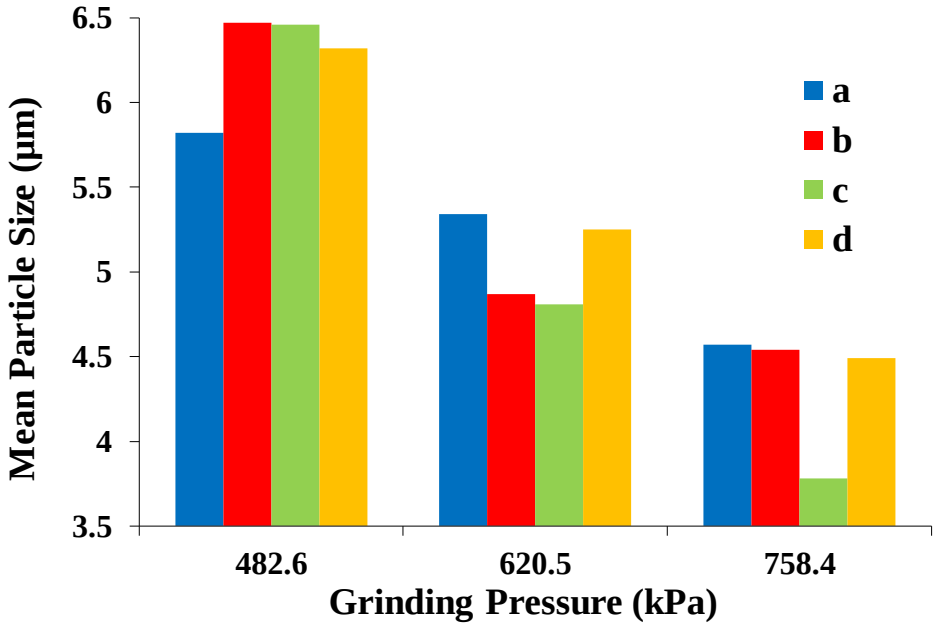

Figure 3.2 The effect of grinding pressure on the mean particle size of the CC product pre-coated with (a) 0 wt%, (b) 0.5 wt%, (c) 1 wt% or (d) 2 wt% of nano-silica.

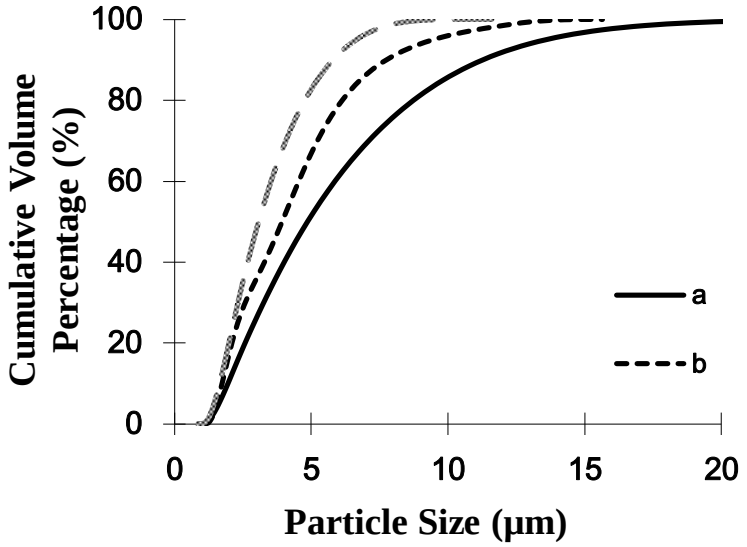

Figure 3.3 Cumulative particle size distribution of CC pre-coated with 1 wt% of nano-silica and milled under grinding pressure of (a) 482.6 kPa, (b) 620.5 kPa, (c) 758.4 kPa.

Figure 3.4 shows the effect of the content of the pre-coating nano-silica on the mean particle size of the milled and coated $CaCO_3$ product particles. Figure 3.5 shows the cumulative particle size distributions of $CaCO_3$ pre-coated with different amounts of nano-silica and milled under the grinding pressure of 620.5 kPa. The shapes of cumulative particle size distribution curves of $CaCO_3$ pre-coated with different contents of nano-silica and milled under grinding pressure of 482.6 kPa and 758.4 kPa are similar to those in Figure 3.5. Under a fixed operating condition, the amount of nano-silica does not significantly affect the product particle size within the concentrations studied, because the elastic inorganic nano-silica dissipates only a very small amount of impact energy during the particle-particle and particle-wall collisions in FEM. It should be mentioned that the particle size of the milled/coated product may increase significantly with increasing the content of soft/ductile polymeric coating materials, such as wax [50].

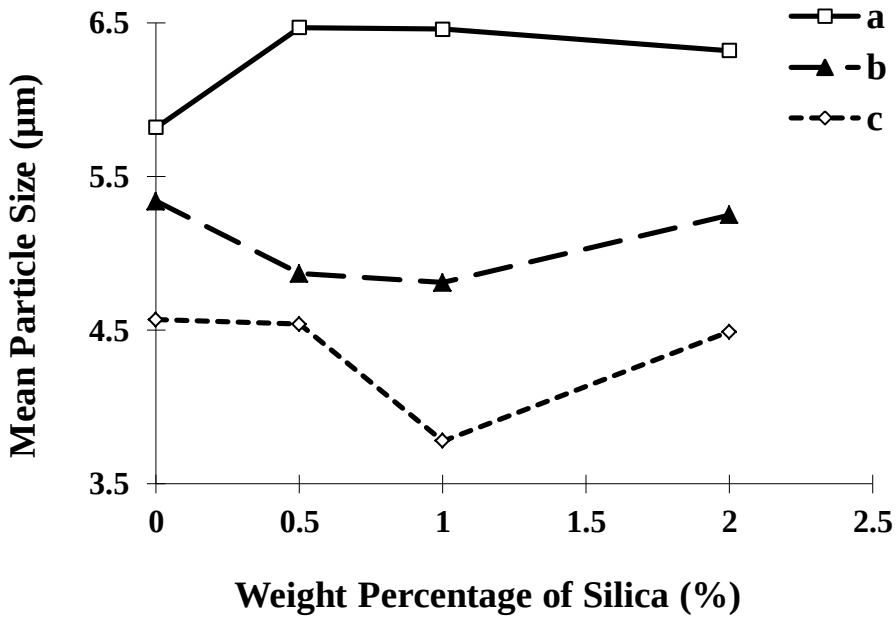

Figure 3.4 The effect of content of nano-silica on the mean particle size of CC product milled under the grinding pressure of (a) 482.6 kPa, (b) 620.5 kPa, (c) 758.4 kPa.

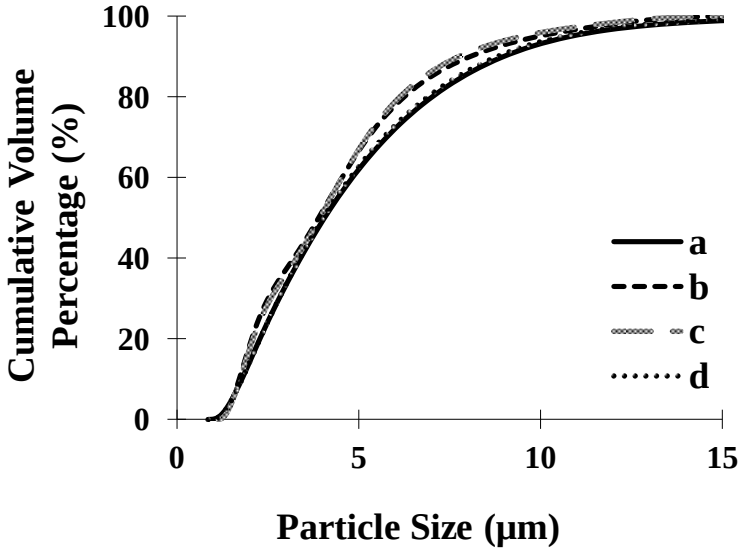

Figure 3.5 Cumulative particle size distribution of CC pre-coated with (a) 0 wt%, (b) 0.5 wt%, (c) 1 wt%, (d) 2 wt% of nano-silica and milled under grinding pressure of 620.5 kPa.

Figure 3.6 shows the morphology of FEM milled and coated $CaCO_3$ particles with different amounts of nano-silica coating material. It can be seen that the surface coverage of $CaCO_3$ increases with the amount of nano-silica. Figure 3.7 indicates that under fixed operating conditions, the nano-silica coating significantly improves the flowability of milled $CaCO_3$ particles and the higher content of nano-silica results in better flowability of the product particles, as evident by the drop of the angle-of-repose in Figure 3.7.

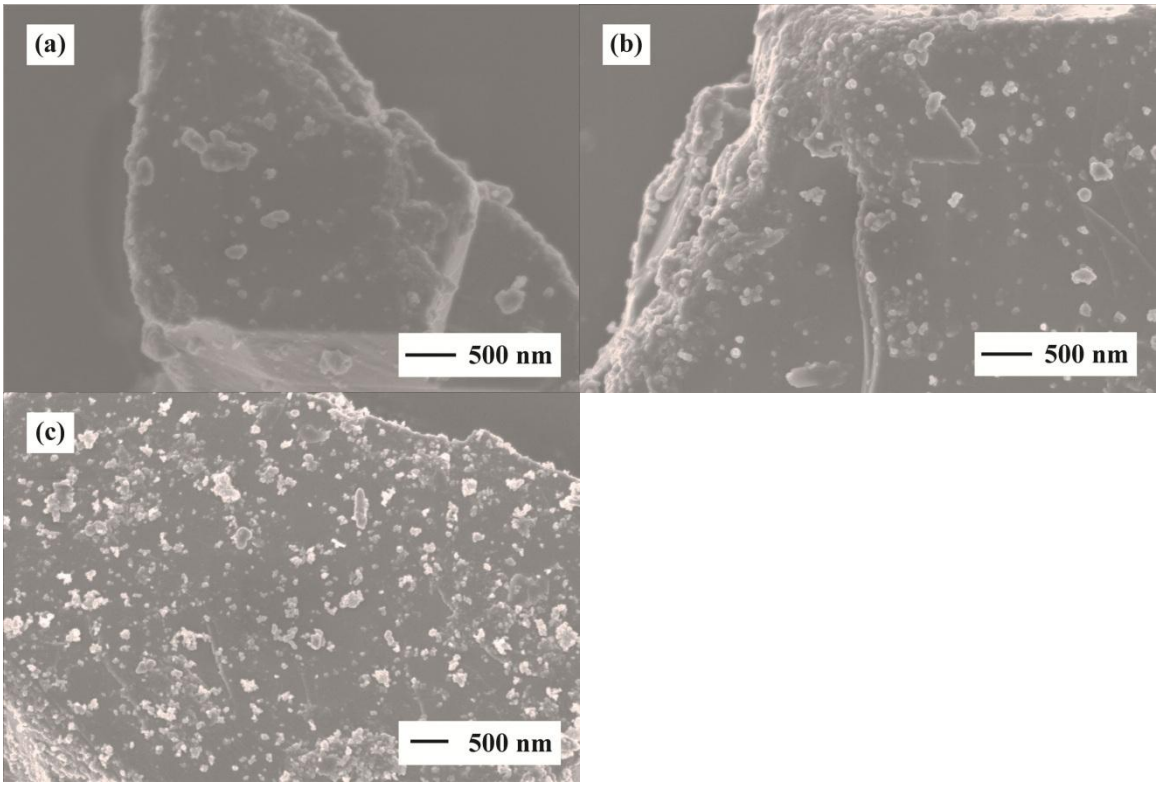

Figure 3.6 The SEM images of the surface of CC coated with (a) 0.5 wt%, (b) 1 wt%, (c) 2 wt% of nano-silica and milled under the grinding pressure of 758.4 kPa.

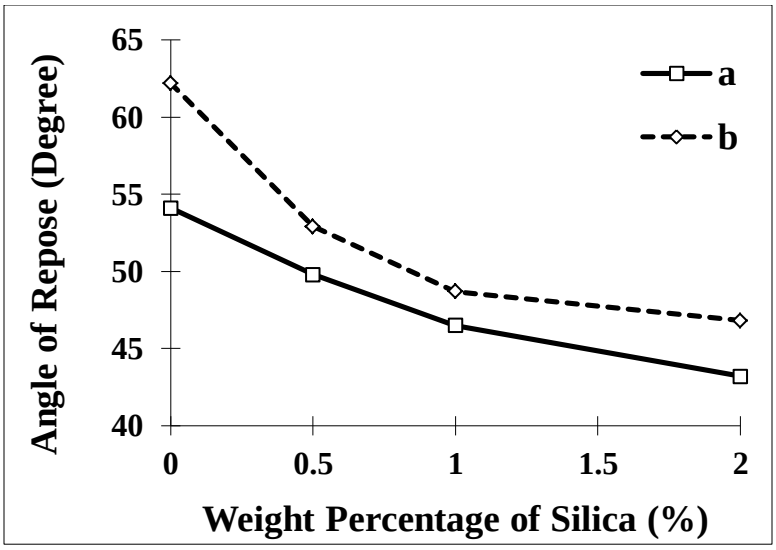

Figure 3.7 The effect of content of nano-silica on the angle of repose of CC milled under the grinding pressure of (a) 482.6 kPa, (b) 758.4 kPa.

To test its performance as filler, $CaCO_3$ pre-coated with 1 wt% of nano-silica and milled under the grinding pressure of 758.4 kPa (coated and milled $CaCO_3$) is extrusion-compounded with polypropylene. As a comparison, uncoated $CaCO_3$ milled under the grinding pressure of 758.4 kPa (milled $CaCO_3$ with nano-silica coating) and as-received $CaCO_3$ (un-milled $CaCO_3$ without coating) are also used as fillers. The designations of the different $CaCO_3$ are specified in Table 3.2.

3.3.2 Mechanical Properties of Neat PP and the Composites

3.3.2.1 Tensile Properties of the Composites. Tensile properties of the three composite materials and the neat PP are given in Figure 3.8-3.10. Increasing the content of $CaCO_3$ increases the modulus and decreases the yield stress of the composite materials. The increase of modulus suggests that the $CaCO_3$ particles do not de-bond at low strains. On the other hand, the decrease of the yield strength is possibly due to increase in the stress concentration at the inter-phase during tensile testing, which has been observed in many

other composites [45]. PP/cm-CC composite has higher modulus than the other two composites due to the smaller particle size and more uniform dispersion of the fillers inside the polymer matrix. In contrast, larger filler particles have smaller specific surface area and poorer interaction between fillers and polymer matrix, resulting in earlier de-bonding of the particles and lower modulus value. Figure 3.11 shows the fracture surfaces of tested tensile bars of the three composite materials. m-CC tends to agglomerate due to its poorer flowability compared to cm-CC. Consequently, the agglomerated m-CC particles perform like large particles. As a result, the modulus of PP/m-CC composite is close to that of PP/u-CC composite.

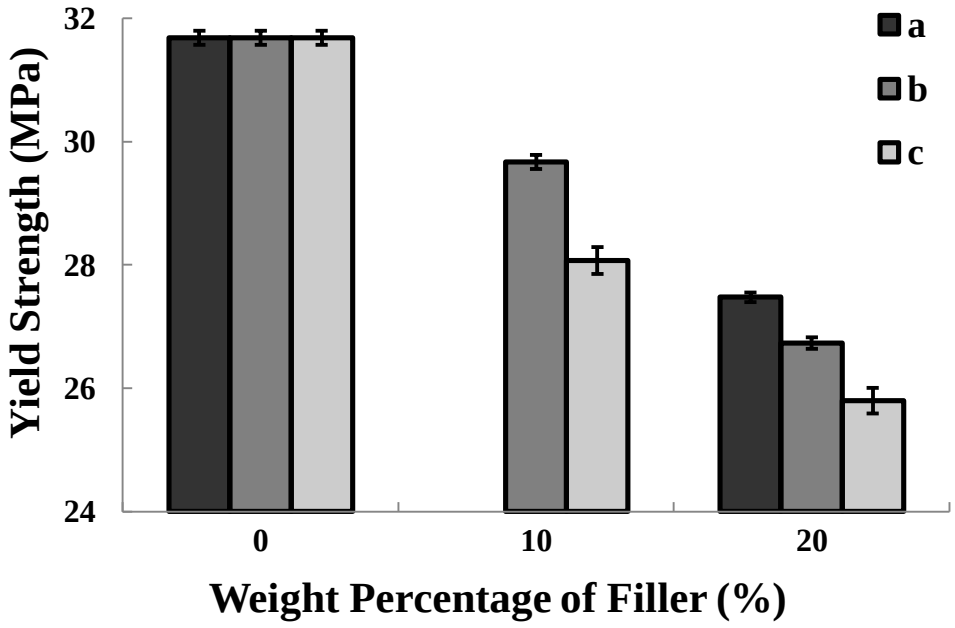

Figure 3.8 The effect of content of fillers on the yield strength of the composites, (a) PP + un-milled CC, (b) PP + CC milled under the grinding pressure of 758.4 kPa, (c) PP + CC pre-coated with 1 wt% of nano-silica and milled under the grinding pressure of 758.4 kPa.

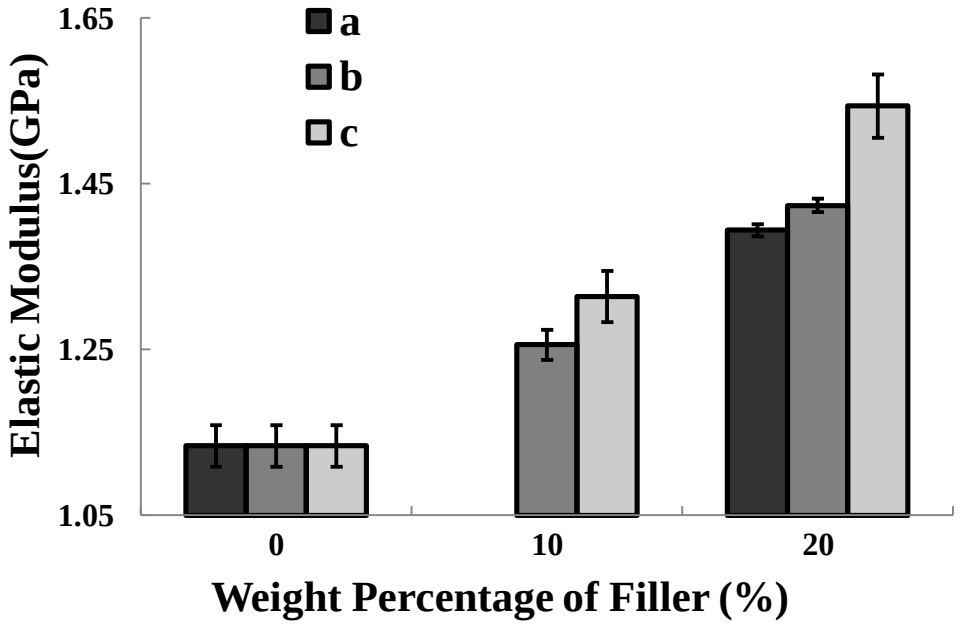

Figure 3.9 The effect of content of fillers on the elastic modulus of the composites, (a) PP + un-milled CC, (b) PP + CC milled under the grinding pressure of 758.4 kPa, (c) PP + CC pre-coated with 1 wt% of nano-silica and milled under the grinding pressure of 758.4 kPa.

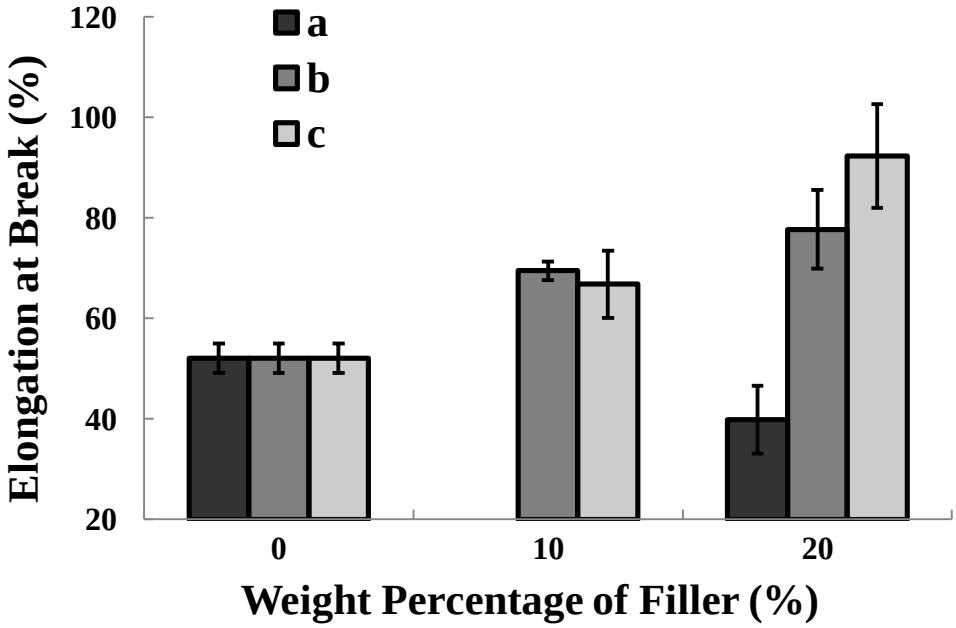

Figure 3.10 The effect of content of fillers on the elongation at break of the composites, (a) PP + un-milled CC, (b) PP + CC milled under the grinding pressure of 758.4 kPa, (c) PP + CC pre-coated with 1 wt% of nano-silica and milled under the grinding pressure of 758.4 kPa.

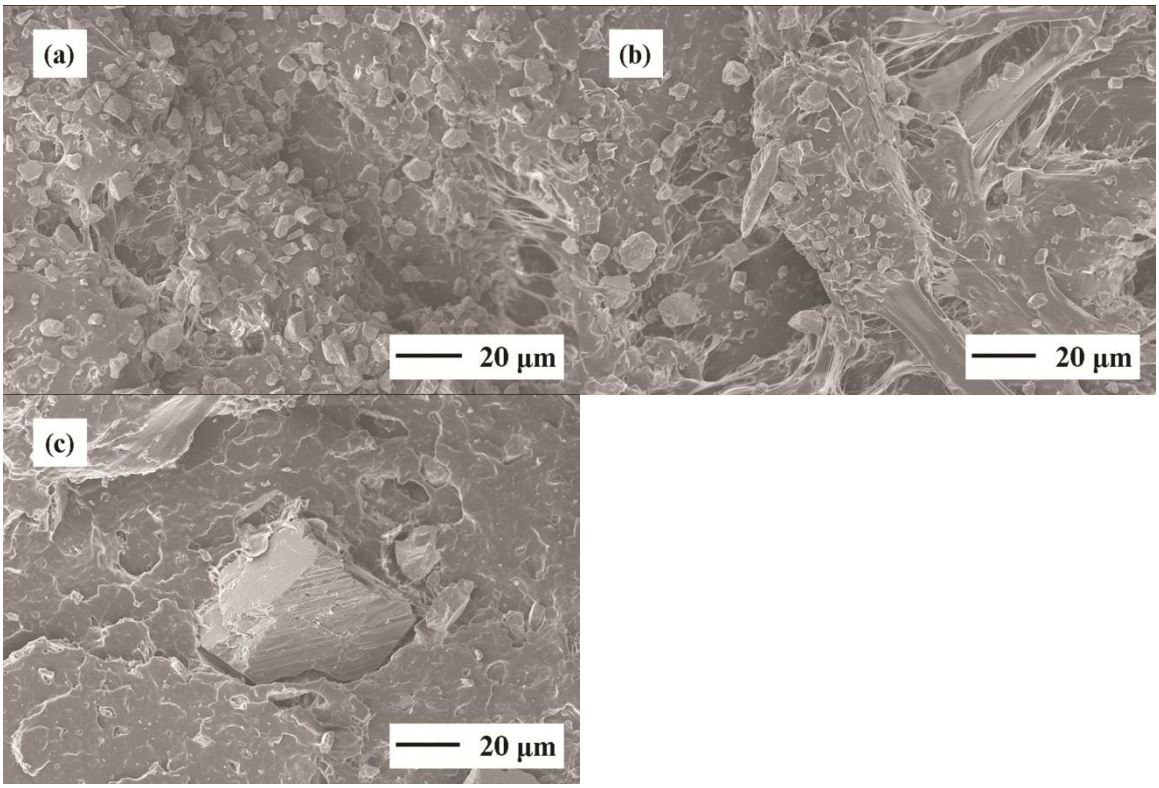

Figure 3.11 SEM micrographs of fracture surface of tested tensile bar. (a) PP+20 wt% coated & milled CC; (b) PP+20 wt% milled CC; (c) PP+20 wt% un-milled CC.

The elongation at break of PP/cm-CC composite and PP/m-CC composite increases as the content of filler increases due to the formation of shear bands which absorb large amount of energy during deformation [45]. The elongation at break of PP/20 wt% cm-CC composite is larger than that of PP/20 wt% m-CC because of the better dispersion of cm-CC in polymer matrix. Figure 3.12 shows the cross sections normal to the stretch direction of tested tensile bars. De-bonded filler particles are found in elongated cavities. Inside PP/m-CC composites, agglomerates consisting of several filler particles are often found in one cavity (highlighted with black circles in Figure 3.12 (b)). The agglomeration decreases the contribution of filler particles to the formation of shear bands, resulting in smaller elongation at break of composite. The phenomena can be attributed to the following reasons: 1) Agglomeration makes the particle distribution

inside PP less homogeneous; 2) Agglomeration may cause the effective aspect ratio of particles farther away from unity, which in turn leads to higher stress concentration; 3) Large voids due to agglomeration would act as initiation sites for the fracture process, weakening the material. Nevertheless, the incorporation of *milled $CaCO_3$ particles*, irrespectively to whether they are coated or not, leads to larger elongation at break of PP. In contrast, the elongation at break of PP/u-CC composite is smaller than that of neat PP. The latter is probably due to the fracture site of PP/u-CC initiated by large filler particles.

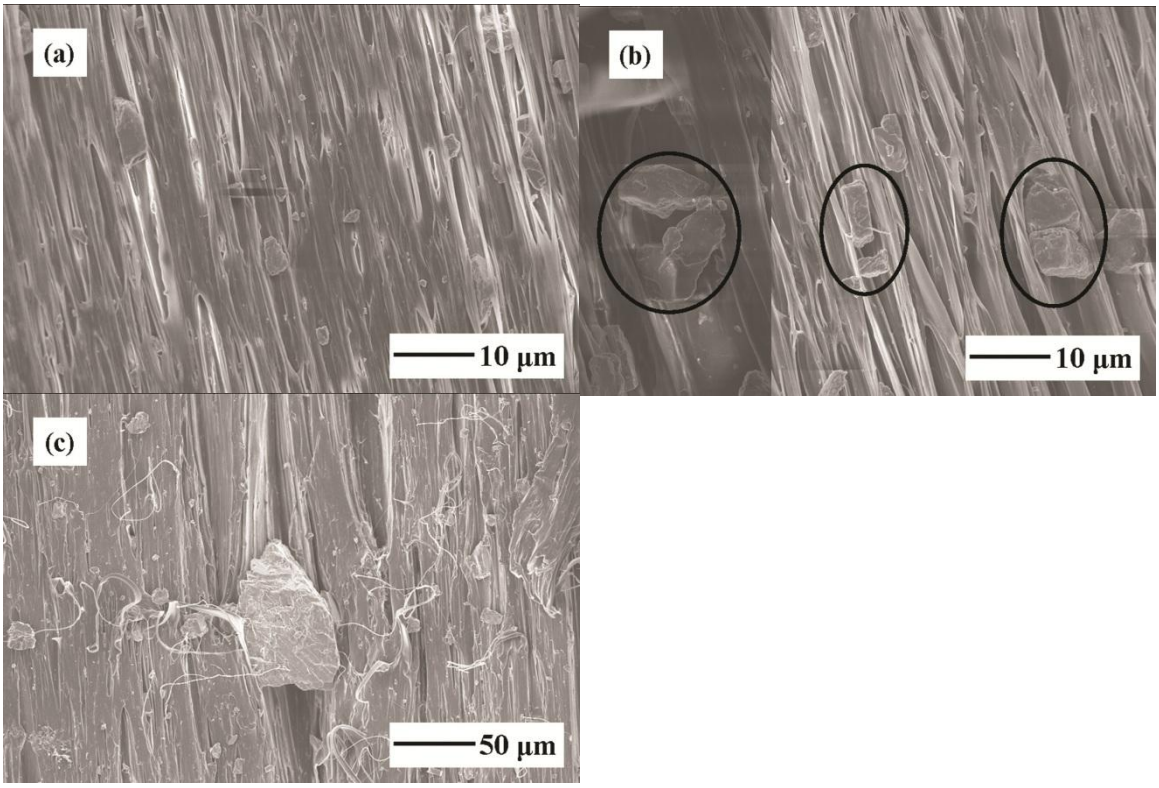

Figure 3.12 SEM micrographs of cross section of stretch direction of tested tensile bars. (a) PP+20 wt% coated CC; (b) PP+20 wt% CC; (c) PP+20 wt% un-milled CC.

3.3.2.2 Impact Strength of the Composites. Figure 3.13 shows the notched impact strength of three composites. Two types of milled $CaCO_3$ particles, cm-CC or m-CC, improve the impact strength of PP. On the contrary, the introduction of u-CC into PP has

no effect on the impact strength of PP/u-CC composite. The impact strength of PP/cm-CC composite increases as the content of filler increases from 10 wt% to 20 wt%; while PP/m-CC composite's impact strength essentially does not. During high strain rate deformation, most energy is consumed in the fracture initiation stage and at the very next to the notch root [46]. Fillers with small particle size and uniform dispersion in polymer matrix can form an inter-particle ligament-like network structure, which toughens the material [47]. In the composites with low content of filler such as 10 wt%, the filler particles of cm-CC and m-CC disperse quite well in the polymer matrix, resulting in the mechanism of plastic deformation of the inter-particle ligaments. Figure 3.14 shows SEM micrographs on the notch roots of the impact-fractured surface of composites. The white arrows indicate the crack-propagation direction. Figure 3.14 (a) and (b) are from the composites of PP/10 wt % of cm-CC and PP/10 wt % of m-CC. De-bonding of the CC particles from the matrix is observed in the plastic deformation region. Consequently, the composites become tougher.

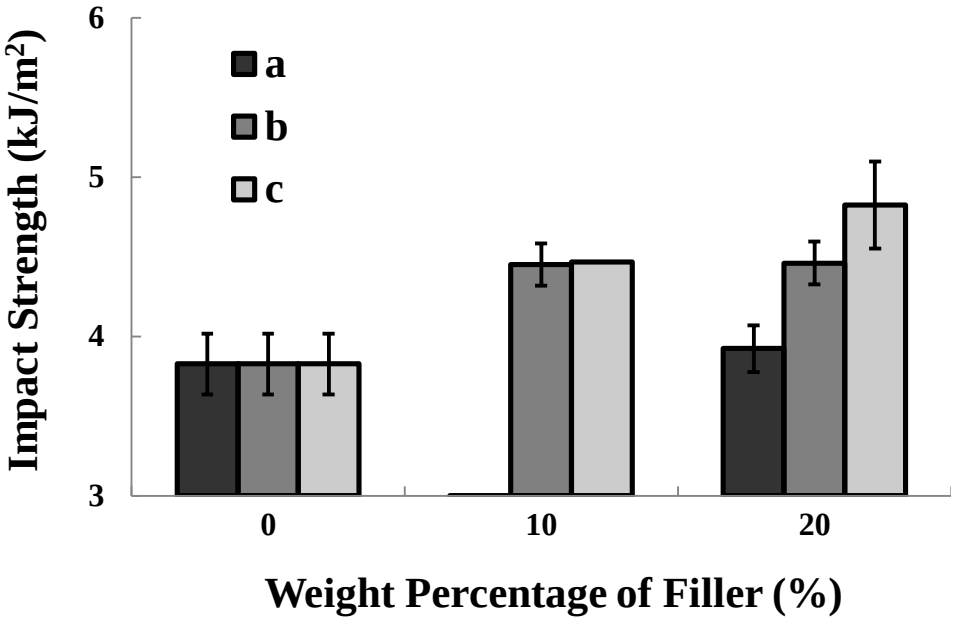

Figure 3.13 The effect of content of fillers on the impact strength of the composites, (a) PP + un-milled CC, (b) PP + CC milled under the grinding pressure of 758.4 kPa, (c) PP + CC pre-coated with 1 wt% of nano-silica and milled under the grinding pressure of 758.4 kPa.

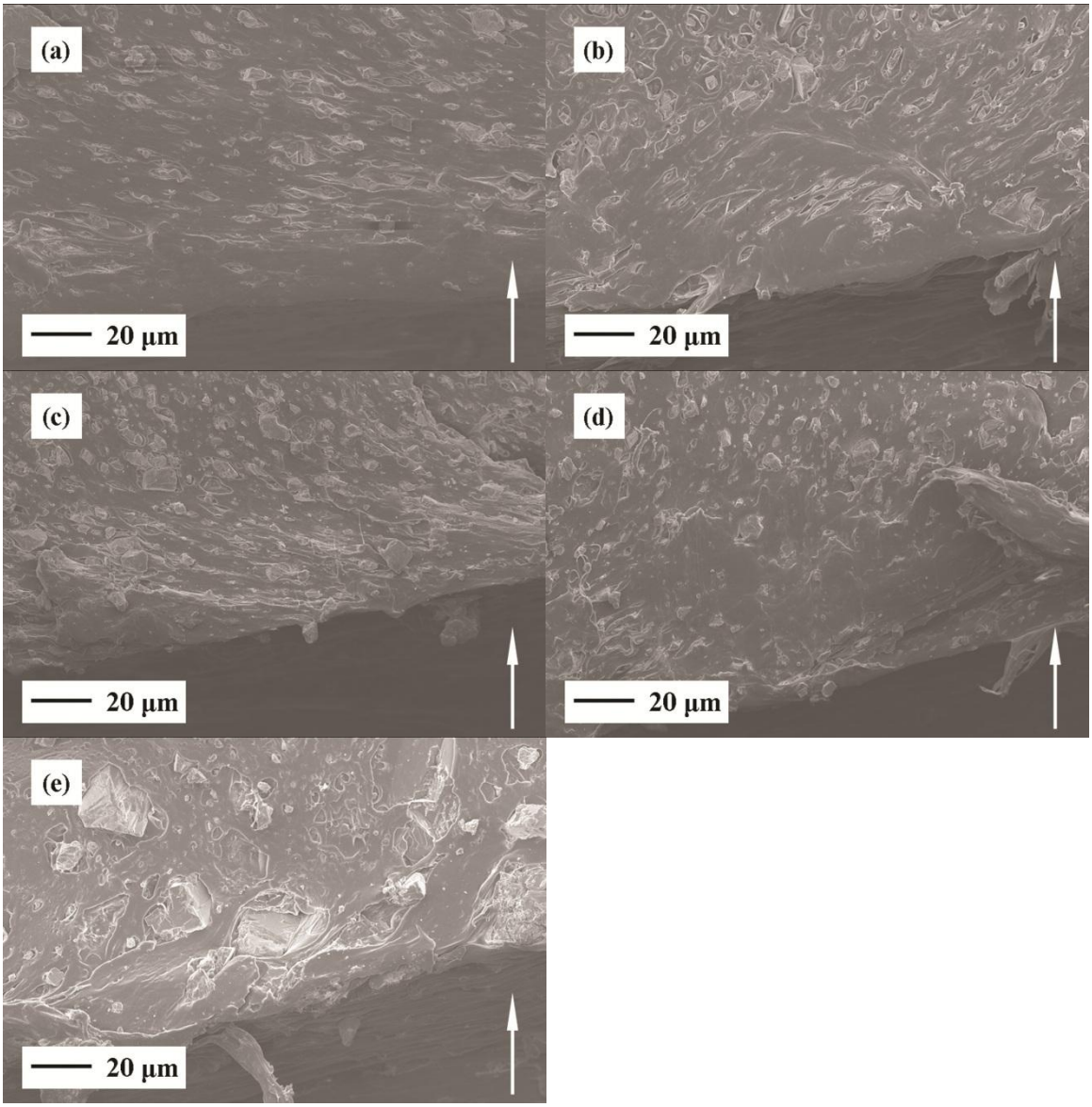

Figure 3.14 SEM micrograph on the notch roots of the impact-fractured surface of composites. The arrows indicate the crack-propagation direction. (a) PP/10 wt% coated & milled CC composite; (b) PP/10 wt% milled CC composite; (c) PP/20 wt% coated & milled CC composite; (d) PP/20 wt% milled CC composite; (e) PP/un-milled CC composite.

Increasing the content of cm-CC particles further improves the impact strength of the composite due to the increase of plastic deformation as shown in Figure 3.14 (c). In contrast, increasing the content of m-CC particles also leads to more agglomeration, which provides a convenient trigger for brittle behavior, consequently weakening the

toughening effect. Hence, changing the content of m-CC from 10 to 20% does not affect the impact strength significantly. Due to its large size and sharp edges, u-CC particles cannot improve the impact strength of composite.

3.3.3 Fractal Dimension of Impact-Fractured Surface

The fractal characterization, which relates macro-mechanical properties to microstructure, is discussed in Chapter 2 for $CaCO_3$ and KCl, both of which are brittle materials. Furthermore, the fracture analysis is presented to apply only to brittle materials. The deformation of polymer composites during tensile testing indicates both elastic and plastic deformations and the failure is ductile fracture, and fractal characterization used in Chapter 2 cannot be applied here. *However, all the composites showed signs of brittle fracture behavior during Izod impact test*, where *the surfaces appeared relatively flat and no significant whitening was observed*, as shown in Figure 3.14. That is because Izod toughness, which is measured during deformation at high strain rates, is a measure of the energy required to propagate a crack rapidly. Even in the PP/20 wt% cm-CC composite with higher impact energy, there are few signs of plastic deformation present. [47] Therefore, for modeling the impact-fractured surface of polymer composites by a fractal surface, AFM and the free software Gwyddion 2.25 are again used to *measure the fractal dimension (D_s) of the composites' impact-fractured surfaces*.

As with the $CaCO_3$ and KCl particulates, for every composite, three locations around the very next to the notch root of the impact-fractured surface are selected. For every location, three areas (50×50 μm, 10×10 μm and 5×5 μm) are scanned. Table 3.3 shows the fractal dimension of different composites' impact-fractured surface.

Table 3.3 Izod Impact Strength and Impact-fractured Surface Fractal Dimension of Different Composites

	Izod Impact Strength (kJ/m^2)	**ln(Izod Impact Strength)** (kJ/m^2)	**Fractal Dimension of Impact–fractured surface (D_s)**	**D_s-2**
Neat PP	3.85	1.35	2.13	0.13
PP+10% m-CC	4.43	1.49	2.3	0.30
PP+10% cm-CC	4.48	1.50	2.31	0.31
PP+20% m-CC	4.48	1.50	2.31	0.31
PP+20% cm-CC	4.80	1.57	2.41	0.41
PP+20% u-CC	3.90	1.36	2.15	0.15

Table 3.3 indicates that *there is a relationship between the Izod impact strength* of the five polymer composite samples *and the fractal dimension increment of impact generated surface, D_s-2*. Thus, this relationship in a plot form of ln[Izod Impact Strength] vs. D_s is shown on Figure 3.15. This relationship also follows Equation (2.30).

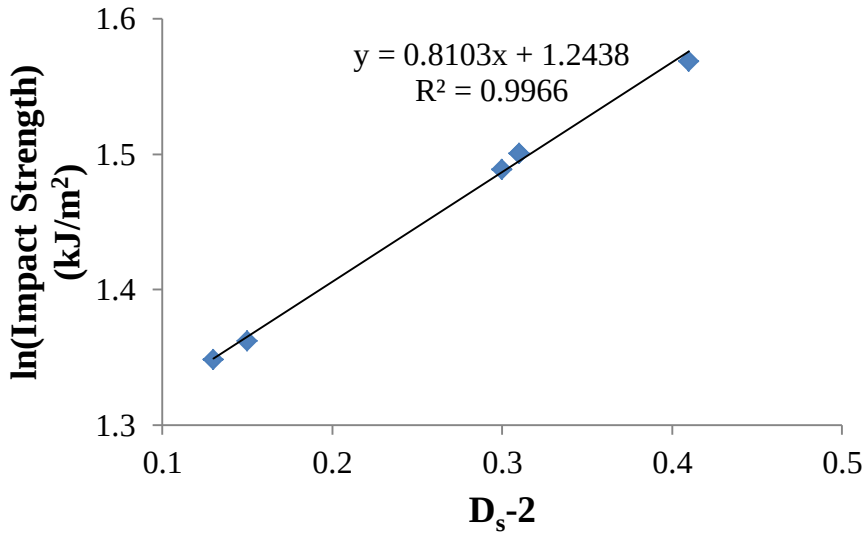

Figure 3.15 The evolution of ln(impact strength) with the fractal dimension increment of impact-fractured surface of composites.

The semi-log *fit* between the impact strength, which is a property depending on a number of physical attributes of the composite samples, and the fractal dimension increment is quite good. It is also reminiscent of Figure 1.1 of the work of Mandelbrot and his associates, which *reported, for the first time*, the relationship of a mechanical property depending on the sample crystalline morphology, which is the energy required for impact fracture, to the fractal dimension increment values of the fractured 300-grade Maraging steel annealed at different conditions. Thus, for comparison purposes, Figure 1.1 is *replotted as* ln[Impact Energy] vs. D_s-2, as shown as Figure 3.16.

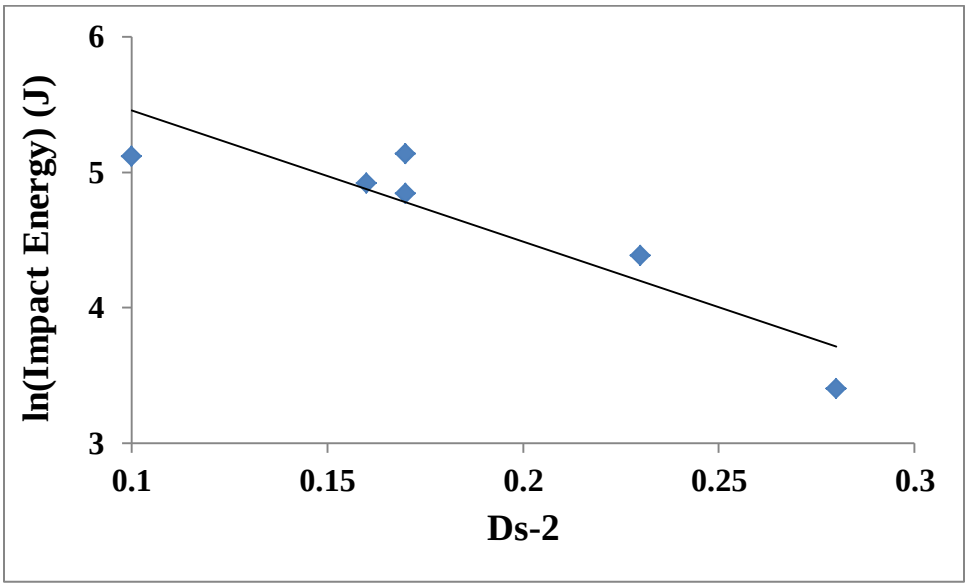

Figure 3.16 The natural logarithm of impact energy vs. fractal dimension increment.

In comparing Figure 3.15 and 3.16, the following are noted: First, the results on Figure 3.15 are another example of *a profound relationship* of a structural morphology-dependent property, the impact strength, and the fractal dimension of impact fractured surface, D_s-2. Of course the relationships existing between (a) the energy needed to fracture annealed steel samples and (D_s-2) of the corresponding fractured surfaces, and (b) the impact strength of various PP/CC composites and the (D_s-2) of the corresponding

fractured surfaces are *different*. They are different, because in the Maraging steel case, an (D_s-2) increase indicates a *rougher fracture surface*, which is due to a *coarser* crystalline morphology. As the crystalline morphology coarsens, the Maraging steel becomes *more brittle* and, consequently requires less energy to impact fracture. On the other hand, for composites of PP/CC samples in this study, as fractured surface roughness and consequently (D_s-2) increases, so does the impact strength of the corresponding composite samples. The surface roughness (D_s) at the location just adjacent to the notch of the sample was measured. The reason for this is that during high strain rate deformation, most of the impact energy needed to fracture the composite sample is consumed in the fracture initiation stage and at the very next to the notch root. As mentioned before, fillers with small particle size and uniform dispersion in the polymer matrix can form an inter-particle ligament-like network structure, which toughens the material. The reason that in samples (a), (b), (c) and (d) in Figure 3.14, the D_s values are high, 0.31, 0.3, 0.41 and 0.31, respectively, is that the roughness is due to the inter-particle "ligaments" formed (see Figure 3.14 (c)). The higher the number of such inter-particle ligaments the tougher the composite is and the higher the D_s of the fractured surface next to the notch.

Equally important to the work conducted in this dissertation are the following two statements:

- Any fracture mechanical property which is dependent on the materials morphology (crystalline morphology or polymer-filler interaction regions) can be characterized by the (D_s-2) of the corresponding fractured surfaces, because they both depend on roughness ramifications.
- The experimental result proving that for brittle materials, the milling process does not affect surface roughness, D_s, implies that the milled particles have a tremendously high specific surface area, because their surfaces are not smoother than the original ones, and thus they are very effective. Furthermore, this is shown

by the (D_s-2) value of 0.15 and 0.31 for PP+20% u-CC and PP+20% m-CC, respectively. The additional effect of coating with nano-silica is to decrease $CaCO_3$ agglomeration and thus increase the number of inter-particle ligaments (increasing impact strength) and fractured surface roughness at the region next to the notch.

3.4 Conclusions

In this section of the dissertation, a simultaneous milling and coating method is applied for the first time to prepare nano-silica-coated $CaCO_3$ additives for polymer composite materials. The effects of the grinding pressure and content of nano-silica coating on $CaCO_3$ particle size are studied. The angle-of-repose data suggest that $CaCO_3$ additives made from this simultaneous milling and coating FEM process are less cohesive and have improved flowability. As a result, it is easier to consistently feed the additives into the extruder and a more uniform and extensive dispersion of the additives inside the polymer is achieved, compared to simply milled particles.

The composites made of PP and these specially prepared $CaCO_3$ particulates have better mechanical properties, such as larger elongation at break, higher elastic modulus and improved impact strength, compared to the simply milled $CaCO_3$.

Although the deformation of polymer composites during tensile testing is plastic characterizing ductile fracture, fractal characterization can be applied to model the *impact-fractured surface* of polymer composites in the notch vicinity by a fractal surface due to the *brittle fracture* behavior during Izod impact test. The results show that the fractal dimension of composite's impact-fractured surface increases with the Izod impact strength. Their relationship is represented by a linear fit of semi-log, following Equation (2.30), which shows that the impact-fractured surface of composites can be modeled very well by a fractal surface. For the polymer composites of PP and $CaCO_3$, the fractal

dimension of the fractured surface can be applied to characterize the Izod impact strength, in a manner similar to that presented in the pioneering 1984 *Nature* publication on the fundamental relationship between the impact energy of annealed metal samples and the (D_s-2) values of their impact fractured surfaces, because they both depend on the coarseness of the polycrystalline morphology.

The different trends of impact toughness with the increasing fractal dimension of fractured surface between the results in this study and the work in Mandelbrot et al. are believed to be the results of the different fracture micro-mechanisms.

CHAPTER 4

SUMMARY AND FUTURE WORK

The research presented in this dissertation has focused on the investigation of the fracture phenomena during the milling process of inorganic particulates and brittle fracture of polymer composites using fractal theory. Due to the self-similar properties shown in the particle fracture during fluid energy milling process, including the self-similar surface morphology of raw and ground particles and the fractal behavior in PSD of fluid energy milled products, successful attempts are made to apply fractal theory to build a linkage between the evolution of macro-mechanical property of impact toughness and the mirco-structural property of fractal dimension of fractured surface.

Major achievements and conclusions obtained from the results in the work of this dissertation are:

- Brittle milled particulates have self-similar shape to the original particulates, which points to the self-similarity property of fractals. PSD (particle size distribution) of milled particulates obeys Power Law expression. This allows analyzing size reduction efficiency and specific kinetic energy of particulates during SEFM milling using fractal methods.
- Under the same feed pressure and as impact numbers increase, KCl can be milled to smaller particle sizes than $CaCO_3$. Moreover, the fractal dimension describing the PSD of KCl increases faster than that of $CaCO_3$, and KCl particles, when milled under the same conditions, generate larger surface area than $CaCO_3$. The grindability of $CaCO_3$ predominantly affected by the attrition in nozzle is much smaller than that of KCl.

  The results from AFM show that the surfaces of $CaCO_3$ and KCl particles are modeled very well by fractal surfaces. The larger surface fractal dimension of $CaCO_3$ particles over KCl particles indicates that the roughness of $CaCO_3$ particles' surface is higher than that of KCl particles' surface. The quantitative results do indeed agree with the qualitative appearances of roughness shown in SEM images of particles. For the materials of $CaCO_3$ and KCl, a relationship between the macro-mechanical property of energy per unit surface area for fracture and the micro-structural property of roughness of particle surface,

characterized by the fractal dimension of fracture surface, is constructed. The energy per unit surface area for fracture increases with fractal dimension of the fracture surface, which is consistent with the Equation (2.30) derived from Griffith energy balance concept.

- A simultaneous milling and coating method is applied for the first time to prepare nano-silica-coated $CaCO_3$ additives for polymer composite materials. The angle-of-repose data suggest that $CaCO_3$ additives made from this FEM process are less cohesive and have improved flowability. As a result, it is easier to consistently feed the additives into the extruder and a more uniform and extensive dispersion of the additives inside the polymer is achieved, compared to simply milled particles. The composites made of PP and this specially prepared $CaCO_3$ have better mechanical properties, such as larger elongation at break, higher elastic modulus and improved impact strength, compared to the simply milled $CaCO_3$.
- Although the deformation of polymer composites during tensile testing is resulting in ductile fracture, fractal characterization can be applied to model the impact-fractured surface of polymer composites in the region next to the notch by a fractal surface due to the brittle fracture behavior during Izod impact test. The results show that the Izod impact strength increases with the fractal dimension of composite's impact-fractured surface. Their relationship is a linear fit of semi-log according to Equation (2.30), which shows that the impact-fractured surface of composites can be modeled very well by a fractal surface. For the polymer composites of PP and $CaCO_3$, the fractal dimension of fractured surface can be used to characterize the Izod impact strength. The different trends of impact toughness with the increasing fractal dimension of fractured surface between the results in this study and the work in Mandelbrot et al. are believed to be the results of the different fracture micro-mechanisms.

For future work of the fractal behavior during particulate fracture, more brittle materials, including inorganic particles, such as NaCl and talc, and organic drug particles, such as Guaifenesin and Indometacin, will be studied using the SEFM milling process to study the self-similar properties in these materials and processes. The goal is to build a quantitative relationship between the macro-mechanical property of energy per unit surface area for fracture and the micro-structural property of roughness of particle surface and check the prediction's correctness.

For the investigation of brittle fracture of polymer composites, increasing filler content, introducing different kinds of fillers, applying more kinds of polymers are

planned to do to convince the prediction that fractal dimension of fractured surface can characterize the notched impact toughness of polymer composites.

Preliminary work by this investigation has shown that ductile materials are hard to mill with FEM processes and, due to the presence of plastic deformation will be difficult to show fractal properties on fractured surfaces.

APPENDIX A

A BRIEF ACCOUNT OF THE MATHEMATICS OF FRACTALS

The mathematics behind fractals began to take shape in the 17th century when the mathematician and philosopher Gottfried Leibniz considered recursive self-similarity (although he made the mistake of thinking that only the straight line was self-similar in this sense). [51]

It was not until 1872 that a function appeared whose graph would today be considered fractal. This was when Karl Weierstrass [1] gave an example of a function with the non-intuitive property of being everywhere continuous but nowhere differentiable. In 1904, Helge von Koch, dissatisfied with Weierstrass's abstract and analytic definition, gave a more geometric definition of a similar function, which is now called the Koch curve.[52] In 1883, Georg Cantor gave examples of subsets of the real line with unusual properties—these Cantor sets are also now recognized as fractals.[16] Although Cantor himself defined the set in a general, abstract way, the most common modern construction is the Cantor ternary set shown in Figure A.1, built by removing the middle thirds of a line segment.[53] Wacław Sierpiński constructed his triangle (shown in Figure A.2) in 1915 and, one year later, his carpet. Sierpinski carpet is a generalization of the Cantor set in two dimensions, shown in Figure A.3. [54].

The idea of self-similar curves was taken further by Paul Pierre Lévy, who, in his 1938 paper Plane or Space Curves and Surfaces Consisting of Parts Similar to the Whole described a new fractal curve, the Lévy C curve shown in Figure A.4. [55].

Figure A.1 Producing a Cantor ternary set by iterative removal of the central 1/3 of line segments. Six iterations are shown from top to bottom. [56]

Figure A.2 Sierpinski triangle evolution in which each iteration removes one-quarter of the remaining area as a series of ever-smaller triangles. Four iterations are shown from left to right. [57]

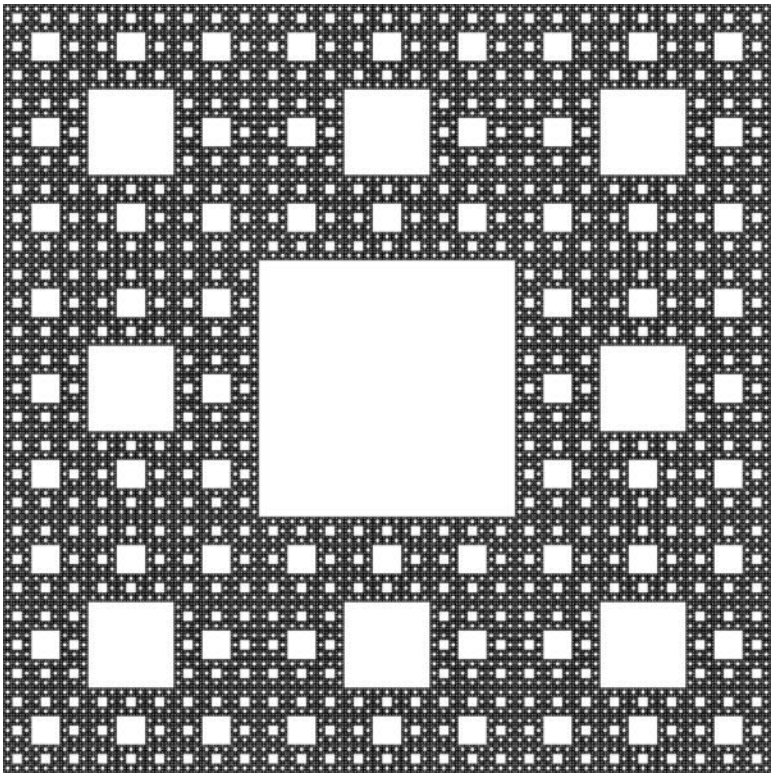

Figure A.3 Sierpinski carpet. [58]

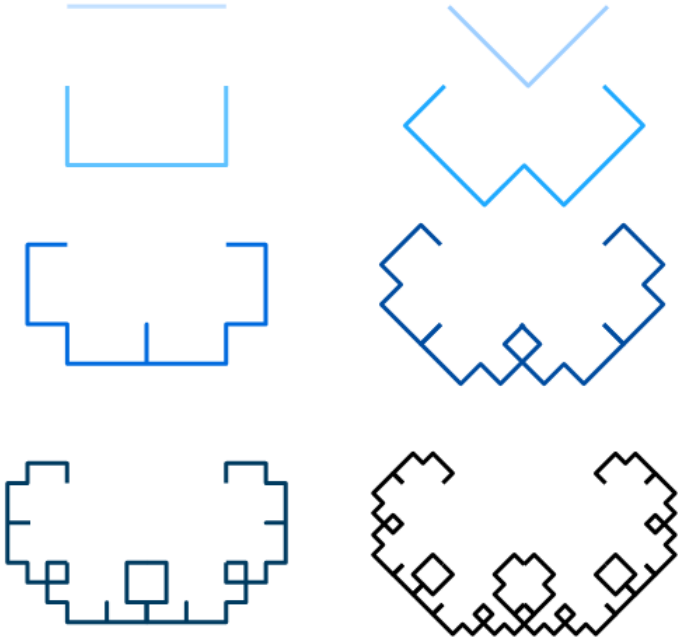

Figure A.4 First eight stages in the construction of a Levy C curve. [59]

Iterated functions in the complex plane were investigated in the late 19th and early 20th centuries by Henri Poincaré [60], Felix Klein [61], Pierre Fatou [62] and Gaston Julia [63]. Without the aid of modern computer graphics, however, they lacked the means to visualize the beauty of many of the objects that they had discovered.

In the 1960s, Benoit Mandelbrot started investigating self-similarity in papers such as How Long Is the Coast of Britain? Statistical Self-Similarity and Fractional Dimension, [3] which built on earlier work by Lewis Fry Richardson [64]. Finally, in 1975 Mandelbrot coined the word "fractal" from the Latin adjective fractus. The corresponding Latin verb frangere means “to break:” to create irregular fragments. [1] The word “fractal” is to denote an object whose Hausdorff–Besicovitch dimension, to be introducded below, is greater than its topological dimension. Mandelbrot illustrated this mathematical definition with striking computer-constructed visualizations. These images [1] (shown as Figure A.5~A.8) captured the popular imagination; many of them were

based on recursion, leading to the popular meaning of the term "fractal". [65] Among them, the Mandelbrot set is the most popular fractal, probably the most popular object of all contemporary mathematics. Some people claim that it is not only the most beautiful but also the most complex object which has been seen, i.e., made visible. [6]

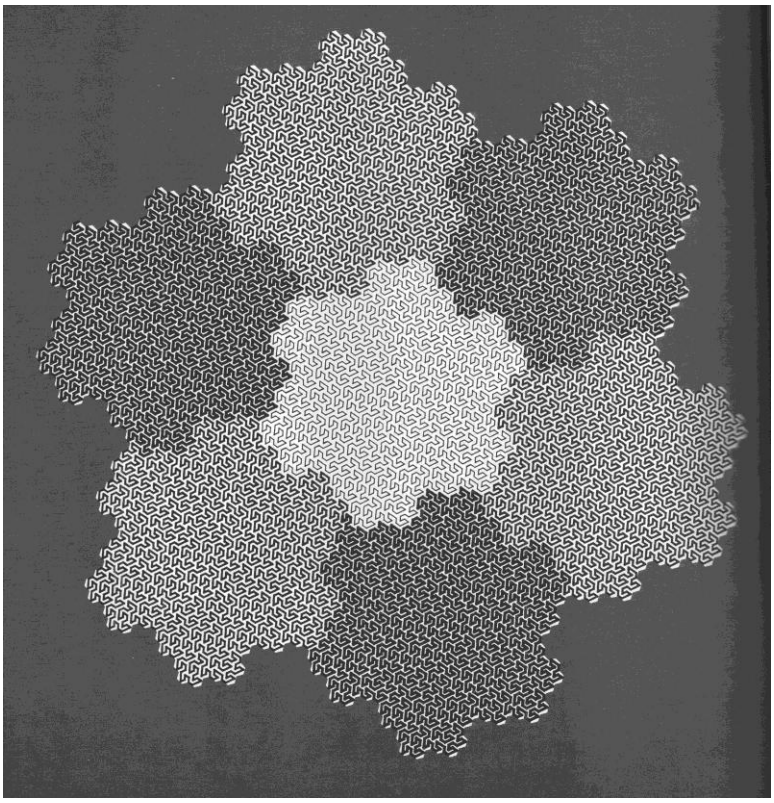

Figure A.5 Alternative Koch island and lake (coastline dimension D=log9 / log7~1.1291). [1]

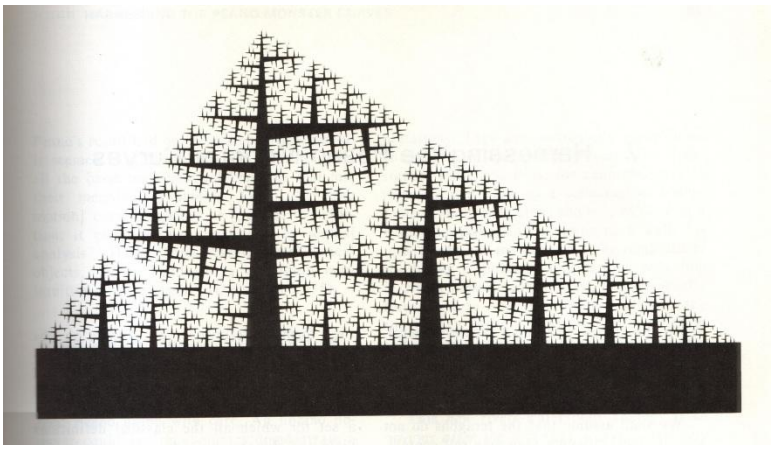

Figure A.6 Self-similarity with unequal parts, *D*~1.8797. [1]

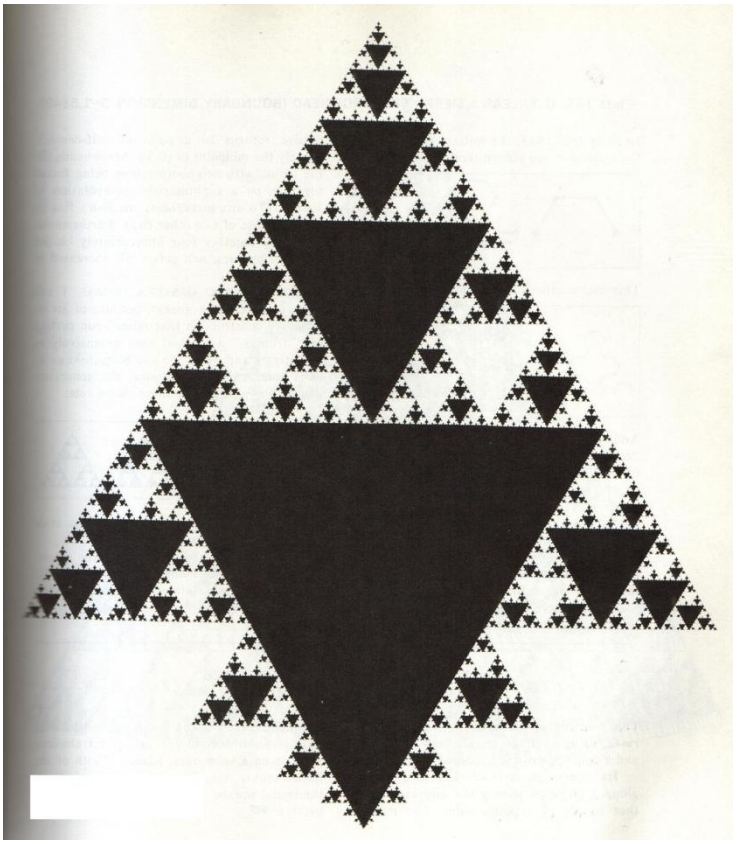

Figure A.7 Sierpinski arrowhead (boundary dimension *D*~1.5849). [1]

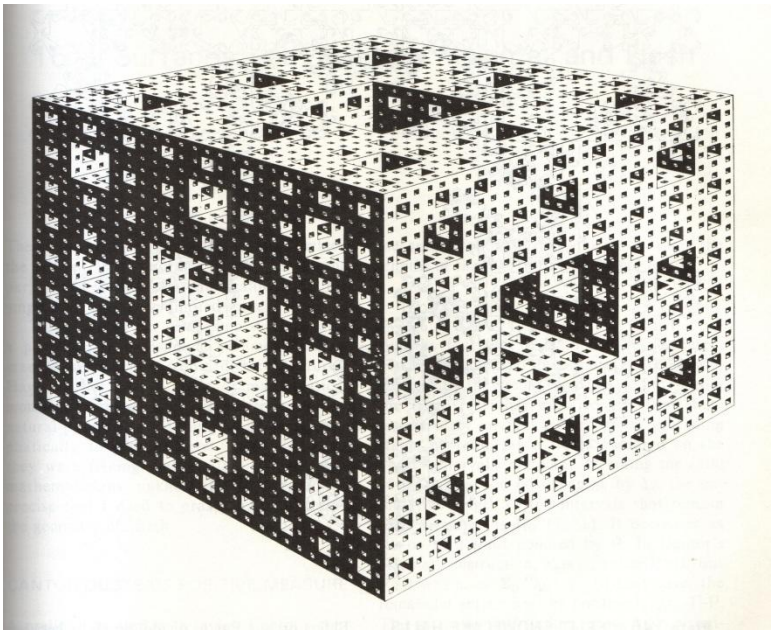

Figure A.8 The Menger sponge (Dimension D~2.7268). [1]

The Mandelbrot set is a particular mathematical set of points, whose boundary generates a distinctive and easily-recognizable two-dimensional fractal shape. [66] This set is named after the mathematician Benoit Mandelbrot, who studied and popularized it. Figure A.9 is the initial image of a Mandelbrot set. Technically, the Mandelbrot set is the set of values of c in the complex plane for which the orbit of 0 under iteration of the complex quadratic polynomial $z_{n+1}=z_n^2+c$ remains bounded. That is, a complex number, c, is part of the Mandelbrot set if, when starting with $z_0=0$ and applying the iteration repeatedly, the absolute value of z_n never exceeds a certain number (that number depends on c) however large n gets. [67] Figure A.10 is a mathematician's depiction of the Mandelbrot set M. A point c is colored black if it belongs to the set, and white if not. Re[c] and Im[c] denote the real and imaginary parts of c, respectively. Images of the Mandelbrot set display an elaborate boundary that reveals progressively ever-finer recursive detail at increasing magnifications. The "style" of this repeating detail depends on the region of the set being examined. The set's boundary also incorporates smaller

versions of the main shape, so the fractal property of self-similarity applies to the whole set, and not just to its parts. [68]

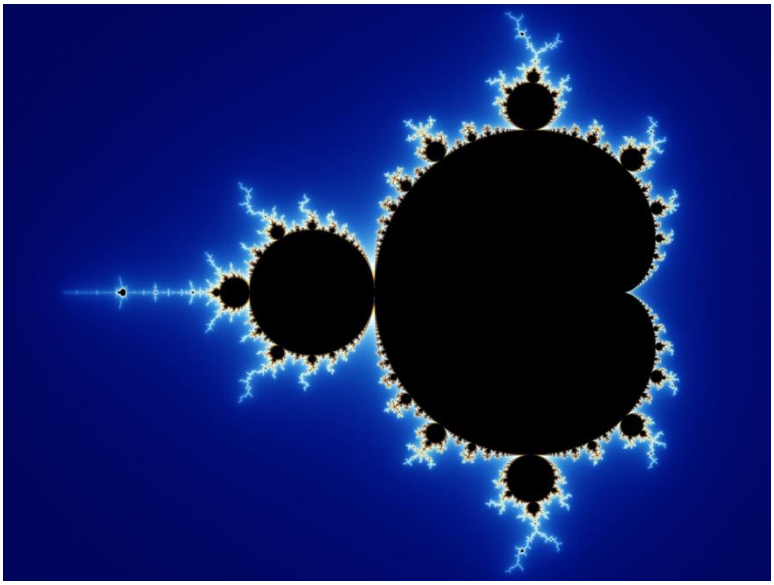

Figure A.9 Initial image of Mandelbrot set. [69]

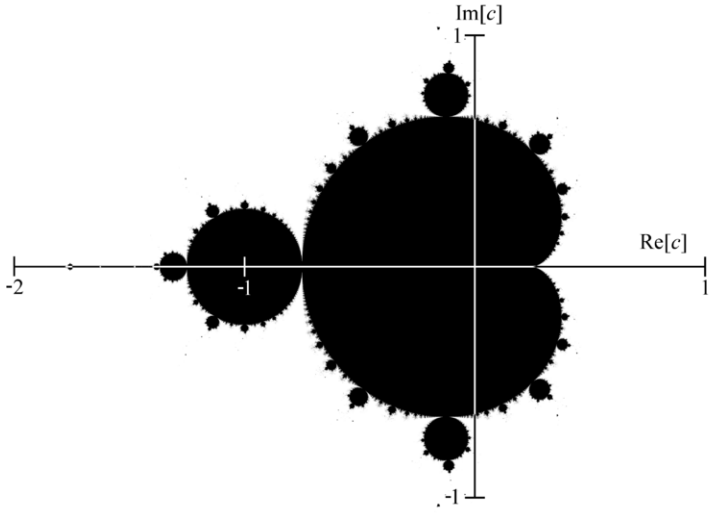

Figure A.10 A mathematician's depiction of the Mandelbrot set M. [70]

REFERENCES

1. Mandelbrot, B.B., *The Fractal Geometry of Nature*1983, New York: W. H. Freeman and Company.

2. Mandelbrot, B.B., D.E. Passoja, and A.J. Paullay, *Fractal character of fracture surfaces of metals.* Nature, 1984. **208**: p. 721-722.

3. Lu, C. *Some notes on the study of fractals in fracture*. in *The 5th Australasian Congress on Applied Mechanics*. 2007. Brisbane, Australia.

4. Zinn-Justin, J., *Quantum Field Theory and Critical Phenomena*. The Internationl Series of Monographs on Physics2002, New York: Oxford University Press.

5. Lu, P., et al., *Fractal characteristics of loess formation: evidence from laboratory experiments.* Engineering Geology, 2003. **69**: p. 287-293.

6. Walker, J. *Fractal Food: Self-Similarity on the Supermarket Shelf*. 2005 [cited 2012 March 5th]; Available from: http://www.fourmilab.ch/images/Romanesco/.

7. *An image of a fern*. [cited 2012 March 5th]; Available from: http://principiacosmologica.blogspot.com/2010/07/chaos-theory-part-2.html.

8. *Romanesco broccoli*. [cited 2012 March 5th]; Available from: http://pbmo.files.wordpress.com/2010/12/romanesco-broccoli-fractal.png.

9. Mandelbrot, B.B., *How Long Is the Coast of Britain? Statistical Self-Similarity and Fractional Dimension.* Science, 1967. **156**(3775): p. 636-638.

10. Vicsek, T., *Fractal growth phenomena*1992, Singapore: World Scientific Publishing Co. Pte. Ltd.

11. Falconer, K., *Fractal Geometry: Mathematical Foundations and Applications*2003, New York: Wiley.

12. Hurewicz, W. and H. Wallman, *Dimension Theory*1948, New Jersey: Princeton University Press.

13. *Estimating the Hausdorff dimension of the coast of Great Britain*. [cited 2012 March 5th]; Available from: http://en.wikipedia.org/wiki/File:Great_Britain_Hausdorff.svg

14. *Fractal and the Fractal Dimension*. [cited 2012 March 5th]; Available from: http://www.vanderbilt.edu/AnS/psychology/cogsci/chaos/workshop/Fractals.html

15. Schroeder, M., *Fractals, Chaos, Power Laws: Minutes from an Infinite Paradise*1992, New York: W. H. Freeman.

16. Peitgen, H.-O., H. Jurgens, and D. Saupe, *Chaos and Fractals: New Frontiers of Science*. 2nd ed2004, New York: Springer-Verlag New York, Inc.

17. Beke, D.B., *Principles of Comminution*1964, Hungary: Publishing House of the Hungarian Academy of Sciences.

18. Turcotte, D.L., *Fractals and Chaos in Geology and Geophysics*1997, New York: Cambridge University Press.

19. Carpinteri, A. and N. Pugno, *A fractal comminution approach to evaluate the drilling energy dissipation.* International Journal for Numerical and Analytical Methods in Geomechanics, 2002. **26**: p. 499-513.

20. Teng, S., et al., *Mathematical modeling of fluid energy milling based on a stochastic approach.* Chemical Engineering Science, 2010. **65**(15): p. 4323-4331.

21. Midoux, N., et al., *Micronization of pharmaceutical substances in a spiral Jet Mill.* Powder Technology, 1999. **104**: p. 113-120.

22. *Sanitary Design Micronizer*. [cited 2012 March 5th]; Available from: www.sturtevantinc.com.

23. Klapetek, P., D. Necas, and C. Anderson, *Gwyddion user guide*.

24. Teng, S., et al., *Analysis of Fluid Energy Mill by gas-solid two-phase flow simulation.* Powder Technology, 2011. **208**: p. 684-693.

25. Teng, S., et al., *Experimental and numerical analysis of a lab-scale fluid energy mill.* Powder Technology, 2009. **195**(1): p. 31-39.

26. Warsi, Z.U.A., *Fluid dynamics: theoretical and computational approaches*2006, Florida: CRC Press.

27. Launder, B.E. and D.B. Spalding, *The numerical computation of turbulent flows.* Methods in Applied Mechanics and Engineering, 1974. **3**: p. 269–289.

28. ANSYS, *ANSYS FLUENT 12.0 User's Guide*, April 2009.

29. Teng, S., *Investigation of the Dynamic Behavior of Particle Collisions and Size attrition Mechanisms within Fluid Energy Mills*, in *Department of Chemical, Biological & Pharmaceutical Engineering*2009, New Jersey Institute of Technology: New Jersey.

30. Mebtoul, M., J.F. Large, and P. Guigon, *High velocity impact of particles on a target – an experimental study*. International Journal of Mineral Processing, 1996. **44-45**: p. 77-91.

31. Lecoq, O., et al., *Fragmentation by high velocity impact on a target: a material grindability test.* Powder Technology, 2003. **133**: p. 113– 124.

32. Capece, M., E. Bilgili, and R. Dave, *Identification of the breakage rate and distribution parameters in a non-linear population balance model for batch milling.* Powder Technology, 2011. **208**: p. 195–204.

33. Timoshenko, S.P. and J.N. Goodier, *Theory of elasticity*1970, New York: McGraw-Hill.

34. Austin, L.G., *Approximate calculation of specific fracture energies for grinding.* Powder Technology, 1987. **53**: p. 145– 150.

35. Rowe and Roberts, *Mechanical Properties*, in *Pharmaceutical Powder Compaction Technology*1996, Marcel Dekker, Inc.: New York. p. p288.

36. Gercek, H., *Poisson's ratio values for rocks.* International Journal of Rock Mechanics and Mining Sciences, 2007. **44**(1): p. 1-13.

37. Lecoq, O., P. Guigon, and M.N. Pons, *A grindability test to study the influence of material processing on impact behaviour*. Powder Technology, 1999. **105**: p. 21-29.

38. Nagahama, H. and K. Yoshii, *Fractal dimension and fracture of brittle rocks.* International Journal of Rock Mechanics and Mining Sciences & Geomechanics Abstracts, 1993. **30**(2): p. 173-175.

39. Yang, J., et al., *In-situ Milling and Coating within A Fluid Energy Mill*, in *Proceedings of the 37th International Annual Conference of ICT (Energetic Materials)*2006. p. 2: 1-13.

40. Chen, W.L., et al. *Numerical modeling of the grinding velocity and pressure fields ofnitramine-based particulates flowing in a Fluid Energy Mill (FEM)*. in *Proceedings of the 38th International Annual Conference of ICT*. 2007.

41. Gogos, C.G., et al. *In-situ milling and coating of energetic materials with micron- and nano-particulates within a Fluid Energy Mill*. in *39th International Annual Conference of ICT (Energetic Materials)*. 2008.

42. Gogos, C.G., et al., *Continuous High Speed Coating of Finelly Ground Particles*, in *USPTO App.*2006.

43. Wang, P., et al., *A novel process for simultaneous milling and coating of particulates.* Powder Technology, 2009. **193**: p. 65-68.

44. Zhang, Q., et al., *In-situ, simultaneous milling and coating of particulates with nanoparticles.* Powder Technology, 2009. **196**: p. 292-297.

45. Zuiderduin, W.C.J., et al., *Toughening of polypropylene with calcium carbonate particles.* Polymer, 2002. **44**(1): p. 261-275.

46. Lin, Y., et al., *High impact toughness polypropylene/$CaCO_3$ nanocomposites and the toughening mechanism.* Macromolecules, 2008. **41**(23): p. 9204-9213.

47. Thio, Y.S., et al., *Toughening of isotactic polypropylene with $CaCO_3$ particles.* Polymer, 2002. **43**(13): p. 3661-3674.

48. Dubnikova, I.L., et al., *Preparation and characteristics of composites based on polypropylene and ultradispersed calcium carbonate.* Polymer Science - Series A, 2008. **50**(12): p. 1214-1225.

49. Mohanty, B. and K.S. Narasimhan, *Fluid energy grinding.* Powder Technology, 1982. **33**(1): p. 135-141.

50. Zhang, Q., et al., *Simultaneous milling and coating of inorganic particulates with polymeric coating materials using a fluid energy mill.* Polymer Engineering and Science, 2010. **50**(12): p. 2366-2374.

51. Solomon, G., *Leibniz and Topological Equivalence.* Dialogue, 1993. **32**: p. 721-724.

52. Pickover, C.A., *The Math Book: From Pythagoras to the 57th Dimension, 250 Milestones in the History of Mathematics*2009, New York: Sterling Publishing Company, Inc.

53. Cantor, G., *On infinite, linear point-manifolds (sets).* Mathematische Annalen, 1883. **21**: p. 545–591.

54. Barlow, M.T. and R.F. Bass, *Brownian Motion and Harmonic Analysis on Sierpinski Carpets.* Canadian Journal of Mathematics, 1999. **51**: p. 673-744.

55. Edgar, G.A., *Classics On Fractals*1993, Boston: Addison-Wesley Publishing.

56. *Cantor ternary set*. [cited 2012 March 5th]; Available from: http://en.wikipedia.org/wiki/File:Cantor_set_in_seven_iterations.svg.

57. *Sierpinski triangle*. [cited 2012 March 5th]; Available from: http://en.wikipedia.org/wiki/File:Sierpinski_triangle_evolution.svg.

58. *Sierpinski carpet*. [cited 2012 March 5th]; Available from: http://en.wikipedia.org/wiki/File:Sierpinski_carpet.png.

59. *Levy C curve*. [cited 2012 March 5th]; Available from: http://en.wikipedia.org/wiki/File:Levy_C_construction.png.

60. Murzi, M. *Jules Henri Poincaré (1854-1912)*. 2006 [cited 2012 March 5th]; Available from: http://www.iep.utm.edu/poincare/.

61. *Felix Klein*. [cited 2012 March 5th]; Available from: http://www.britannica.com/EBchecked/topic/319960/Felix-Klein.

62. Garnett, J., *Bounded Analytic Functions*1981, San Diego: Academic Press.

63. *Gaston Maurice Julia (1893 - 1978)*. [cited 2012 March 5th]; Available from: http://www-history.mcs.st-andrews.ac.uk/Mathematicians/Julia.html.

64. Gold, E., *Lewis Fry Richardson. 1881-1953.* Obituary Notices of Fellows of the Royal Society, 1954. **9**(1): p. 216-235.

65. Russ, J.C., *Fractal surfaces*. Vol. 1. 1994, New York: Springer.

66. Taylor, R.P. and J.C. Sprott, *Biophilic Fractals and the Visual Journey of Organic Screen-savers.* Nonlinear Dynamics, Psychology, and Life Sciences, 2008. **12**(1): p. 117-129.

67. *The Mandelbrot Set Explorer: Mathematical Glossary*. [cited 2012 March 5th]; Available from: http://math.bu.edu/DYSYS/explorer/def.html.

68. Lei, T., *The Mandelbrot Set, Theme and Variations*. London Mathematical Society Lecture Note Series2000, Cambridge, U.K.: Cambridge University Press.

69. *http://en.wikipedia.org/wiki/File:Mandel_zoom_00_mandelbrot_set.jpg*. [cited 2012 March 5th].

70. *http://en.wikipedia.org/wiki/File:Mandelset_hires.png*. [cited 2012 March 5th].